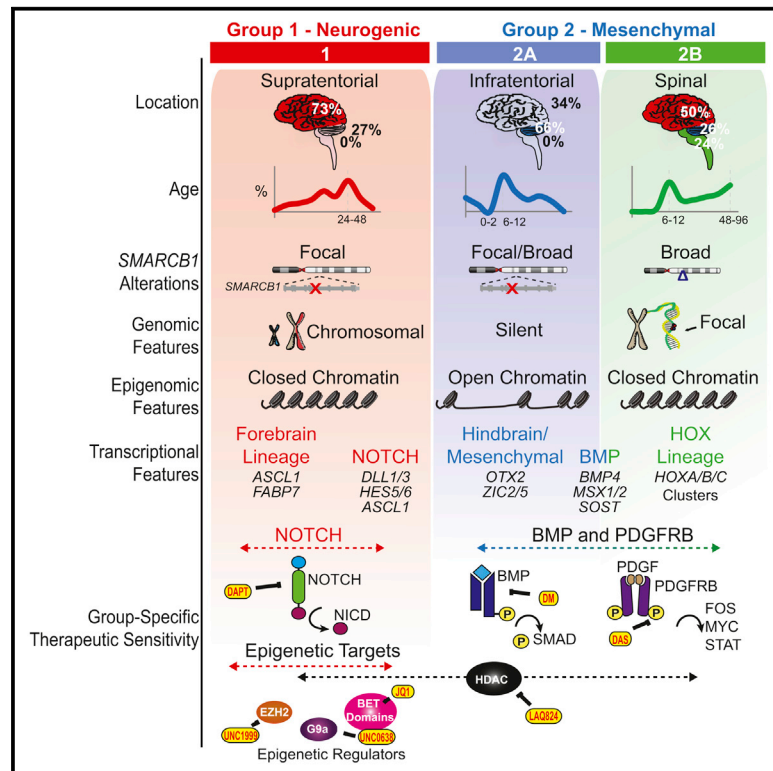


Cancer Cell

Integrated (epi)-Genomic Analyses Identify Subgroup-Specific Therapeutic Targets in CNS Rhabdoid Tumors

Graphical Abstract



Authors

Jonathon Torchia, Brian Golbourn, Shengrui Feng, ..., James T. Rutka, Nada Jabado, Annie Huang

Correspondence

ddecarv@uhnresearch.ca (D.D.D.C.), james.rutka@sickkids.ca (J.T.R.), nada.jabado@mcgill.ca (N.J.), annie.huang@sickkids.ca (A.H.)

In Brief

Torchia et al. show that atypical teratoid rhabdoid tumors (ATRTs) are composed of three epigenetic subgroups that correlate with differential cellular responses to a panel of signaling and epigenetic inhibitors. Specifically, dasatinib and nilotinib are identified as promising therapeutics for group 2 ATRTs.

Highlights

- ATRTs comprise three molecular and epigenetic subgroups: group 1, 2A, and 2B
- Distinct chromatin landscape drives subgroup-specific lineage and signaling features
- ATRT subgroups exhibit distinct sensitivity to signaling and epigenetic inhibitors
- Epigenetically regulated *PDGFRB* enhancer drives TKI sensitivity in group 2 ATRTs



Integrated (epi)-Genomic Analyses Identify Subgroup-Specific Therapeutic Targets in CNS Rhabdoid Tumors

Jonathon Torchia,^{1,2,7,13,73} Brian Golbourn,^{1,8,13,73} Shengrui Feng,^{3,14,73} King Ching Ho,^{7,13,73} Patrick Sin-Chan,^{1,2,7,13} Alexandre Vasiljevic,¹⁵ Joseph D. Norman,^{7,13} Paul Guilhamon,¹⁴ Livia Garzia,^{10,13} Natalia R. Agamez,^{7,13} Mei Lu,^{7,13} Tiffany S. Chan,^{1,2,7,13} Daniel Picard,^{7,13} Pasqualino de Antonellis,^{10,13} Dong-Anh Khuong-Quang,^{16,17} Aline C. Planello,¹⁴ Constanze Zeller,¹⁴ Dalia Barsyte-Lovejoy,¹⁴ Lucie Lafay-Cousin,²⁰ Louis Letourneau,¹⁹ Mathieu Bourgey,¹⁹

(Author list continued on next page)

¹Department of Laboratory Medicine and Pathobiology

²Department of Paediatrics

³Department of Medical Biophysics

⁴Department of Molecular Genetics

⁵Department of Computer Science

⁶Department of Surgery

University of Toronto, Toronto, ON M5G0A4, Canada

⁷Division of Hematology/Oncology

⁸Division of Neurosurgery

⁹Division of Pathology

¹⁰Program in Developmental & Stem Cell Biology

¹¹Program in Genetics & Genome Biology

¹²Department of Paediatric Laboratory Medicine

¹³Arthur and Sonia Labatt Brain Tumour Research Centre

Hospital for Sick Children, Toronto, ON M5G1X8, Canada

¹⁴Princess Margaret Cancer Center, University Health Network, Toronto, ON M5G1L7, Canada

¹⁵Department of Pathology, Groupement Hospitalier Est, CHU de Lyon, Lyon-Bron 69677, France

¹⁶Department of Pediatrics

¹⁷Department of Human Genetics

¹⁸Department of Pathology

McGill University, Montreal, QC H3Z2Z3, Canada

¹⁹Genome Quebec Innovation Centre, McGill University, Montreal, QC H3A1A4, Canada

(Affiliations continued on next page)

SUMMARY

We recently reported that atypical teratoid rhabdoid tumors (ATRTs) comprise at least two transcriptional subtypes with different clinical outcomes; however, the mechanisms underlying therapeutic heterogeneity remained unclear. In this study, we analyzed 191 primary ATRTs and 10 ATRT cell lines to define the genomic and epigenomic landscape of ATRTs and identify subgroup-specific therapeutic targets. We found ATRTs segregated into three epigenetic subgroups with distinct genomic profiles, *SMARCB1* genotypes, and chromatin landscape that correlated with differential cellular responses to a panel of signaling and epigenetic inhibitors. Significantly, we discovered that differential methylation of a *PDGFRB*-associated enhancer confers specific sensitivity of group 2 ATRT cells to dasatinib and nilotinib, and suggest that these are promising therapies for this highly lethal ATRT subtype.

Significance

ATRTs are considered to be genetically homogeneous with bland genomes. Our integrated genomic studies indicate a higher non-coding mutation rate and predominantly structural coding alterations, which suggest a more complex ATRT genome. We identify three epigenetic ATRT subtypes associated with distinct genotypic, chromatin, and functional landscapes that correlate with cellular responses to various signaling and epigenetic pathway inhibitors. Significantly, we identify two well-characterized cancer drugs, dasatinib and nilotinib, as promising therapeutic agents for group 2 ATRTs. Together with our earlier findings, our data provide compelling rationale for the development of a risk- and biology-stratified trial for ATRTs.

Man Yu,¹³ Deena M.A. Gendoo,^{7,13} Misko Dzamba,⁵ Mark Barszczyk,¹³ Tiago Medina,¹⁴ Alexandra N. Riemenschneider,^{8,13} A. Sorana Morrissy,^{10,13} Young-Shin Ra,²² Vijay Ramaswamy,^{7,13} Marc Remke,^{7,13} Christopher P. Dunham,²³ Stephen Yip,²⁵ Ho-keung Ng,²⁶ Jian-Qiang Lu,²⁷ Vivek Mehta,²⁸ Steffen Albrecht,¹⁸ Jose Pimentel,³⁰ Jennifer A. Chan,²¹ Gino R. Somers,¹² Claudia C. Faria,³¹ Lucia Roque,³² Maryam Fouladi,³³ Lindsey M. Hoffman,³⁴ Andrew S. Moore,³⁵ Yin Wang,³⁶ Seung Ah Choi,³⁷ Jordan R. Hansford,³⁸ Daniel Catchpoole,³⁹ Diane K. Birks,³⁴ Nicholas K. Foreman,³⁴ Doug Strother,²⁹ Almos Klekner,⁴⁰ Laszlo Bognár,⁴⁰ Miklós Garami,⁴¹ Péter Hauser,⁴¹ Tibor Hortobágyi,⁴² Beverly Wilson,²⁹ Juliette Hukin,²⁴ Anne-Sophie Carret,⁴³ Timothy E. Van Meter,⁴⁴ Eugene I. Hwang,⁴⁵ Amar Gajjar,⁴⁶ Shih-Hwa Chiou,⁴⁷ Hideo Nakamura,⁴⁸ Helen Toledano,⁴⁹ Iris Fried,⁵⁰ Daniel Fufts,⁵¹

(Author list continued on next page)

²⁰Division of Pediatric Hematology/Oncology, Alberta Children's Hospital, AB T3B6A8, Canada

²¹Department of Pathology and Laboratory Medicine, University of Calgary, Calgary, AB T2N1N4, Canada

²²Department of Neurosurgery, Asan Medical Center, Seoul 138-736, Korea

²³Division of Anatomic Pathology

²⁴Division of Hematology and Oncology

Children's and Women's Health Centre of B.C., University of British Columbia, Vancouver, BC V6H3N1, Canada

²⁵Department of Pathology & Laboratory Medicine, University of British Columbia, V6T1Z3, Canada

²⁶Department of Anatomical and Cellular Pathology, Chinese University of Hong Kong, Hong Kong, China

²⁷Laboratory Medicine and Pathology

²⁸Division of Neurosurgery

²⁹Division of Pediatric Hematology/Oncology

Stollery Children's Hospital, University of Alberta, Edmonton, AB T2W3N2, Canada

³⁰Division of Pathology

³¹Department of Neurosurgery

Hospital de Santa Maria, Centro Hospitalar Lisboa Norte, Lisbon 1649-035, Portugal

³²Cytometry and Cytogenetic Laboratory, CIPM, Portuguese Cancer Institute, Lisbon 1099-023, Portugal

³³Division of Oncology, Department of Cancer and Blood Diseases, Cincinnati Children's Hospital, Cincinnati, OH 45229, USA

³⁴Department of Pediatrics, University of Colorado, Denver, CO 80045, USA

³⁵Oncology Service, Children's Health Queensland Hospital; University of Queensland Diamantina Institute, Brisbane, QLD 4102, Australia

³⁶Research Institute of Health Development Strategies, Fudan University, Shanghai 200032, China

³⁷Division of Pediatric Neurosurgery, Seoul National University Children's Hospital, Seoul 03080, Korea

³⁸Royal Children's Hospital, Murdoch Children's Research Institute, Melbourne, VIC 3052, Australia

³⁹Children's Cancer Research Unit, Children's Hospital at Westmead, Westmead, NSW 2145, Australia

⁴⁰Department of Neurosurgery, University of Debrecen, Debrecen 4032, Hungary

⁴¹Second Department of Pediatrics, Semmelweis University, Budapest 1094, Hungary

⁴²Department of Histopathology, University of Szeged, Szeged 6720, Hungary

⁴³Department of Pediatrics, Division of Hematology-Oncology, Université de Montréal/CHU Sainte-Justine, Montreal, QC H3T1C5, Canada

⁴⁴Department of Neurosurgery, Virginia Commonwealth University, Richmond, VA 23298-0631, USA

⁴⁵Department of Oncology, Children's National Medical Center, Washington, DC 20010, USA

⁴⁶Division of Neuro-Oncology, St. Jude Children's Research Hospital, Memphis, TN 38105, USA

⁴⁷Department of Medical Research, Taipei Veterans General Hospital and National Yang-Ming University, Taipei 112, Taiwan

⁴⁸Department of Neurosurgery, Kumamoto University, Kumamoto 860-8556, Japan

⁴⁹Department of Pediatric Hematology Oncology, Children's Medical Center of Israel, Petach Tikva 49202, Israel

⁵⁰Department of Pediatric Hematology-Oncology, Hadassah Hebrew University Medical Center, Jerusalem 91120, Israel

⁵¹Department of Neurosurgery, University of Utah, School of Medicine, Salt Lake City, UT 84132, USA

⁵²Department of Neurosurgery, Shizuoka Children's Hospital, Shizuoka 420-8660, Japan

⁵³Department of Pediatrics, McMaster University, Hamilton, ON L8S4K1, Canada

(Affiliations continued on next page)

INTRODUCTION

Rhabdoid tumors (RT) are highly malignant, multi-lineage neoplasms of early childhood originally described in kidneys and soft tissues, but most frequently seen in the CNS where they are called atypical teratoid rhabdoid tumors (ATRTs). ATRTs were historically considered incurable, and although outcomes have improved with intensified multimodal therapy, most patients survive less than 1 year after diagnosis (Chi et al., 2008; Hilden, 2004; Lafay-Cousin et al., 2012; Teakautz, 2005).

Biallelic *SMARCB1* loss-of-function alterations are diagnostic of all RTs (Versteeg et al., 1998). Up to 35% of ATRTs patients have heritable *SMARCB1* alterations, which predispose to multiple RTs (Eaton et al., 2011). Indeed, *Smarcb1*^{+/-} mice also develop soft-tissue- or neural-crest-derived RTs (Klochendler-Yeivin et al., 2000; Roberts et al., 2002), and ATRTs can arise from conditional inactivation of *Smarcb1* (Han et al., 2016). *SMARCB1* is a constitutive component of the SWI/SNF chromatin-remodeling complex, which exhibits substantial structural and functional diversity during neurogenesis. Loss of *SMARCA4* (Hasselblatt et al., 2011), which encodes another component of

Takafumi Wataya,⁵² Chris Fryer,²⁴ David D. Eisenstat,²⁹ Katrin Scheinemann,⁵³ Adam J. Fleming,⁵³ Donna L. Johnston,⁵⁴ Jean Michaud,⁵⁵ Shayna Zelcer,⁵⁶ Robert Hammond,⁵⁷ Samina Afzal,⁵⁸ David A. Ramsay,⁵⁷ Nongnuch Sirachainan,⁵⁹ Suradej Hongeng,⁵⁹ Noppadol Larbcharoensub,⁶⁰ Richard G. Grundy,⁶¹ Rishi R. Lulla,⁶² Jason R. Fangusaro,⁶² Harriet Druker,⁷ Ute Bartels,⁷ Ronald Grant,⁷ David Malkin,^{2,7,11} C. Jane McGlade,^{3,13} Theodore Nicolaides,⁶³ Tarik Tihan,⁶⁴ Joanna Phillips,⁶⁴ Jacek Majewski,^{17,19} Alexandre Montpetit,¹⁹ Guillaume Bourque,^{17,19} Gary D. Bader,⁴ Alyssa T. Reddy,⁶⁵ G. Yancey Gillespie,⁶⁶ Monika Warmuth-Metz,⁶⁷ Stefan Rutkowski,⁶⁸ Uri Tabori,^{1,7,11,13} Mathieu Lupien,^{3,14} Michael Brudno,^{5,11} Ulrich Schüller,⁶⁹ Torsten Pietsch,⁷⁰ Alexander R. Judkins,⁷¹ Cynthia E. Hawkins,^{1,9,13} Eric Bouffet,^{7,13} Seung-Ki Kim,³⁷ Peter B. Dirks,^{8,13} Michael D. Taylor,^{8,10,13} Anat Erdreich-Epstein,⁷² Cheryl H. Arrowsmith,¹⁴ Daniel D. De Carvalho,^{3,14,*} James T. Rutka,^{6,8,13,*} Nada Jabado,^{16,17,*} and Annie Huang^{1,2,7,13,74,*}

⁵⁴Department of Pediatrics

⁵⁵Pathology and Laboratory Medicine

Children's Hospital of Eastern Ontario, University of Ottawa, Ottawa, ON K1H8L1, Canada

⁵⁶Division of Pediatric Hematology/Oncology, Children's Hospital, London Health Sciences Center, London, ON N6A5A5, Canada

⁵⁷Department of Pathology and Laboratory Medicine, Children's Hospital of Western Ontario, University of Western Ontario, London, ON N6A5W9, Canada

⁵⁸Department of Pediatrics, Dalhousie University, Halifax, NS B3H4R2, Canada

⁵⁹Department of Pediatrics, Faculty of Medicine, Ramathibodi Hospital, Mahidol University, Bangkok 10300, Thailand

⁶⁰Department of Pathology, Faculty of Medicine, Ramathibodi Hospital, Mahidol University, Bangkok 10400, Thailand

⁶¹Children's Brain Tumour Research Centre, University of Nottingham, Nottingham NG72RD, England

⁶²Division of Pediatric Hematology-Oncology and Stem Cell Transplantation, Ann and Robert H. Lurie Children's Hospital of Chicago, Chicago, IL 60611, USA

⁶³Department of Pediatrics (Hematology/Oncology)

⁶⁴Department of Neurosurgery

University of California, San Francisco, San Francisco, CA 94143-0112, USA

⁶⁵Department of Pediatric Hematology and Oncology

⁶⁶Department of Neurosurgery

University of Alabama, Birmingham, AL 35233, USA

⁶⁷Department of Neuroradiology, University of Würzburg, Würzburg 97070, Germany

⁶⁸Department of Pediatric Hematology and Oncology

⁶⁹Department of Neuropathology

University Medical Center Hamburg-Eppendorf, Hamburg 20246, Germany

⁷⁰Institute for Neuropathology, University of Bonn Medical Center, Bonn 53105, Germany

⁷¹Department of Pathology & Laboratory Medicine, Children's Hospital of Los Angeles, Los Angeles, CA 90027, USA

⁷²Department of Pediatrics, Children's Hospital Los Angeles, Keck School of Medicine, University of Southern California, Los Angeles, CA 90027, USA

⁷³Co-first author

⁷⁴Lead Contact

*Correspondence: ddecarv@uhnresearch.ca (D.D.D.C.), james.rutka@sickkids.ca (J.T.R.), nada.jabado@mcgill.ca (N.J.), annie.huang@sickkids.ca (A.H.)

<http://dx.doi.org/10.1016/j.ccell.2016.11.003>

the SWI/SNF complex in some ATRTs, further underscores SWI/SNF-directed epigenetic mechanisms as critical in ATRT development. Although cumulative data support a central role for *SMARCB1* in RT initiation, specific mechanisms driving tumor development remain unclear. *SMARCB1* deficiency leads to aberrant nucleosomal positioning by the SWI/SNF complex and is associated with upregulation of EZH2, a histone methyl transferase of the repressive PRC2 complex (Roberts and Orkin, 2004) with consequent deregulation of multiple downstream signaling pathways. These observations have led to RT therapies targeting EZH2 and other downstream pathways (Kim and Roberts, 2016; Wilson et al., 2010).

Surprisingly, despite the highly malignant and heterogeneous nature of ATRTs, exome studies indicate only recurrent *SMARCB1* coding alterations (Johann et al., 2016; Lee et al., 2012). We recently reported that ATRTs comprised at least two transcriptional subtypes with different clinical phenotypes (Torchia et al., 2015). While group 1 ATRTs with neurogenic signatures correlated with superior survival, group 2 ATRTs with

mesenchymal signatures had aggressive, treatment-resistant phenotypes and dismal outcomes. However, mechanisms underlying varied therapeutic responses in ATRT patients remain unclear. Therefore, we performed an integrated genomic and functional epigenomic analysis of a large cohort of primary tumors and cell lines to elucidate subgroup-specific therapeutic sensitivities in ATRT.

RESULTS

ATRTs Comprise Three Epigenetic Subtypes with Distinct Clinical Profiles and Genotypes

We integrated whole-genome sequencing (WGS), whole-exome sequencing (WES), high-resolution copy number profiling, and RNA-sequencing (RNA-seq) analyses with gene expression and methylation profiling on a total of 191 primary tumors (Table S1). Consistent with prior studies, coding region single-nucleotide variation (SNV) rate was low with only recurrent *SMARCB1* coding mutations (Figure 1A, Table S2). However, intergenic mutation

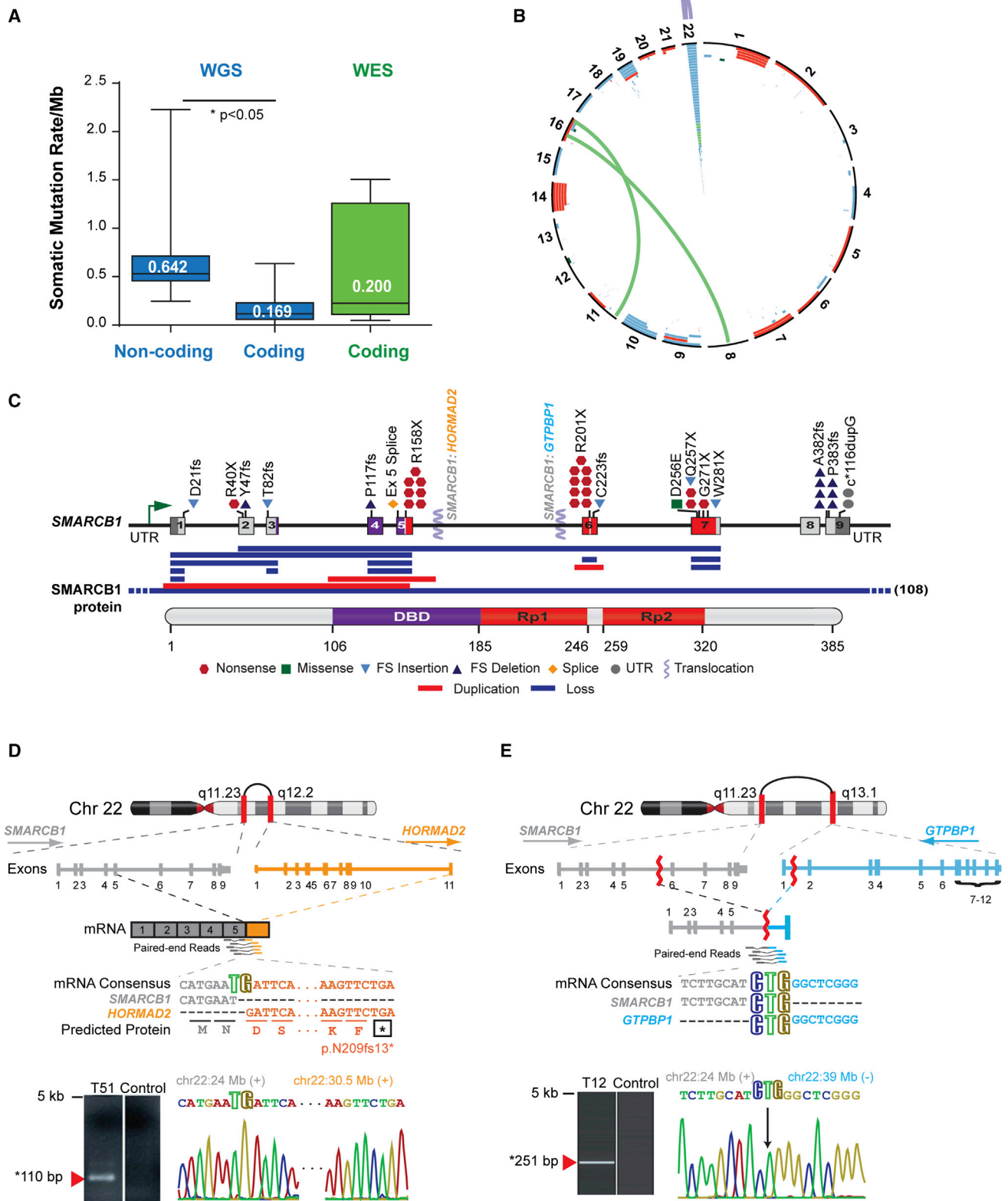


Figure 1. ATRT Coding Genome Is Predominantly Targeted By Structural Alterations

(A) Global genome and coding region somatic mutation rate in ATRTs. Median somatic mutation rates/Mb were calculated using WGS and WES data on 26 primary ATRTs with matched normal DNA. Boxplot middle represents median, box boundaries represent first and third quartiles; whiskers represent min and max values.

(legend continued on next page)

rate was significantly higher (0.64 mutation/Mb), suggesting that non-coding alterations may be important in ATRT (Figure 1A). Interestingly, we identified a spectrum of 379 copy number alterations (CNAs), including whole-arm gains and losses, focal deletions, duplications, and complex inter- and intrachromosomal gene rearrangements and uncovered 1.84–3.57 structural alterations/ATRT (Figure 1B; Tables S2 and S3). Cell adhesion, neural development, and chromatin-remodeling genes were targeted by recurrent coding region CNAs in up to 20% of ATRTs (Table S4) (Figure S1), and *SMARCB1* lacked previously reported mutational hotspots (Bourdeaut et al., 2011; Jackson et al., 2009). Notably, *SMARCB1* loss in 55.8% of ATRTs analyzed arose from structural events including exon duplications and gene fusions to *HORMAD2* and *GTPBP1* (Figures 1C–1E; Table S5), indicating structural alterations as predominant mechanisms for *SMARCB1* loss in ATRTs.

Unsupervised cluster analyses of 450k methylation microarray data from 162 ATRTs revealed three epigenetic classes with high concordance to gene expression subtypes determined from 90 primary ATRTs (Figures 2A and 2B, S2A–S2E). While group 1 ATRTs comprised a single methylation cluster, group 2 tumors further segregated into two methylation subtypes (group 2A and 2B). ATRT subtypes correlated with distinct clinical and genotypic features (Figures 2C and 2D; Table S6); group 1 and 2A tumors arose predominantly in the supratentorial/cerebral (38/52; 73.1%) and infratentorial (cerebellum, brain stem) (42/64; 65.6%) locations, respectively. Group 1 and 2A ATRTs were seen in the oldest (median age 24 months; 95% confidence interval [CI] = 20.70–26.55) and youngest (median age 12 months; 95% CI = 11.05–13.00) children, respectively. Group 2B ATRTs encompassed more heterogeneous locations and included infra- (9/34; 26.5%), supratentorial (17/34; 50.0%), and all spinal (8/34; 23.5%) tumors. Group 2B patients spanned a broader age distribution and comprised the majority of patients older than 3 years of age (12/32; 37.5%). We found no significant subgroup association with gender or tumor metastases.

Although SNV alteration rates were comparable across subgroups, we observed genotypic differences; group 2B tumors had more focal genomic alterations (mean = 1.83; 95% CI = 1.43–2.31 alterations/tumor; $p = 0.0024$) than group 1 (mean = 0.86; 95% CI = 0.65–1.12 alterations/tumor) and 2A (mean = 0.88; 95% CI = 0.68–1.13 alterations/tumor; Figures 2C and Table S6) tumors. While group 1 tumors were distinguished by recurrent chr14 gains and chr19 losses, group 2B tumors exhibited focal copy number losses across multiple chromosomes, and group 2A ATRTs were genomically bland (Figure S3). Strikingly, our analyses revealed the type of genetic event leading to *SMARCB1* loss also differed between ATRT subgroups ($p = 2.79 \times 10^{-4}$; Figure 2C; Table S6). Most group

1 tumors (30/45; 66.7%) exhibited focal/subgenomic alterations with predicted retention of the *SMARCB1* transcriptional start site; however, group 2B tumors had large deletions encompassing *SMARCB1* and frequently additional chr22 genes, thus indicating *SMARCB1* genotype:phenotype correlations in ATRTs.

ATRT Subgroups Have Distinct Lineage-Enriched Functional Genomes

Our observation of specific genotypes suggests that *SMARCB1* loss may have different functional consequences in ATRT subtypes. To define core molecular and cellular features of ATRT subgroups, we integrated supervised analyses of transcriptional and methylation data and observed that, while ATRTs generally exhibited a hypermethylated genome relative to other pediatric brain tumors, group 2A ATRTs had the lowest CpG island methylation levels compared with group 1 and 2B tumors (Figure S4A). Distribution of differentially methylated probes in CpG islands or gene bodies were similar across subgroups (Figure S4B); however, methylation and expression levels of lineage and developmental signaling genes differed significantly between subgroups (Figure 3A). These findings were corroborated by ingenuity pathway analyses (Figure 3B; Table S7), which revealed neurogenic genes (*FABP7*, *ASCL1*, *MYCN*, *c1orf61*) and genes involved in NOTCH (*DLL1/3 HES5/6*), glutamate receptor (*SLC17A8*, *SLC17A6*), and axonal guidance (*TUBB2B/3/4A*, *SEMA6A*) signaling, were most highly expressed and hypomethylated in group 1 ATRTs. BMP signaling (*BMP4*, *BAMBI*, *GDF5*, *FOXC1*) and mesenchymal differentiation (*SERPINF1*, *CLDN10*, *FBN2*, *MSX1*, *PDGFRB*) genes were most differentially expressed and methylated in group 2A/B tumors (Figure 3C; Table S7). Group 2A tumors were further distinguished by enrichment of visual cortex/hindbrain development (*OTX2*), retinol (*RBP1*, *RBP7*, *RDH5*, *RDH10*), and tyrosine (*TYR*) metabolism genes, while upregulation of *MYC* and *HOXB/C* clusters was seen in group 2B tumors (Figure 3C). Detailed analyses showed high concordance of CpG methylation patterns at promoters with ATRT subtypes, thus suggesting epigenetic regulation of developmental/cell lineage signaling pathways in ATRTs (Figures 3D and S5). Interestingly, while many group 2A enriched genes had functions in pluripotency and EMT, group 2B ATRTs exhibited heterogeneous profiles with enrichment of interferon signaling, cell adhesion, and cytoskeletal genes (Figure 3B).

To further investigate the distinct functional epigenome of ATRT subgroups, we performed high-resolution, genome-wide chromatin accessibility mapping using the assay for transposase-accessible chromatin (ATAC)-sequencing (ATAC-seq) analyses on five primary tumors (two group 1 and 2A, one group 2B) and four ATRT cell lines. In keeping with methylation and transcriptional analyses, principle component and correlation

(B) Circos plot of recurrent structural alterations, including SCNAs and gene rearrangements, from integrated WGS, RNA-seq, SNP, and 450k methylation array copy number data of 180 primary ATRTs.

(C) Schema of *SMARCB1* alterations relative to DNA binding domain (DBD) and repeat regions 1 and 2 (Rp1 and Rp2) domains in the *SMARCB1* protein.

(D) Schema of a chr22q intrachromosomal fusion of *SMARCB1* exon 5 (gray) and *HORMAD2* exon 11 (orange) identified by RNA-seq in ATRT T51 with consensus sequence and RT-PCR and Sanger sequencing validation of the fusion mRNA.

(E) Schematic of a chr22q intrachromosomal translocation involving *SMARCB1* intron 5 (gray) and *GTPBP1* intron 1 (blue) identified by WES in ATRT T12 with CREST predicted mRNA consensus sequence of respective gene fragments and PCR and Sanger sequencing validation of breakpoint.

See also Figure S1, Tables S1, S2, S3, S4, and S5.

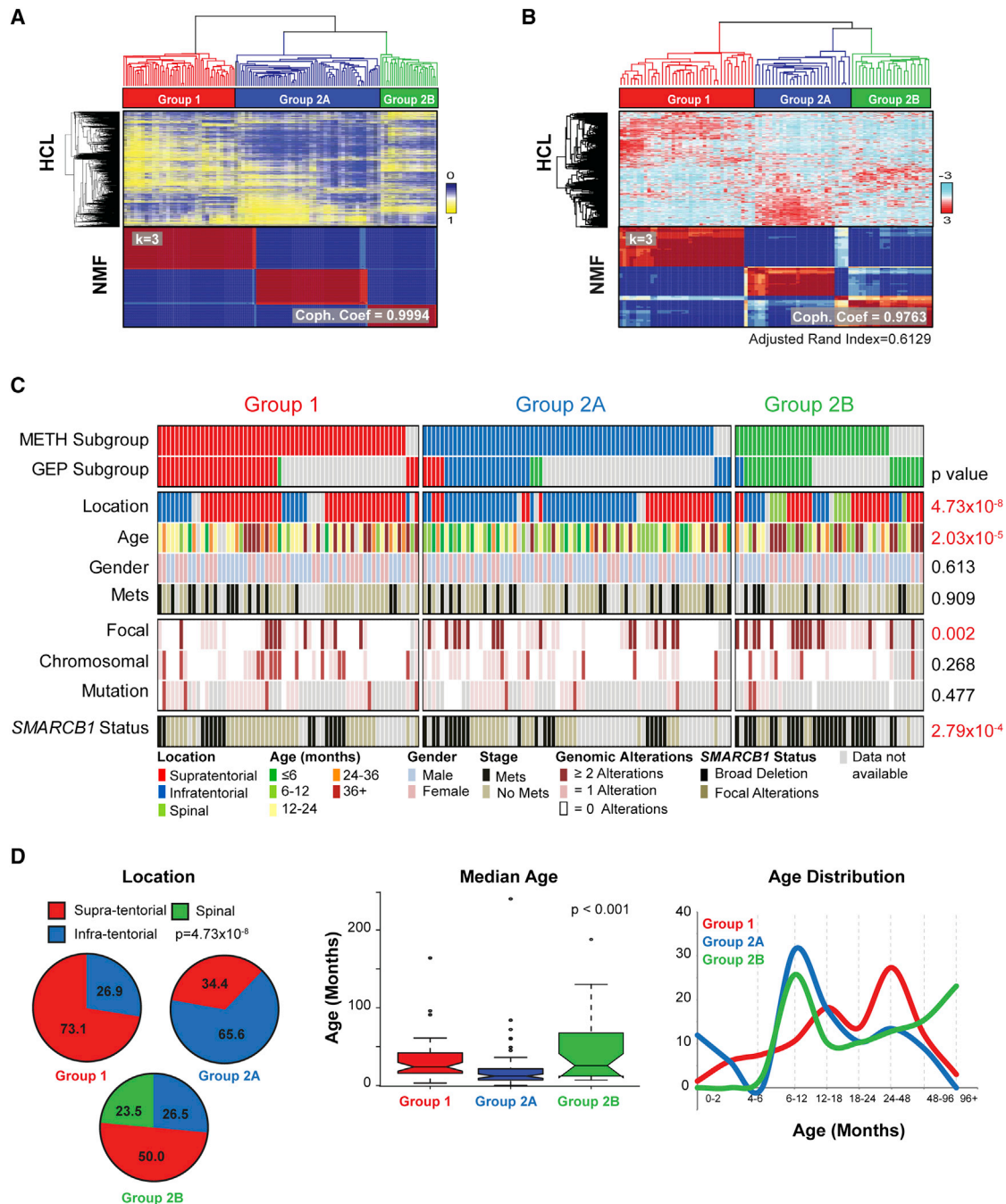


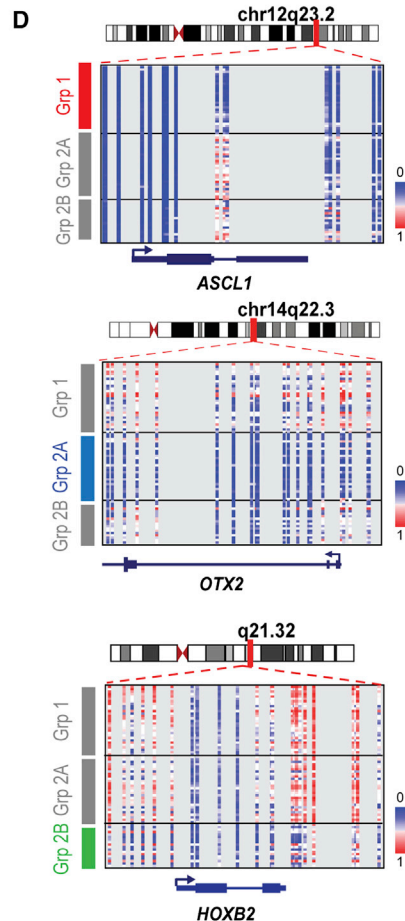
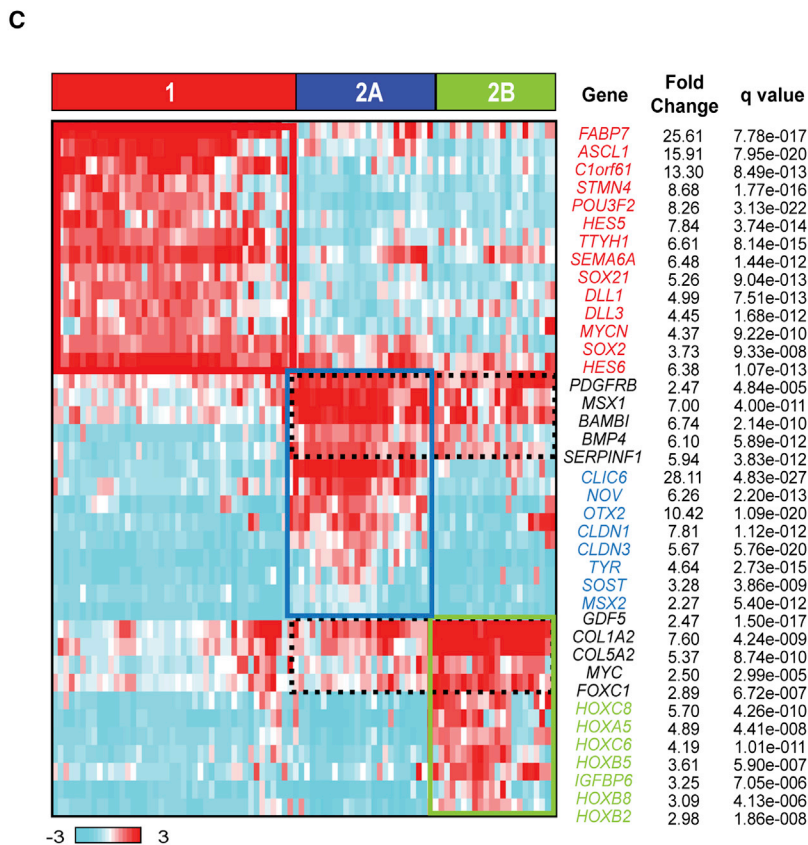
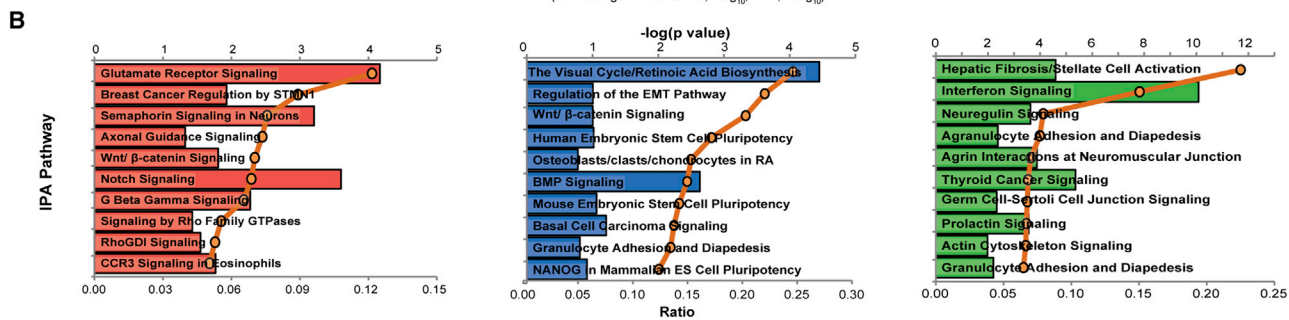
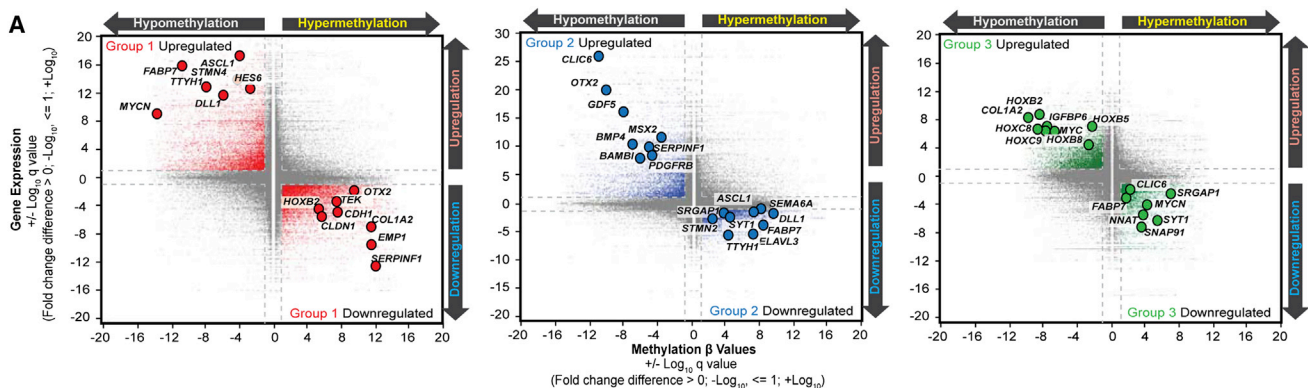
Figure 2. ATRTs Comprise Three Epigenetic Subgroups with Distinct Clinical Profiles and Genotypes

(A and B) ATRTs were classified by unsupervised consensus hierarchical (HCL) and non-negative matrix factorization (NMF) cluster analyses of 450k methylation array (A) or Illumina HT12 gene expression array data (B). Adjusted Rand Index indicates concordance in methylation and gene expression clusters. Most stable tumor grouping indicated by highest cophenetic coefficient (Coph. Coef; $k = 3$) with 250 genes and 10,000 methylation probes are shown.

(C) Clinical, molecular, and genotypic features of 177 primary ATRTs. Tumor subgroups determined by methylation or gene expression are indicated by red (group 1), blue (group 2A), green (group 2B) or gray (group not available) bars; clinical (tumor location, patient age, metastatic status), global patterns of CNAs (chromosomal or subchromosomal/focal), and type of *SMARCB1* alterations in individual tumors are indicated. Clinical or molecular features with significant subgroup correlation are indicated in red. *SMARCB1* alterations were classified as focal (point mutations, small indels, intergenic deletions) or broad (intragenic events, large deletions).

(D) Tumor location, median age, and age distribution in ATRT subgroups. Boxplot middle represents median, box boundaries represent first and third quartiles, and whiskers represent 10th and 90th percentiles.

See also [Figures S2, S3](#), and [Table S6](#).



(legend on next page)

analysis of primary ATRT ATAC-seq data showed segregation and association of ATRT subtypes with distinct ATAC-seq profiles (Figure 4A; Table S8). Integration of ATAC-seq footprints with RNA-seq data revealed open chromatin landscape in group 2A ATRTs that correlated with generally increased gene expression patterns in contrast to more closed chromatin landscapes and decreased gene expression patterns in group 1 tumors, while group 2B ATRTs exhibited an intermediate profile (Figure 4B). Specifically, we observed that group 1 (*ASCL1*, *FABP7*) and group 2A/B (*OTX2*, *ZIC1/4*, *ZIC5/2*) cell lineage genes and multiple signaling genes including ligands of NOTCH (*DLL1*, *HES6*) and BMP (*BMP4*, *MSX2*) pathways displayed open chromatin in a subtype-specific pattern. ATAC-seq analyses of ATRT cell lines showed similar patterns indicating that subgroup lineage and signaling features were maintained in cell lines (Figures 4C and 4D). These data suggest that ATRT subgroups and *SMARCB1* genotypes correlate with distinct functional epigenomes and indicate that epigenomic mechanisms drive lineage-specific gene expression and potential targetable therapeutic pathways in ATRTs.

NOTCH and BMP Signaling Drive ATRT Subgroup-Specific Cell Growth

To investigate subtype-specific therapies, we used expression profiling to determine molecular grouping of ten ATRT cell lines including 78C and 34C, respectively, derived from tumors T13 (group 1), T45 (group 2B), and established lines CHLA02, CHLA04, CHLA05, CHLA06, CHLA266, BT12, BT16, and SH. Prediction analysis of microarray (PAM) analyses of gene expression data from primary ATRTs reproducibly classified cell lines into subgroups 1 and 2 which, respectively, showed enrichment of neurogenic/NOTCH and mesenchymal/BMP signaling genes seen in corresponding primary ATRT subtypes. Western blot analyses confirmed expression of NOTCH intracellular domain (NICD) and phosphorylated SMAD1/5 (pSMAD1/5), respective effectors of NOTCH and BMP signaling in primary group 1 and 2 ATRTs and corresponding cell lines (Figure 5A), indicating that subtype signaling pathways were maintained.

To evaluate functional significance of NOTCH and BMP signaling, we used DAPT (N-[N-(3,5-difluorophenacetyl)-L-alanyl]-S-phenylglycine t-butyl ester), a γ -secretase inhibitor (Geling et al., 2002), and dorsomorphin (DM) (Yu et al., 2008) to, respectively, assess effects of NOTCH and BMP inhibition on a panel of group 1 (78C, CHLA05, CHLA02) and group 2A/B (SH, CHLA06, BT16) cell lines with most consistent growth phenotypes. Cell viability assays showed robust dose-dependent growth inhibition of group 1 and 2 cell lines with DAPT and DM treatment, respectively (Figures 5B and S6A), while cross-treatment of group 1 and

2 cell lines respectively with DM and DAPT had insignificant growth effects. Western blot and qRT-PCR analyses confirmed growth inhibition by DAPT correlated with dose-dependent downregulation of NICD and NOTCH transcriptional targets *HES1* and *HES5* in group 1 lines (Figures 5C and S6B). Similarly, we observed a dose-dependent decrease in pSMAD1/5 and BMP target genes *SOST* and *BAMBI* in group 2 cell lines (Figures 5D and S6B). Changes in NICD and pSMAD1/5 levels after DAPT and DM treatments also correlated with increased cell death in TUNEL assays (Figure S6C). We confirmed that the growth effects of γ -secretase inhibitors were mediated via NOTCH signaling in group 1 cells using siRNA-mediated knockdown of the NOTCH effector RBPJ, which significantly diminished growth of group 1 (CHLA04/05) but not group 2 cell lines (BT12/BT16) (Figure 5E). These data collectively indicate that NOTCH and BMP are important ATRT subgroup-specific survival pathways and attractive pharmacologic targets.

Epigenetic Regulation of an Enhancer Element Underlies Group 2 ATRT Sensitivity to Pharmacologic Inhibitors of PDGFRB Signaling

Recent studies report promising therapies targeting various epigenetic and signaling pathways in ATRTs (Ginn and Gajjar, 2012); however, the relevance of these agents to ATRT subtypes is unknown as prior studies examined a few cell lines. To identify additional subgroup-specific targets, we tested the effects of 14 small molecules targeting epigenetic pathways on growth of three group 1 (CHLA04, 02, 05) and five group 2 ATRT (CHLA266/06, SH, BT16/12) lines (Figure S7A). We selected small-molecule inhibitors with well-defined in vitro cellular activity that target Bromo/BET domain proteins (JQ1, PFI-1,2, GSK2801, SGC-CBP30), methyltransferases (GSK343, UNC1999, UNC0642, UNC0638, A-366, J4, DOT1L, LLY507), and histone deacetylases (LAQ824). Cell viability assays showed that five of the 14 compounds had consistent significant effects on cell growth (>30% reduction in cell viability), including UNC0638, UNC1999, JQ1, LAQ824, and J4. LAQ824 and J4 significantly diminished growth of all cell lines. In contrast, UNC0638, UNC1999, and JQ1 treatment induced >30% reduction in viability of all three group 1 cell lines but did not affect three out of five group 2 cell lines (Figures 6A, 6B, S7A, and S7B). Interestingly, gene expression analyses showed that *EHMT2* (encodes G9a), *EZH2*, *BRD4*, and related loci (*BRD1-BRD7*) were highly expressed across all ATRTs (data not shown), and suggest that therapeutic sensitivity to epigenetic inhibitors may be dependent on a distinct functional chromatin landscape in ATRT subtypes.

Dasatinib and nilotinib are ATP-competitive small-molecule multi-tyrosine kinase inhibitors (TKIs) of BCR-ABL fusion protein,

Figure 3. ATRT Subgroups have Distinct Lineage-Enriched Transcriptional and Methylation Signatures

(A) Starburst plot of ATRT subgroup-specific genes with reciprocal changes in methylation (x axis) and gene expression (y axis). Genes associated with group 1 (left panel; red), group 2A (middle panel; blue), and group 2B (right panel; green) ATRTs are highlighted.

(B) Top ten (top axis) enriched pathways for each subgroup was determined by ingenuity pathway analysis (IPA) of subgroup-specific genes with ± 2 -fold difference in expression; relative enrichment of pathways is shown on bottom axis.

(C) Gene expression heatmap of subgroup-enriched neural/mesenchymal lineage and NOTCH/BMP/HOX signaling genes in ATRT determined by supervised t test with FDR correction. Genes enriched in individual subgroups, or shared by subgroups 2A and 2B are shown by solid and dashed boxes, respectively.

(D) Heatmaps show methylation levels of representative lineage genes in ATRT subgroups; methylation status of probes in *ASCL1*, *OTX2*, and *HOXB2* are shown relative to transcriptional start sites.

See also Figures S4, S5, and Table S7.

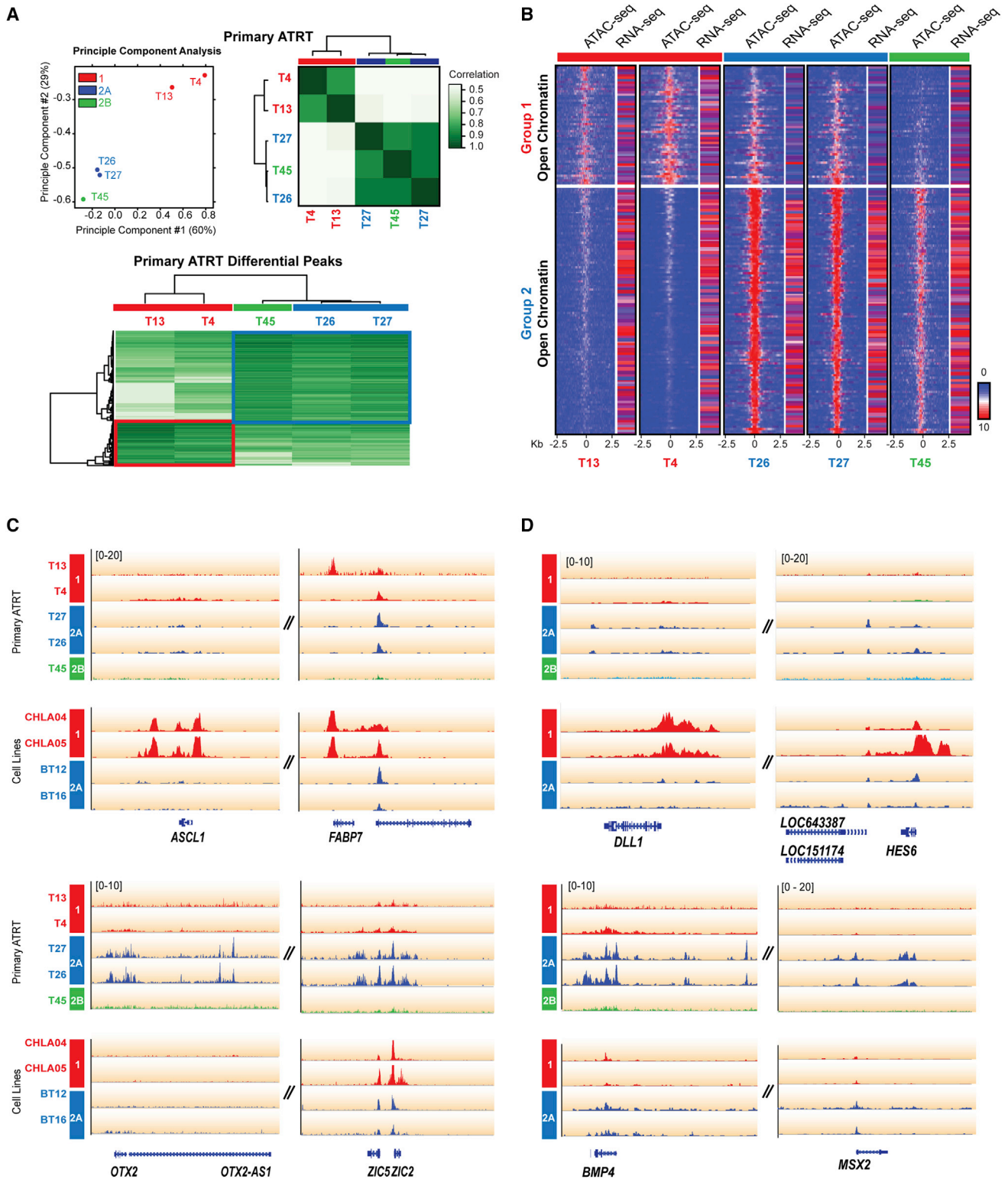


Figure 4. ATRT Subgroups Have Unique Chromatin Landscape and Functional Genomes

(A) Principle component analysis (PCA) and correlation analysis of ATAC-seq data from five primary ATRTs. Aligned sequence reads from ATAC-seq profiling were converted to peak tag counts using HOMER software for PCA and correlation analysis using DiffBind software; color gradients indicate sample relatedness. Heatmap shows peaks enriched in group 1 and 2 ATRTs.

(legend continued on next page)

stem cell factor receptor, platelet-derived growth factor receptor (PDGFR), and Src family kinases (Rix et al., 2007). Both drugs are widely used in treatment of leukemia (Kantarjian et al., 2006) and some solid tumors (Araujo and Logothetis, 2010) but have not been extensively investigated in pediatric brain tumors. We therefore tested the sensitivity of ATRT cell lines to dasatinib and nilotinib as gene expression data indicated that *PDGFRB* was most differentially expressed between ATRT subgroups. In contrast to the relative insensitivity of group 2 ATRTs to epigenetic inhibitors, the growth of all five group 2 cell lines tested, including CHLA266 that was reported previously to be dasatinib sensitive (Kolb et al., 2008), was robustly diminished after dasatinib and nilotinib treatment (Figures 6A and 6B). Importantly, neither drug significantly affected the growth of group 1 cell lines. The well-characterized pharmacology of these drugs make them ideal candidates for clinical translation, hence we sought to further investigate the pharmacologic properties and mechanisms underlying the robust effect of both drugs on group 2 ATRT cell growth. Half-maximal inhibitory concentration (IC_{50}) assays revealed group 2 cell lines were up to 1,000 times more sensitive to dasatinib than group 1 cell lines (IC_{50} range 1.01 ± 0.02 to $5.23 \pm 0.13 \mu\text{M}$ versus 3.98 ± 0.90 to 49.95 nM for group 1 and 2, respectively) (Figure 6C). As there are no reports of dasatinib efficacy in brain tumors, we tested dasatinib treatment in vivo using a BT16 orthotopic xenograft model which recapitulates classical rhabdoid morphology (Figure S7C) with predictable engraftment rates. Mice with BT16 xenografts treated with daily intraperitoneal dasatinib (30 mg/kg) injections for 2 weeks had significantly prolonged survival compared with vehicle-treated controls (Figure 6D). Bioluminescence imaging (BLI) of a subset of tumor-bearing mice showed that drug treatment correlated significantly with decreased BLI signals ($p = 0.043$; Figure 6D).

To investigate mechanisms for dasatinib sensitivity, we compared expression of known dasatinib targets in ATRT subtypes. Integrated analyses identified *PDGFRB* as the most significantly differentially expressed locus in group 2 versus group 1 ATRTs (>2-fold change, $p = 6.35 \times 10^{-5}$) (Figure 6E), which was confirmed by western blot analyses of primary ATRTs (Figure 6F). *CSF1R*, which also encodes a potential dasatinib/nilotinib target and maps next to *PDGFRB*, was not differentially expressed or methylated in primary tumors or cell lines. These findings suggested that differential epigenetic regulation leading to *PDGFRB* upregulation may underlie the distinct sensitivity of group 2 cells to dasatinib and nilotinib. Consistent with high *PDGFRB* expression in group 2 ATRTs, ATAC-seq analyses revealed open chromatin at the *PDGFRB* but not the *CSF1R* promoter, specifically in group 2 primary tumors and cell lines (Figures 7A and 7B). Interestingly, ATAC-seq analyses also identified a distinct region of open chromatin in group 2 tumors and cell lines that corresponded to a potential regulatory domain

50 kb upstream of the *PDGFRB* promoter within exon 1 of *CSF1R* (chr5:149,491,285-149,493,716) (Figures 7A and 7B). To examine whether juxtaposition of the *PDGFRB* promoter and putative enhancer by chromatin looping underlies *PDGFRB* upregulation in group 2 ATRTs, we performed C3D analyses on primary tumor ATAC-seq data to evaluate the probability of peak associations (Thurman et al., 2012). The Pearson correlation coefficient calculated for ATAC-seq peaks within a 500 kb window of the *PDGFRB* promoter showed significant correlations between the *PDGFRB* promoter and putative enhancer only in group 2 tumors, T26 (0.5170; $p < 0.0001$) and T27 (0.3028; $p = 0.0067$) (Figure 7C), and strongly supported direct interaction of the *PDGFRB* promoter and putative enhancer specifically in group 2 ATRTs. Detailed analyses of *CSF1R* and *PDGFRB* revealed hypomethylation of six CG residues within the putative enhancer in group 2 tumors and cell lines that correlated significantly with *PDGFRB* but not *CSF1R* expression (Figure 7D). Alignment with ENCODE data indicated features characteristic of enhancers in this region (Filippova et al., 1996; Malik et al., 2014), including differential H3KMe1, H3K4Me3, and H3K27Ac marks, and binding sites for multiple transcription factors including Myc network proteins, FOS and CTCF (Figures 7A and S8A). Together with the significant enrichment of *MYC* and *FOS* expression seen in group 2 ATRTs (Figure S8B), these findings suggest that differential epigenetic regulation of the putative enhancer underlies *PDGFRB* upregulation and distinct group 2 ATRT sensitivity to dasatinib and nilotinib. To confirm and map the putative *PDGFRB* enhancer, we performed H3K27Ac chromatin immunoprecipitation sequencing (ChIP-seq) on two dasatinib/nilotinib-resistant group 1 (CHLA04, 05) cell lines and a representative dasatinib/nilotinib-sensitive group 2 (BT12) cell line. Peak analyses showed that enriched H3K27Ac marks aligned with the predicted enhancer region only in group 2 lines, indicating enhancer activity only in group 2 ATRT cells (Figure 7B). 3C analyses revealed co-enrichment of probes mapping to the *PDGFRB* enhancer and promoter regions in BT12 and CHLA05 cells (Figure 8A). Of note, a second peak in the *PDGFRB* gene body was not associated with H3K27Ac enrichment in BT12 cells. Taken together with the enrichment of H3K27Ac marks at the putative *PDGFRB* enhancer in BT12 but not CHLA04 and 05 cells, these data indicate that direct interaction of a distant active enhancer and promoter via chromatin looping facilitates *PDGFRB* expression in group 2 ATRT cells (Figure 8B). Consistent with these observations, western blot analyses showed high phospho-PDGFRB (pPDGFRB) expression in group 2, but not group 1 ATRT cell lines (Figure 8C), and robust downregulation of pPDGFRB after dasatinib treatment in group 2 cells (Figure 8D). Collectively, our results suggest that epigenetic regulation via differential methylation of a *PDGFRB*-associated enhancer specifically drives the sensitivity of group 2 ATRTs to small-molecule inhibitors of the *PDGFRB* signaling axis and

(B) Genome-wide chromatin openness profiles of group 1 (T4, 13), 2A (T26, 27), and 2B (T45) ATRTs. Differentially open chromatin peaks ($FDR < 0.5$) were identified using DiffBind analysis of ATAC-seq data. Heatmap shows average read density in 20 bp bins (range ± 2.5 kb from peak center) and FPKM values of corresponding genes in individual tumors determined by RNA-seq. The color scale is proportional to read enrichment and normalized between ChIP-seq experiments relative to input DNA.

(C and D) ATAC-seq alignment tracks for subgroup-specific lineage (C) and signaling (D) genes in primary tumors and cell lines. Gene tracks are shown relative to hg19 RefSeq annotation and ATRT molecular group (red, 1; blue, 2A; green, 2B).

See also Table S8.

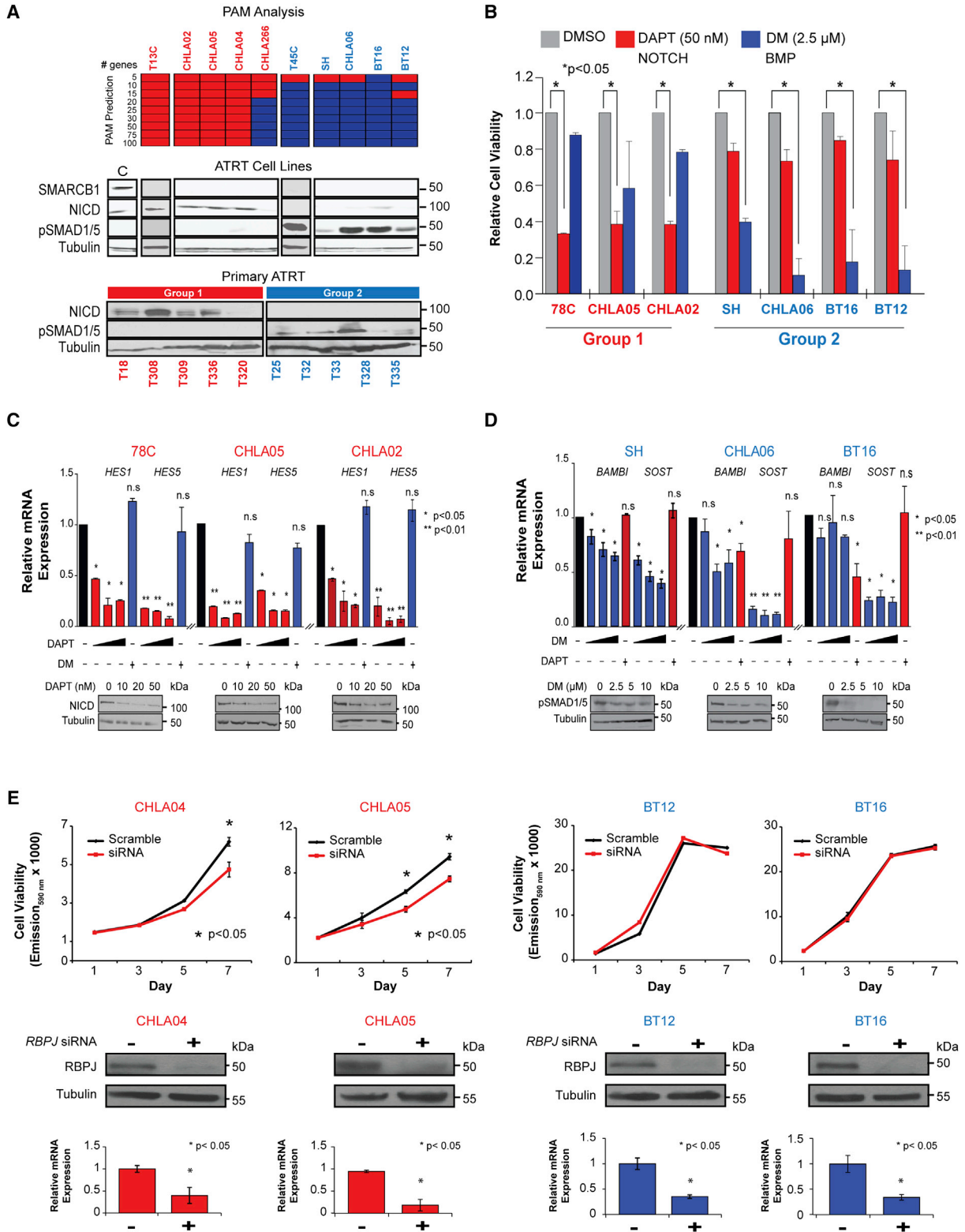


Figure 5. NOTCH and BMP Inhibitors Have Subgroup-Specific Effects on ATRT Cell Growth

(A) Molecular subtype of ten ATRT cell lines is shown with a heatmap of PAM predicted gene classifiers based on primary ATRT gene expression data and western blot analyses of NOTCH intracellular domain (NICD) and pSMAD1/5 expression in cell lines and primary tumors. UW228 medulloblastoma cell line served as a control (C) for SMARCB1 expression; tubulin served as loading control.

(legend continued on next page)

indicate that dasatinib/nilotinib are important agents for the particularly lethal group 2 ATRTs.

DISCUSSION

ATRTs are highly malignant cancers with substantial heterogeneity in disease presentation and poorly defined biology for which best therapeutic approaches are undefined. Here, we demonstrate that ATRTs comprise three epigenetic subtypes that correlate with distinct tumor locations, patient age, lineage-enriched methylation and transcriptional signatures, and unique global and *SMARCB1*-specific genotypes. Our data reveal that ATRT subgroups are associated with a distinct epigenomic landscape and sensitivity to inhibitors of NOTCH, BMP, PDGFRB, and epigenetic signaling. Significantly, we discovered that differential methylation of a *PDGFRB* enhancer underlies the robust and distinct sensitivity of group 2 ATRTs to dasatinib and nilotinib, two well-characterized and widely used cancer drugs.

Cumulative studies indicate that a convergence of epigenomic features reflecting cellular origins and specific somatic alterations underlies diverse tumor phenotypes (Feinberg et al., 2006). Here, we observed that ATRTs segregate into subtypes with specific lineage-enriched methylation signatures, distinct tumor location, and age of presentation suggestive of origins from different neural progenitors. In the predominantly supratentorial group 1 ATRTs, we observed distinct methylation and enrichment of neurogenic loci including forebrain markers *LHX2* (Roy et al., 2014) and *MEIS2* (Ceccconi et al., 1997), as well as *FABP7* and *ASCL1*, markers of radial glial neural progenitors (Anthony et al., 2004), indicating these as potential cell of origins for group 1 ATRTs. In contrast, differentially methylated and expressed loci in group 2 ATRTs were primarily mesenchymal lineage/signaling (*BMP/PDGFRB*) and mid/hindbrain development (*ZIC1*, -2, -4, -5, *OTX2*, *HOXB/C*) genes and suggest that group 2A/B ATRTs, which are primarily infratentorial and spinal tumors, develop from mid/hindbrain neural progenitors. Enrichment of neuronal development pathways in group 1 tumors contrasted with a dominance of stem cell differentiation and pluripotency pathways in group 2A ATRTs. We also observed that, in contrast to group 1 and 2B, group 2A tumors were associated with global CpG island hypomethylation, a more open chromatin landscape and overall increased gene expression patterns reminiscent of more primitive cell types. These data further suggest that group 2A tumors, which arise in the youngest patients (12.00 months 95% CI = 11.05–13.00), originate from highly primitive neural precursors. Our findings corroborate a recent study that also reported three epigenetic subtypes of ATRTs with distinct enhancer landscapes (Johann

et al., 2016), and a study of murine ATRTs derived from a conditional ROSA-Cre model (Han et al., 2016). Our data revealed that ATRTs have rare coding mutations but exhibit subtype-enriched patterns of CNAs and *SMARCB1* genotypes, and suggest different mechanisms of tumor initiation and progression in ATRT subtypes. Notably *SMARCB1* deletions in group 2B ATRTs were frequently accompanied by copy number-driven gene expression changes in candidate modifier loci with neurogenic and epigenetic functions, including *BCR*, *MKL*, and *EP300* (Kaartinen et al., 2001).

As ATRTs lack other recurrent coding alterations, there has been substantial interest in epigenetic therapies for ATRTs. Specifically, promising studies of EZH2 (Knutson et al., 2013) and BET domain (Tang et al., 2014) inhibitors have been reported. Intriguingly, while our screen of small epigenetic inhibitors confirmed the therapeutic effects of UNC1999 and JQ1, respectively EZH2 and BET domain inhibitors, we observed growth inhibitory effects predominantly in group 1 lines. Similarly, we observed that only group 1 lines were sensitive to UNC0638, a chemical compound for histone methyl transferase G9a, while LAQ824, a histone acetylase inhibitor, diminished growth in all cell lines. These findings may reflect more general epigenetic functions of histone deacetylases versus histone methyl transferases. Interestingly, the cellular responses to epigenetic compounds overlapped with the sensitivity to inhibitors of NOTCH and BMP signaling pathways, critical mediators of lineage-specific progenitor cell survival (Ericson et al., 1998). Specifically, group 1 cells with neurogenic transcriptional and epigenomic profiles were sensitive to DAPT, UNC0638, and UNC1999, while group 2 cell lines with limited features of neural differentiation were largely insensitive to these three inhibitors. In contrast, we observed a distinct sensitivity of group 2 cell lines to inhibitors of BMP and PDGFRB, both mediators of mesenchymal signaling. Of note, recent reports indicate a functional and physical interaction of the G9a/GLP and polycomb repressive complex 2 (PRC2) epigenetic silencing machineries and co-regulation of neuronal developmental genes by G9a and PRC2 (Mozzetta et al., 2014). These observations collectively indicate that lineage-associated epigenomic landscapes of ATRTs have critical implications for the development of ATRT subtype-specific therapies. Future investigations to define contributions of other epigenetic modifiers implicated by our genomic and experimental data will clearly be important for informing the development of ATRT therapies.

Our data extend an earlier report of PDGFRA/B expression in some ATRTs and rhabdoid tumor sensitivity to TKIs (Koo et al., 2010). Here, we observed that nilotinib and dasatinib have growth inhibitory effects only in group 2 ATRT cells,

(B) MTS assays of group 1 and 2 cell lines respectively at 3 and 5 days post-treatment with DAPT and dorsomorphin (DM), cell viability is normalized to DMSO-treated controls.

(C and D) Effect of DAPT and DM on NOTCH and BMP signaling in ATRT cells was confirmed by qRT-PCR analyses of respective target genes and western blot analyses for NICD and pSMAD1/5 in group 1 (C) and group 2 (D) cell lines treated with increasing doses (black triangles) of DAPT or DM, and cross-treated with a single dose of DM or DAPT; \pm signs indicate presence or absence of specific drugs. mRNA levels are normalized to actin, and to carrier treated controls (black bars). Significance was calculated using Student's t test.

(E) Cell viability of group 1 (CHLA04, 05) and group 2 (BT12, 16) cell lines treated with RBPJ (25 nM) and scrambled control (20 nM) siRNA were assessed using Alamar blue assays; western blot and qRT-PCR analyses confirmed RBPJ knockdown.

Error bars show \pm SEM (n = 3).

See also Figure S6.

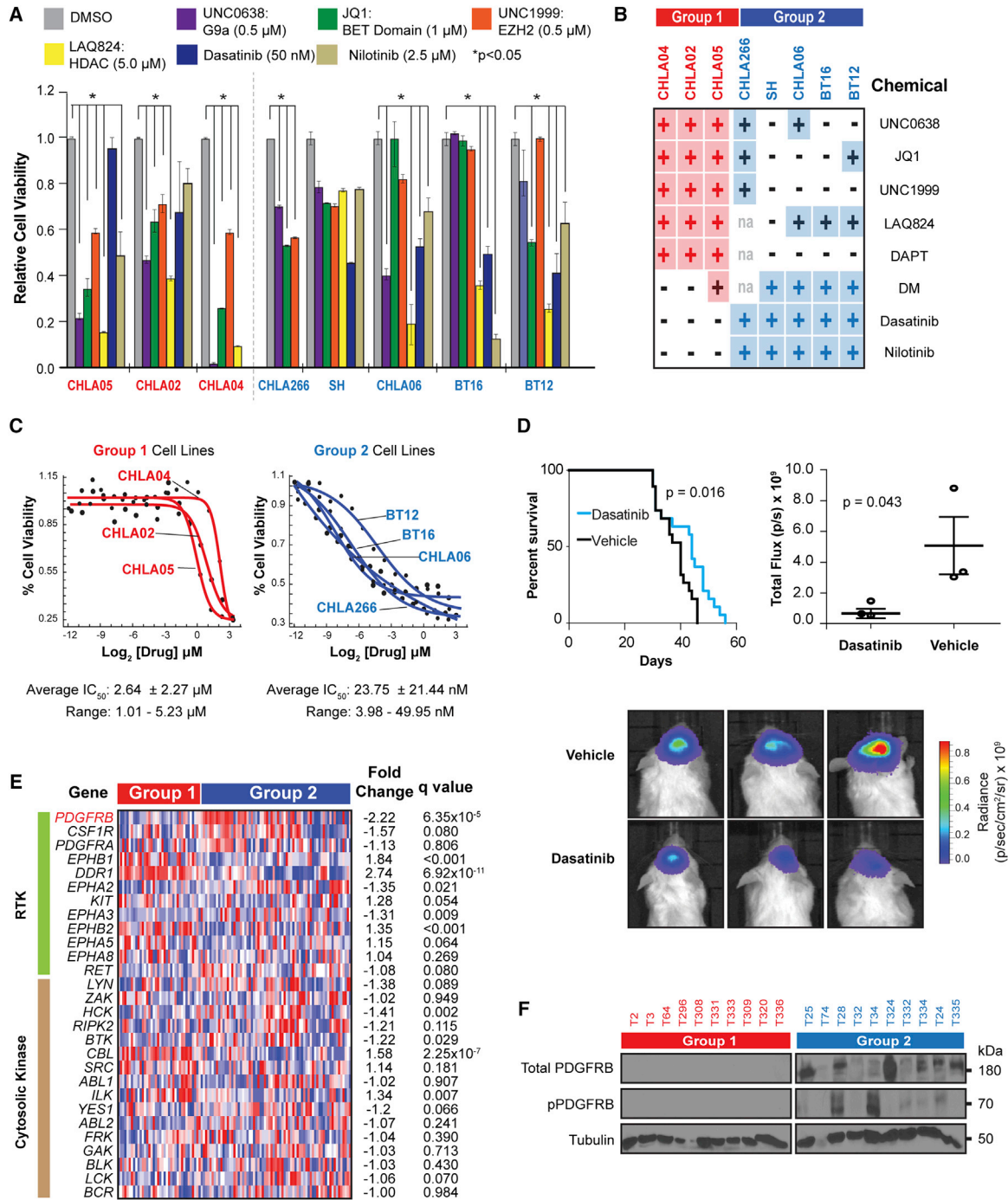


Figure 6. Subgroup-Specific Effect of Signaling and Epigenetic Pathway Inhibitors on ATRT Cell Growth

(A) Cell viability of cell lines treated with indicated small molecules for 7 days was determined by the MTS assays relative to DMSO controls over 5–7 days. Error bars show ±SEM (n = 3).

(B) Summary of MTS assays for cell lines treated with indicated chemicals. + and – indicate > or <30% reduction in cell viability, respectively.

(C) Group 1 and 2 cell lines were treated with 0.3 nM–10 μM dasatinib; IC₅₀ was determined using Alamar blue assays at day 6 post-treatment.

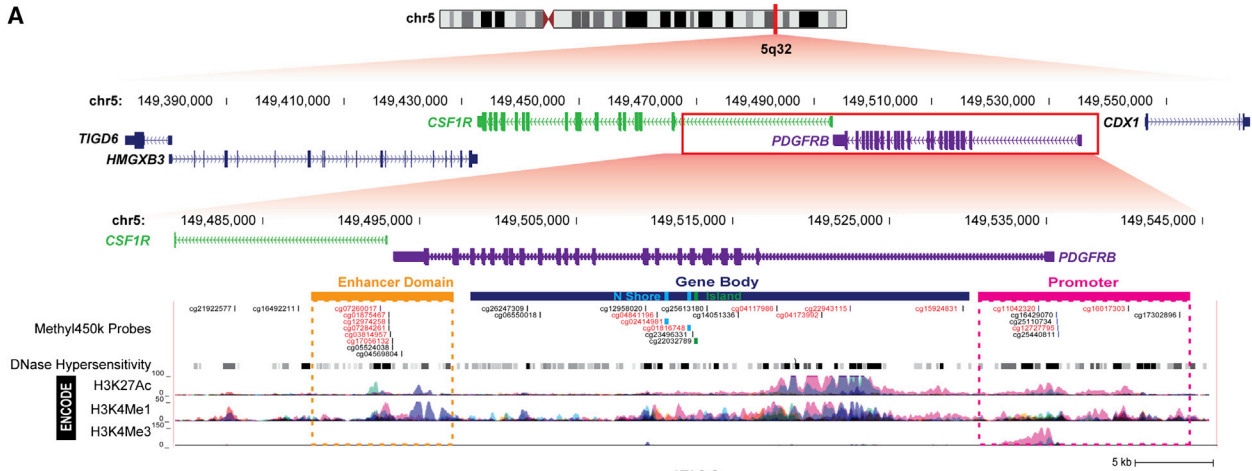
(D) Kaplan-Meier survival analysis of mice with orthotopic BT12 cell line xenografts treated with 30 mg/kg intraperitoneal dasatinib injections for 2 weeks. Dot plot (middle bar represents mean, whiskers represent 10th and 90th percentiles) and BLI images depicting tumor mass at day 21 post-injection in three representative control and treated mice. Differences in survival and tumor growth were assessed using log rank (Mantel-Cox) test and ANOVA analysis, respectively.

(E) Gene expression heatmap of *PDGFRB* (red) and putative receptor (green) and cytosolic tyrosine kinase (brown) targets of dasatinib/nilotinib in ATRTs. Significance was determined by FDR adjusted Student's t test.

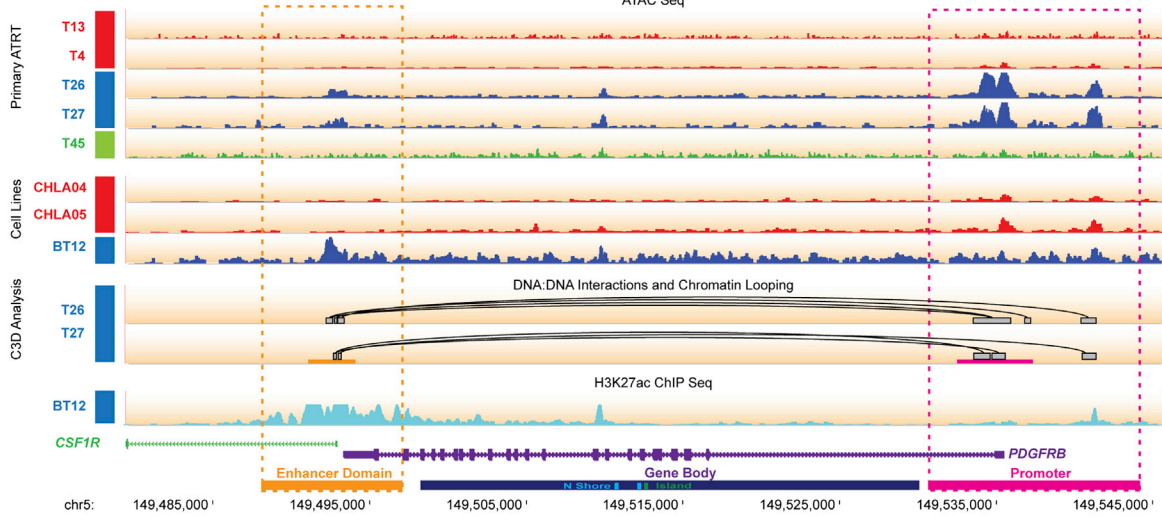
(F) Western blot analyses of total and pPDGFRB in primary ATRTs.

See also Figure S7.

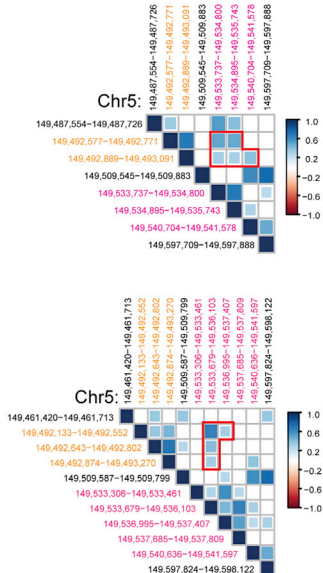
A



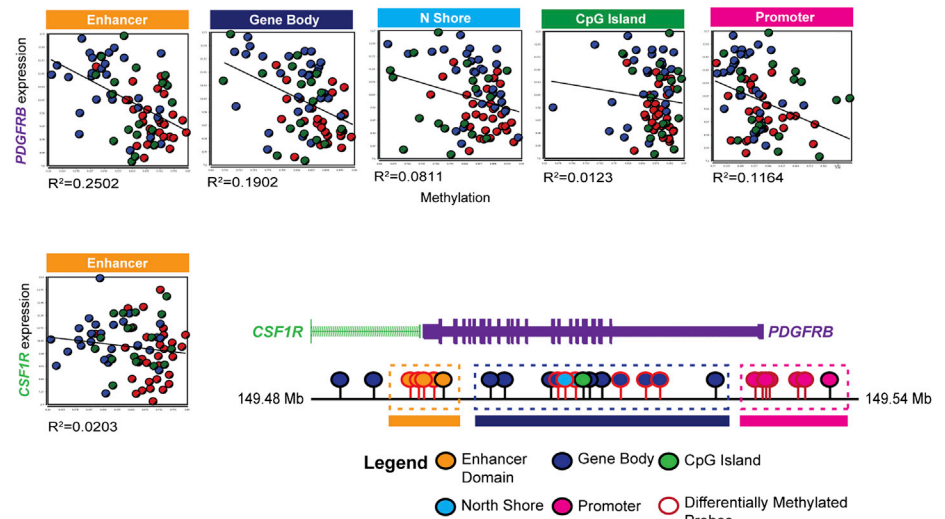
B



C



D



(legend on next page)

including the CHLA266 cell line reported previously to be dasatinib sensitive (Kolb et al., 2008). Importantly, our studies show that dasatinib significantly prolongs the survival of mice with orthotopic group 2 ATRT xenografts, thus indicating that dasatinib can accumulate at a sufficient concentration for tyrosine kinase inhibition in brain tumors. Our studies also suggest that PDGFRB expression is a promising biomarker for dasatinib sensitivity in ATRTs. These findings have significant implications for ATRT treatment as the safety and efficacy of dasatinib are established in adults and children. Interestingly, consistent with the reported enrichment of BMP signaling/mesenchymal lineage genes in non-CNS RTs (Birks et al., 2011; Chun et al., 2016; Gadd et al., 2010), we observed an overlap in the methylation profiles of non-CNS RTs and group 2 ATRTs (data not shown), which suggests that some group 2 ATRTs and non-CNS tumors characteristically seen in very young children with rhabdoid predisposition syndrome, may have common or closely related cellular origins. Indeed, we observed that dasatinib and nilotinib also robustly inhibited the growth of G401, a renal RT cell line (data not shown) and suggest potential roles for dasatinib and nilotinib in non-CNS RT treatment.

Despite evidence of a critical etiologic role for *SMARCB1* in RT initiation, the pathobiology of ATRTs remains poorly elucidated. Our data suggest that *SMARCB1* loss via diverse mechanisms in different cellular contexts, together with additional epigenetic and genetic events, underlies the clinical heterogeneity of human ATRTs. These observations have significant implications for the fundamental understanding and targeting of SWI/SNF function in neoplastic growth and clinical management of ATRTs. Specifically, our analyses, which reveal a spectrum of alterations throughout *SMARCB1*, indicate that current diagnostic methods may underestimate the frequency of *SMARCB1* alterations in ATRTs. We have identified known and potential drugs and drug-like inhibitors with different therapeutic effects in molecular subtypes of ATRTs. In addition to nominating dasatinib and nilotinib as promising repurposed drugs for ATRTs, our comprehensive characterization of ATRT cell lines provides a rich resource for the further development of other candidate ATRT drugs. Most importantly, our study underscores the significant limitations of current chemoradiotherapeutic regimens used uniformly for all ATRT patients. Together with our earlier observations that indicate differential outcomes for molecular subtypes of ATRTs, our study provides a critical framework for informing pre-clinical

studies as well as risk- and biology-stratified clinical trials for ATRTs.

EXPERIMENTAL PROCEDURES

Tumor and Patient Information

All tumors and clinical information were collected through an international collaborative network (see Supplemental Experimental Procedures) with consent as per protocols approved by the Hospital Research Ethics Board at participating institutions. In total, 194 CNS (191 primary and 3 recurrent) and 9 non-CNS RT samples were collected for genomic analyses (Table S3). All ATRTs were diagnosed according to the World Health Organization CNS tumor classification criteria (Louis and Wiestler, 2007) and confirmed by BAF47 immunostains (BD Biosciences, catalog no. 612110). Biallelic *SMARCB1* alterations were confirmed using FISH, MLPA, targeted exons 1–9 Sanger sequencing, or WGS/WES analyses. DNA or RNA from snap frozen tumor were investigated with one or more of WGS/WES, RNA-seq and high-resolution copy number/SNP, gene expression, and methylation array analyses; 123 samples with DNA from formalin-fixed, paraffin-embedded materials were analyzed with the Illumina 450k methylation arrays. Animal studies were conducted in accordance with the policies and regulations for ethical treatment of animals approved for the Toronto Center for Phenogenomics.

Statistical Analyses

Difference in nucleotide transition/transversion rates from WGS SNV calls were determined using the two-proportion Z test with Yates' correction for continuity. Significance of differences in gender, location, metastasis, and individual genomic loci between ATRT subgroups were analyzed using a two-sided Fisher's exact test. The Kruskal-Wallis test was used to assess the significance of tumor subgroups in relation to age and counts of genomic alterations. Student's t test and the Mann-Whitney-Wilcoxon test with false discovery rate (FDR) correction were used, respectively, to test for differences in gene expression and methylation between groups. All analyses were conducted in the R statistical environment (v2.15.2) or with SPSS version 22.0. A p value of <0.05 was regarded as significant for all analyses.

ACCESSION NUMBERS

Data for whole-genome/exome DNA and RNA sequencing, ChIP sequencing for H3K27Ac, ATAC sequencing, gene expression, methylation and SNP genotyping array data have been deposited at the European Genome-Phenome Archive, EGA Study Accession ID EGAS00001000506.

SUPPLEMENTAL INFORMATION

Supplemental Information includes Supplemental Experimental Procedures, eight figures, and eight tables and can be found with this article online at <http://dx.doi.org/10.1016/j.ccell.2016.11.003>.

Figure 7. A *PDGFRB* Enhancer Element Exhibits Differential Methylation and Chromatin Association in Group 2 ATRTs

(A) Schema of *CSF1R* (green) and *PDGFRB* (purple) relative to UCSC and/or ENCODE tracks and flanking genes (chr5:149,370,252–149,566,612) with a zoomed view of putative enhancer relative to exon 1 and gene body of *CSF1R* (blue) and *PDGFRB* promoter (purple) (chr5:149,479,360–149,545,365), 450k probe locations, DNase hypersensitivity, and ENCODE cell line tracks for H3K27Ac, H3K4Me1, and H3K4Me3 ChIP-seq data. Probes in *PDGFRB* promoter and putative enhancer with relative hypomethylation in group 2 ATRTs is shown in red font and dashed pink and orange boxes.

(B) ATAC-seq signal for *CSF1R/PGFRB* in primary ATRTs and cell line data is shown with C3D predicted associations (curved lines) of *PDGFRB* enhancer and promoter (boxed). Bottom track shows H3K27Ac ChIP-seq signal for BT12, a dasatinib-sensitive group 2 cell line. Group 1, 2A, and 2B primary ATRTs and cell lines are indicated in red, blue, and green, respectively.

(C) Correlation matrix of associated open chromatin regions in a 120 kb window around the *PDGFRB* promoter predicted by C3D analysis of ATAC-seq data from tumors T26 (top panel) and T27 (bottom panel). Absolute correlation is shown proportional to size of colored squares, positive and negative correlations are indicated in blue and red, respectively. All correlations were tested within a 500 kb window of *PDGFRB* promoter and adjusted for statistical significance (FDR method); blank squares indicate insignificant correlations.

(D) Pearson's correlation/linear regression analyses of *PDGFRB* and *CSF1R* gene expression (\log_2 , y axis) and methylation levels (β value, x axis) at the enhancer domain, *PDGFRB* gene body, North (N) shore, CpG island, and *PDGFRB* promoter. Location of differentially methylated *CSF1R-PDGFRB* probes based on 450k array data of 75 ATRTs is schematized.

See also Figure S8.

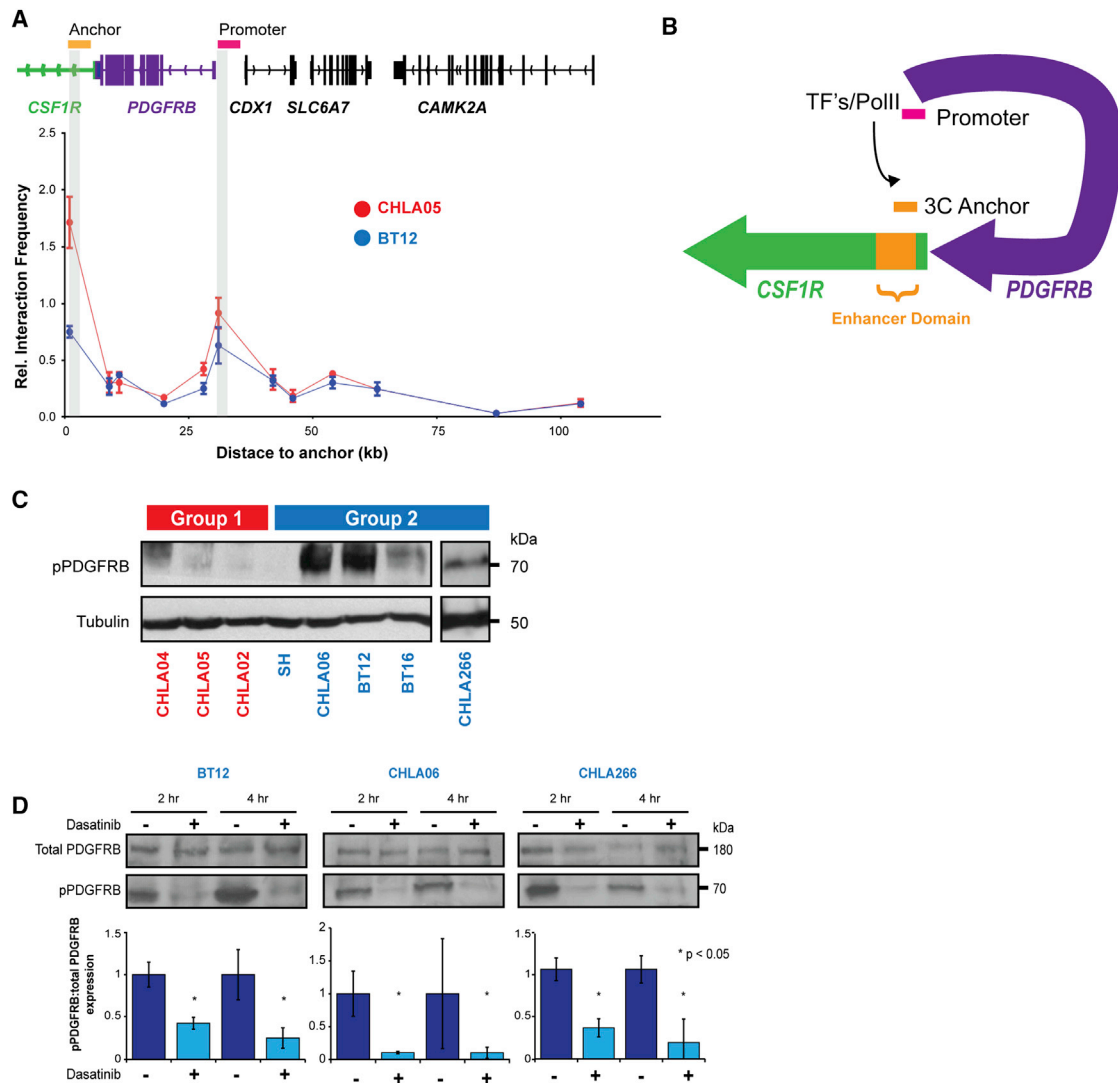


Figure 8. A Promoter-Enhancer Loop Regulates *PDGFRB* Expression and Confers Dasatinib/Nilotinib Sensitivity in Group 2 ATRT

(A) 3C analyses of *PDGFRB* enhancer:promoter interaction in ATRT cell lines CHLA05 (red) and BT12 (blue). Plot indicates relative co-amplification and interaction frequency of an anchor primer in the putative enhancer with test primers located at various distances in the *CSF1R*/*PDGFRB* gene body and promoter (gray bars).

(B) Schema of 3C analysis indicating DNA looping and direct interaction of *PDGFRB* promoter and an enhancer 50 kb upstream.

(C) Western blot analyses of pPDGFRB expression in ATRT cell lines.

(D) Western blot and corresponding densitometric analyses of total and pPDGFRB expression in group 2 cell lines post-treatment with 50 nM of dasatinib (+) and DMSO (-). Error bars show \pm SEM (n = 3).

AUTHOR CONTRIBUTIONS

A.H., D.D.C., N.J., and J.T.R. conceived the projects. J.T. analyzed WGS/WES data assisted by L.L., M.B., S.M., A.V., B.G., M.D., P.S.C., and supervised by A.H., G.D.B., A.M., G.Bu., N.J., and M.Br. A.H. supervised RNA-seq analyses by J.T., D.M.G., and J.D.N.; gene expression and correlative analyses were carried out by J.T. with assistance from D.P. and G.D.B.; methylation data were collected by J.T. with assistance from D.P. and D.K.Q. ATAC and ChIP assays were performed by S.F., C.Z., K.C.H., T.M., and N.R.A. under supervision of D.D.C. Cellular, biochemical assays, and xenograft studies were performed by B.G., L.G., P.A., and K.C.H. with help from N.R.A., M.L., and M.Y. and supervised by A.H. A.C.P. performed 3C experiments supervised by D.D.C. J.T. performed analysis of ChIP and ATAC-seq data supervised by A.H. and D.D.C. in consultation with Ma.L. and P.G. Sequencing

validation was performed under supervision of A.M., all other validation experiments were performed by B.G. and K.C.H. with assistance from T.S.C., A.N.R., and M.Y. under the supervision of A.H. and J.T.R. D.B., L.L.-C., Y.R., V.R., M.R., C.P.D., S.Y., H.-k.N., J.L., S.A., J.P., J.A.C., G.R.S., C.C.F., L.R., M.F., L.M.H., A.S.M., Y.W., S.A.C., J.R.H., D.C., D.K.B., N.F., D.S., A.K., M.G., P.H., T.H., L.B., B.W., J.H., A.C., T.E.V., E.I.H., S.C., H.N., H.T., I.F., H.D., D.F., T.W., C.F., D.D.E., K.S., D.J., J.M., S.Z., R.H., D.A.R., A.J.F., N.S., N.L., S.H., R.R.L., J.R.F., U.B., R.G., Da.M., U.S., T.N., T.T., J.Ph., J.Ma., S.Af., A.T.R., M.W.M., J.C.M., S.R., Y.G.G., M.D.T., U.T., T.P., A.R.J., E.B., S.K., A.E., P.D., and C.H.A. provided tumor materials/clinical data, and/or cell lines used in this study. Statistical analyses were performed by J.T. Histopathological analyses were performed by C.E.H. and M.Ba. J.T. and A.H. wrote the manuscript with input from B.G., D.D.C., N.J., and J.T.R.

ACKNOWLEDGMENTS

This work was supported by funds from Genome Canada, 110814 (A.H. and N.J.), CCSRI #703279 (A.H. and D.D.C.), b.r.a.i.n.child, Mitchell Duckman, Tal Doron, and Suri Boon foundations (A.H. and J.T.R.) and C17 Childhood Cancer and Blood Disorders Research Network (L.L.C., E.B., A.H.). J.T. and P.S.C. are Ontario Graduate Scholars; D.G. and J.D.N. are, respectively, Brain Canada and CIHR Research Fellows. Technical support from V. Lau, A. Ma, and staff of the McGill University and G enome Qu ebec Innovation Center, the Princess Margaret Genomics Center, the Center for Applied Genomics Toronto, the Rare Brain Tumor Consortium (<http://www.rarebraintumorconsortium.ca>), tumor banks of contributing centers (Table S8), and tissue contributions from Dr. A. Korshunov are gratefully acknowledged.

Received: January 6, 2016

Revised: September 19, 2016

Accepted: October 31, 2016

Published: December 12, 2016

REFERENCES

- Anthony, T.E., Klein, C., Fishell, G., and Heintz, N. (2004). Radial glia serve as neuronal progenitors in all regions of the central nervous system. *Neuron* *41*, 881–890.
- Araujo, J., and Logothetis, C. (2010). Dasatinib: a potent SRC inhibitor in clinical development for the treatment of solid tumors. *Cancer Treat. Rev.* *36*, 492–500.
- Birks, D.K., Donson, A.M., Patel, P.R., Dunham, C., Muscat, A., Algar, E.M., Ashley, D.M., Kleinschmidt-Demasters, B.K., Vibhakar, R., Handler, M.H., and Foreman, N.K. (2011). High expression of BMP pathway genes distinguishes a subset of atypical teratoid/rhabdoid tumors associated with shorter survival. *Neurooncol.* *13*, 1296–1307.
- Bourdeaut, F., Lequin, D., Brugieres, L., Reynaud, S., Dufour, C., Doz, F., Andre, N., Stephan, J.L., Perel, Y., Oberlin, O., et al. (2011). Frequent hSNF5/INI1 germline mutations in patients with rhabdoid tumor. *Clin. Cancer Res.* *17*, 31–38.
- Cecconi, F., Proetzel, G., Alvarez-Bolado, G., Jay, D., and Gruss, P. (1997). Expression of Meis2, a Knotted-related murine homeobox gene, indicates a role in the differentiation of the forebrain and the somitic mesoderm. *Dev. Dyn.* *210*, 184–190.
- Chi, S.N., Zimmerman, M.A., Yao, X., Cohen, K.J., Burger, P., Biegel, J.A., Rorke-Adams, L.B., Fisher, M.J., Janss, A., Mazewski, C., et al. (2009). Intensive multimodality treatment for children with newly diagnosed CNS atypical teratoid rhabdoid tumor. *J. Clin. Oncol.* *27*, 385–389.
- Chun, H.J., Lim, E.L., Heravi-Moussavi, A., Saberi, S., Mungall, K.L., Bilenky, M., Carles, A., Tse, K., Shlafman, I., Zhu, K., et al. (2016). Genome-wide profiles of extra-cranial malignant rhabdoid tumors reveal heterogeneity and dysregulated developmental pathways. *Cancer Cell* *29*, 394–406.
- Eaton, K.W., Tooke, L.S., Wainwright, L.M., Judkins, A.R., and Biegel, J.A. (2011). Spectrum of SMARCB1/INI1 mutations in familial and sporadic rhabdoid tumors. *Pediatr. Blood Cancer* *56*, 7–15.
- Ericson, J., Norlin, S., Jessell, T.M., and Edlund, T. (1998). Integrated FGF and BMP signaling controls the progression of progenitor cell differentiation and the emergence of pattern in the embryonic anterior pituitary. *Development* *125*, 1005–1015.
- Feinberg, A.P., Ohlsson, R., and Henikoff, S. (2006). The epigenetic progenitor origin of human cancer. *Nat. Rev. Genet.* *7*, 21–33.
- Filippova, G.N., Fagerlie, S., Klenova, E.M., Myers, C., Dehner, Y., Goodwin, G., Neiman, P.E., Collins, S.J., and Lobanenkov, V.V. (1996). An exceptionally conserved transcriptional repressor, CTCF, employs different combinations of zinc fingers to bind diverged promoter sequences of avian and mammalian c-myc oncogenes. *Mol. Cell Biol.* *16*, 2802–2813.
- Gadd, S., Sredni, S.T., Huang, C.-C., and Perlman, E.J.; Group, Renal Tumor Committee of the Children's Oncology Group (2010). Rhabdoid tumor: gene expression clues to pathogenesis and potential therapeutic targets. *Lab. Invest.* *90*, 724–738.
- Geling, A., Steiner, H., Willem, M., Bally-Cuif, L., and Haass, C. (2002). A gamma-secretase inhibitor blocks Notch signaling in vivo and causes a severe neurogenic phenotype in zebrafish. *EMBO Rep.* *3*, 688–694.
- Ginn, K.F., and Gajjar, A. (2012). Atypical teratoid rhabdoid tumor: current therapy and future directions. *Front. Oncol.* *2*, 114.
- Han, Z.Y., Richer, W., Freneaux, P., Chauvin, C., Lucchesi, C., Guillemot, D., Grison, C., Lequin, D., Pierron, G., Masliah-Planchon, J., et al. (2016). The occurrence of intracranial rhabdoid tumours in mice depends on temporal control of Smarcb1 inactivation. *Nat. Commun.* *7*, 10421.
- Hasselblatt, M., Gesk, S., Oyen, F., Rossi, S., Viscardi, E., Giangaspero, F., Giannini, C., Judkins, A.R., Fruhwald, M.C., Obser, T., et al. (2011). Nonsense mutation and inactivation of SMARCA4 (BRG1) in an atypical teratoid/rhabdoid tumor showing retained SMARCB1 (INI1) expression. *Am. J. Surg. Pathol.* *35*, 933–935.
- Hilden, J.M. (2004). Central nervous system atypical teratoid/rhabdoid tumor: results of therapy in children enrolled in a registry. *J. Clin. Oncol.* *22*, 2877–2884.
- Jackson, E.M., Sievert, A.J., Gai, X., Hakonarson, H., Judkins, A.R., Tooke, L., Perin, J.C., Xie, H., Shaikh, T.H., and Biegel, J.A. (2009). Genomic analysis using high-density single nucleotide polymorphism-based oligonucleotide arrays and multiplex ligation-dependent probe amplification provides a comprehensive analysis of INI1/SMARCB1 in malignant rhabdoid tumors. *Clin. Cancer Res.* *15*, 1923–1930.
- Johann, P.D., Erkek, S., Zapatka, M., Kerl, K., Buchhalter, I., Hovestadt, V., Jones, D.T., Sturm, D., Hermann, C., Segura Wang, M., et al. (2016). Atypical teratoid/rhabdoid tumors are comprised of three epigenetic subgroups with distinct enhancer landscapes. *Cancer Cell* *29*, 379–393.
- Kaartinen, V., Gonzalez-Gomez, I., Voncken, J.W., Haataja, L., Faure, E., Nagy, A., Groffen, J., and Heisterkamp, N. (2001). Abnormal function of astroglia lacking Abr and Bcr RacGAPs. *Development* *128*, 4217–4227.
- Kantarjian, H., Giles, F., Wunderle, L., Bhalla, K., O'Brien, S., Wassmann, B., Tanaka, C., Manley, P., Rae, P., Mietlowski, W., et al. (2006). Nilotinib in imatinib-resistant CML and Philadelphia chromosome-positive ALL. *N. Engl. J. Med.* *354*, 2542–2551.
- Kim, K.H., and Roberts, C.W. (2016). Targeting EZH2 in cancer. *Nat. Med.* *22*, 128–134.
- Klochendler-Yeivin, A., Fiette, L., Barra, J., Muchardt, C., Babinet, C., and Yaniv, M. (2000). The murine SNF5/INI1 chromatin remodeling factor is essential for embryonic development and tumor suppression. *EMBO Rep.* *1*, 500–506.
- Knudson, S.K., Warholic, N.M., Wigle, T.J., Klaus, C.R., Allain, C.J., Raimondi, A., Porter Scott, M., Chesworth, R., Moyer, M.P., Copeland, R.A., et al. (2013). Durable tumor regression in genetically altered malignant rhabdoid tumors by inhibition of methyltransferase EZH2. *Proc. Natl. Acad. Sci. USA* *110*, 7922–7927.
- Kolb, E.A., Gorlick, R., Houghton, P.J., Morton, C.L., Lock, R.B., Tajbakhsh, M., Reynolds, C.P., Maris, J.M., Keir, S.T., Billups, C.A., and Smith, M.A. (2008). Initial testing of dasatinib by the pediatric preclinical testing program. *Pediatr. Blood Cancer* *50*, 1198–1206.
- Koos, B., Jeibmann, A., Lunenburger, H., Mertsch, S., Nupponen, N.N., Roselli, A., Leuschner, I., Paulus, W., Fruhwald, M.C., and Hasselblatt, M. (2010). The tyrosine kinase c-Abl promotes proliferation and is expressed in atypical teratoid and malignant rhabdoid tumors. *Cancer* *116*, 5075–5081.
- Lafay-Cousin, L., Hawkins, C., Carret, A.S., Johnston, D., Zelcer, S., Wilson, B., Jabado, N., Scheinmann, K., Eisenstat, D., Fryer, C., et al. (2012). Central nervous system atypical teratoid rhabdoid tumours: the Canadian Paediatric Brain Tumour Consortium experience. *Eur. J. Cancer* *48*, 353–359.
- Lee, R.S., Stewart, C., Carter, S.L., Ambrogio, L., Cibulskis, K., Sougnez, C., Lawrence, M.S., Auclair, D., Mora, J., Golub, T.R., et al. (2012). A remarkably simple genome underlies highly malignant pediatric rhabdoid cancers. *J. Clin. Invest.* *122*, 2983–2988.
- Louis, D.N., and Wiestler, O.D. (2007). WHO Classification of Tumours of the Central Nervous System, Fourth Edition (IARC).

- Malik, A.N., Vierbuchen, T., Hemberg, M., Rubin, A.A., Ling, E., Couch, C.H., Stroud, H., Spiegel, I., Farh, K.K., Harmin, D.A., and Greenberg, M.E. (2014). Genome-wide identification and characterization of functional neuronal activity-dependent enhancers. *Nat. Neurosci.* *17*, 1330–1339.
- Mozzetta, C., Pontis, J., Fritsch, L., Robin, P., Portoso, M., Proux, C., Margueron, R., and Ait-Si-Ali, S. (2014). The histone H3 lysine 9 methyltransferases G9a and GLP regulate polycomb repressive complex 2-mediated gene silencing. *Mol. Cell* *53*, 277–289.
- Rix, U., Hantschel, O., Durnberger, G., Rensing Rix, L.L., Planyavsky, M., Fernbach, N.V., Kaupe, I., Bennett, K.L., Valent, P., et al. (2007). Chemical proteomic profiles of the BCR-ABL inhibitors imatinib, nilotinib, and dasatinib reveal novel kinase and nonkinase targets. *Blood* *110*, 4055–4063.
- Roberts, C.W., and Orkin, S.H. (2004). The SWI/SNF complex–chromatin and cancer. *Nat. Rev. Cancer* *4*, 133–142.
- Roberts, C.W., Leroux, M.M., Fleming, M.D., and Orkin, S.H. (2002). Highly penetrant, rapid tumorigenesis through conditional inversion of the tumor suppressor gene *Snf5*. *Cancer Cell* *2*, 415–425.
- Roy, A., Gonzalez-Gomez, M., Pierani, A., Meyer, G., and Tole, S. (2014). *Lhx2* regulates the development of the forebrain hem system. *Cereb. Cortex* *24*, 1361–1372.
- Tang, Y., Gholamin, S., Schubert, S., Willardson, M.I., Lee, A., Bandopadhyay, P., Bergthold, G., Masoud, S., Nguyen, B., Vue, N., et al. (2014). Epigenetic targeting of Hedgehog pathway transcriptional output through BET bromodomain inhibition. *Nat. Med.* *20*, 732–740.
- Tekautz, T.M. (2005). Atypical teratoid/rhabdoid tumors (ATRT): improved survival in children 3 years of age and older with radiation therapy and high-dose alkylator-based chemotherapy. *J. Clin. Oncol.* *23*, 1491–1499.
- Thurman, R.E., Rynes, E., Humbert, R., Vierstra, J., Maurano, M.T., Haugen, E., Sheffield, N.C., Stergachis, A.B., Wang, H., Vernot, B., et al. (2012). The accessible chromatin landscape of the human genome. *Nature* *489*, 75–82.
- Torchia, J., Picard, D., Lafay-Cousin, L., Hawkins, C.E., Kim, S.K., Letourneau, L., Ra, Y.S., Ho, K.C., Chan, T.S., Sin-Chan, P., et al. (2015). Molecular subgroups of atypical teratoid rhabdoid tumours in children: an integrated genomic and clinicopathological analysis. *Lancet Oncol.* *16*, 569–582.
- Versteeg, I., Sévenet, N., Lange, J., Rousseau-Merck, M.F., Ambros, P., Handgretinger, R., Aurias, A., and Delattre, O. (1998). Truncating mutations of *hSNF5/INI1* in aggressive paediatric cancer. *Nature* *394*, 203–206.
- Wilson, B.G., Wang, X., Shen, X., McKenna, E.S., Lemieux, M.E., Cho, Y.-J., Koellhoffer, E.C., Pomeroy, S.L., Orkin, S.H., and Roberts, C.W.M. (2010). Epigenetic antagonism between polycomb and SWI/SNF complexes during oncogenic transformation. *Cancer Cell* *18*, 316–328.
- Yu, P.B., Hong, C.C., Sachidanandan, C., Babitt, J.L., Deng, D.Y., Hoyng, S.A., Lin, H.Y., Bloch, K.D., and Peterson, R.T. (2008). Dorsomorphin inhibits BMP signals required for embryogenesis and iron metabolism. *Nat. Chem. Biol.* *4*, 33–41.

Supplemental Information

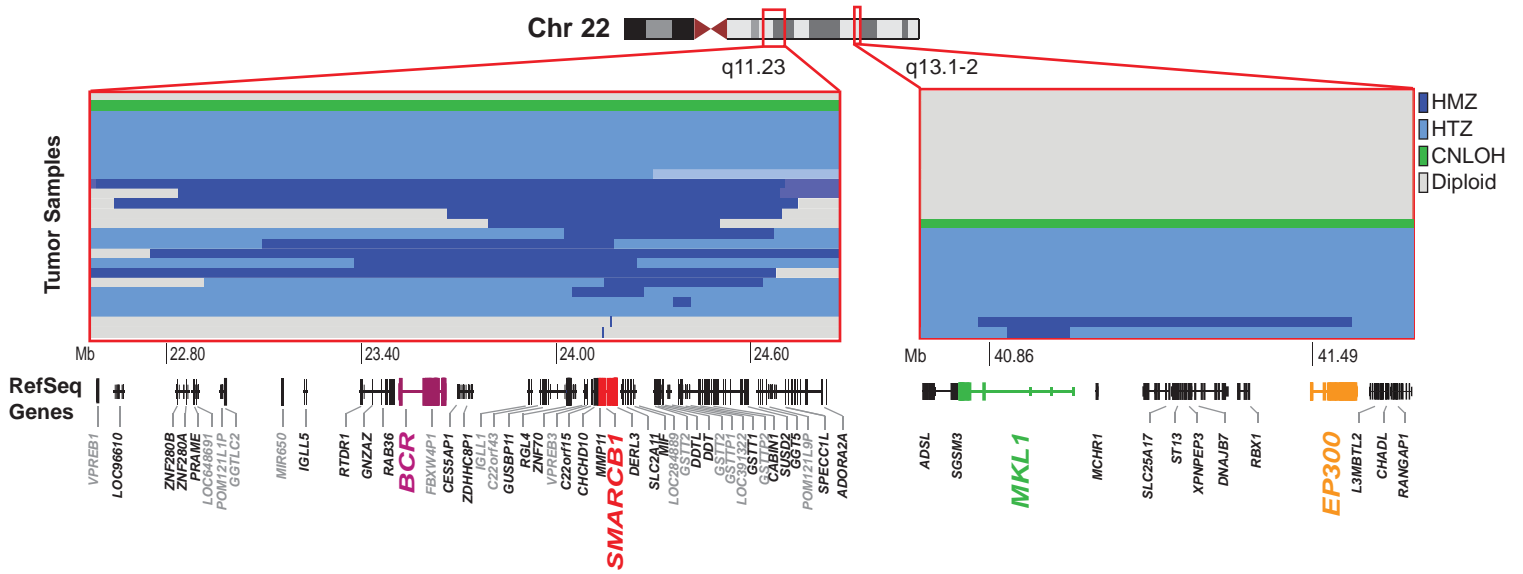
Integrated (epi)-Genomic Analyses Identify

Subgroup-Specific Therapeutic Targets

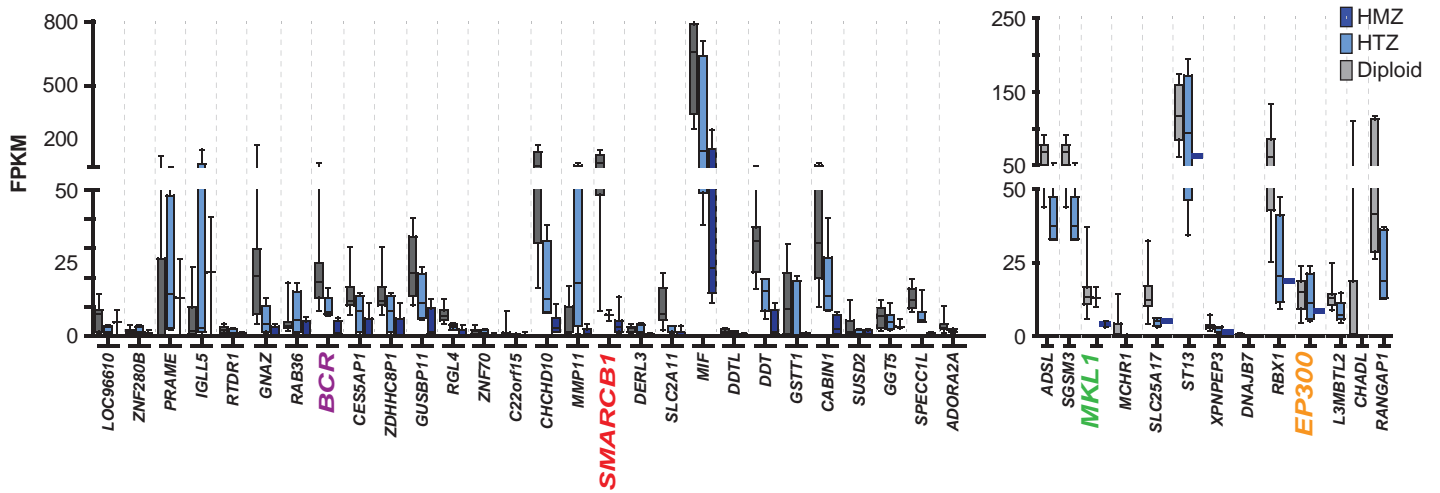
in CNS Rhabdoid Tumors

Jonathon Torchia, Brian Golbourn, Shengrui Feng, King Ching Ho, Patrick Sin-Chan, Alexandre Vasiljevic, Joseph D. Norman, Paul Guilhamon, Livia Garzia, Natalia R. Agamez, Mei Lu, Tiffany S. Chan, Daniel Picard, Pasqualino de Antonellis, Dong-Anh Khuong-Quang, Aline C. Planello, Constanze Zeller, Dalia Barsyte-Lovejoy, Lucie Lafay-Cousin, Louis Letourneau, Mathieu Bourgey, Man Yu, Deena M.A. Gendoo, Misko Dzamba, Mark Barszczyk, Tiago Medina, Alexandra N. Riemenschneider, A. Sorana Morrissy, Young-Shin Ra, Vijay Ramaswamy, Marc Remke, Christopher P. Dunham, Stephen Yip, Ho-keung Ng, Jian-Qiang Lu, Vivek Mehta, Steffen Albrecht, Jose Pimentel, Jennifer A. Chan, Gino R. Somers, Claudia C. Faria, Lucia Roque, Maryam Fouladi, Lindsey M. Hoffman, Andrew S. Moore, Yin Wang, Seung Ah Choi, Jordan R. Hansford, Daniel Catchpoole, Diane K. Birks, Nicholas K. Foreman, Doug Strother, Almos Klekner, Laszlo Bognár, Miklós Garami, Péter Hauser, Tibor Hortobágyi, Beverly Wilson, Juliette Hukin, Anne-Sophie Carret, Timothy E. Van Meter, Eugene I. Hwang, Amar Gajjar, Shih-Hwa Chiou, Hideo Nakamura, Helen Toledano, Iris Fried, Daniel Fults, Takafumi Wataya, Chris Fryer, David D. Eisenstat, Katrin Scheinemann, Adam J. Fleming, Donna L. Johnston, Jean Michaud, Shayna Zelcer, Robert Hammond, Samina Afzal, David A. Ramsay, Nongnuch Sirachainan, Suradej Hongeng, Noppadol Larbcharoensub, Richard G. Grundy, Rishi R. Lulla, Jason R. Fangusaro, Harriet Druker, Ute Bartels, Ronald Grant, David Malkin, C. Jane McGlade, Theodore Nicolaides, Tarik Tihan, Joanna Phillips, Jacek Majewski, Alexandre Montpetit, Guillaume Bourque, Gary D. Bader, Alyssa T. Reddy, G. Yancey Gillespie, Monika Warmuth-Metz, Stefan Rutkowski, Uri Tabori, Mathieu Lupien, Michael Brudno, Ulrich Schüller, Torsten Pietsch, Alexander R. Judkins, Cynthia E. Hawkins, Eric Bouffet, Seung-Ki Kim, Peter B. Dirks, Michael D. Taylor, Anat Erdreich-Epstein, Cheryl H. Arrowsmith, Daniel D. De Carvalho, James T. Rutka, Nada Jabado, and Annie Huang

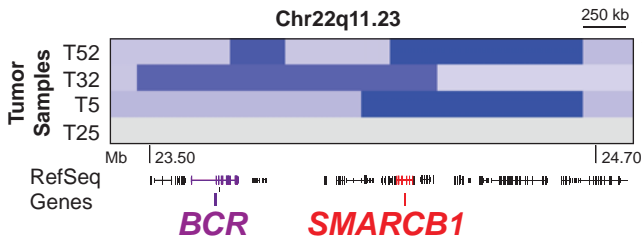
A



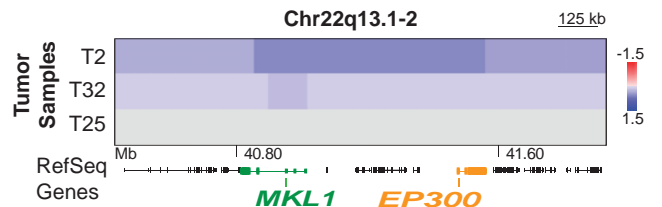
B



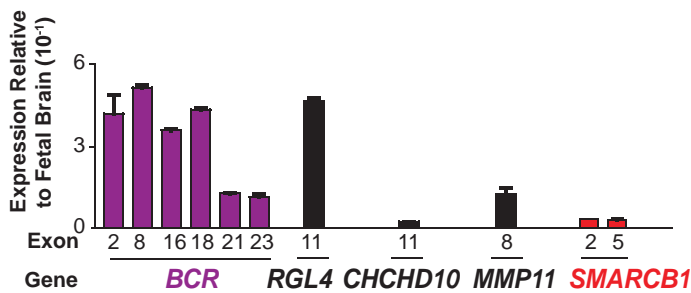
C



E



D



F

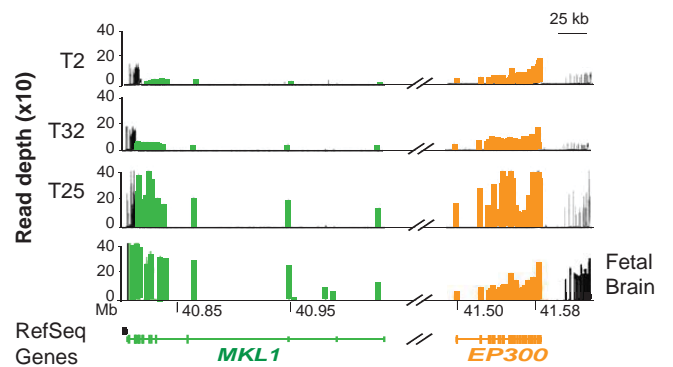


Figure S1, related to Figure 1. Copy number-driven gene expression changes on chr 22

(A) Composite heat map of recurrent chr22 SCNAs in ATRTs. Chr22 copy number status was determined for a subset of 25 ATRTs with matching RNA-seq data, by multiple methods including Illumina OmniQuad SNP and 450k methylation array and whole genome sequence analyses (see methods). Genes with insignificant expression levels in all ATRTs, based on gene expression arrays/RNA-seq and/or RT-PCR analyses, are indicated in grey. Relative positions of RefSeq loci are indicated.

(B) Plots of FPKM values for genes in the chr22q11.23 and q13.1-2 interval, grouped by copy number status. Boxplot middle represents mean, box boundaries represent 1st and 3rd quartiles and whiskers represent 10th and 90th percentiles.

(C) Heat map of contiguous and non-contiguous deletions of *BCR* and *SMARCB1* in ATRT T52, T32 and T5, shown relative to ATRT T25, which is diploid for chr 22 and harbours a *SMARCB1* point mutation.

(D) qRT-PCR analyses confirming a focal, non-contiguous deletion of *BCR* and *SMARCB1* in ATRT T52. Expression of specific *BCR* and *SMARCB1* exons and intervening loci, *RGL4*, *CHCHD10* and *MMP11* were determined relative to a normal fetal brain control using the $\Delta\Delta CT$ method, error bars depict \pm SD (n=3).

(E) Heat map of overlapping focal heterozygous *MKL1* and *EP300* deletions in ATRT T2 and T32 is shown relative to tumor T25 diploid for both genes with corresponding RefSeq gene tracks and genomic positions indicated.

(F) RNA-seq read depths plots for *MKL1* (green) and *EP300* (orange) exons in ATRT T2, T32, T25 and control fetal brain relative to RefSeq gene tracks.

Table S1, related to Figure 1. Provided as a separate Excel file. Summary of whole genome/exome and RNA-seq analyses

Table S2, related to Figure 1. Provided as a separate Excel file. Summary of alterations in ATRTs

Table S3, related to Figure 1. Provided as a separate Excel file. Summary of genomic analyses and clinical information of ATRT samples

Table S4, related to Figure 1. Provided as a separate Excel file. Summary of recurrent focal somatic genetic alterations in ATRTs

Table S5, related to Figure 1. Provided as a separate Excel file. Details of *SMARCB1* gene alterations

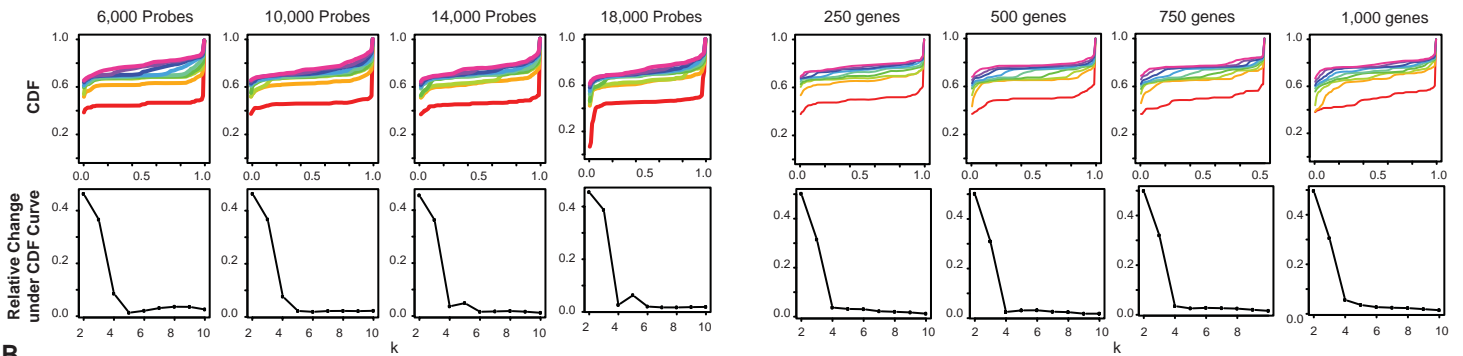
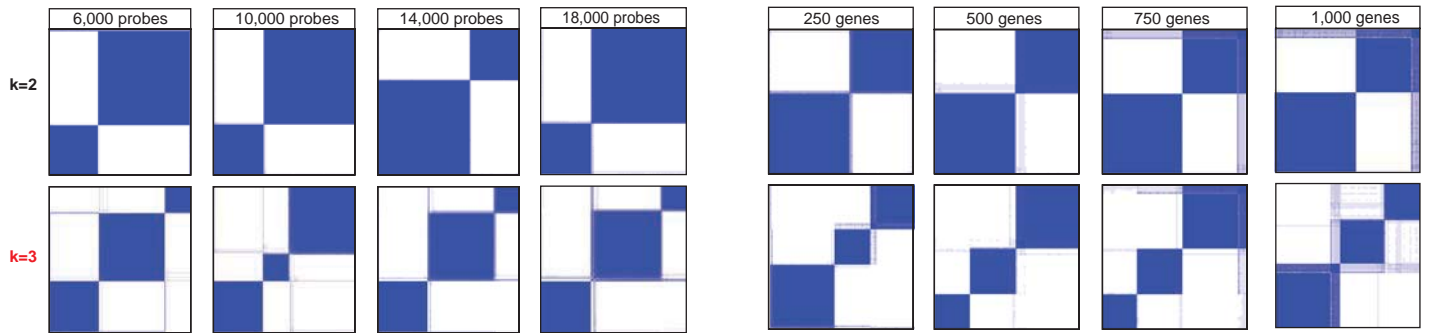
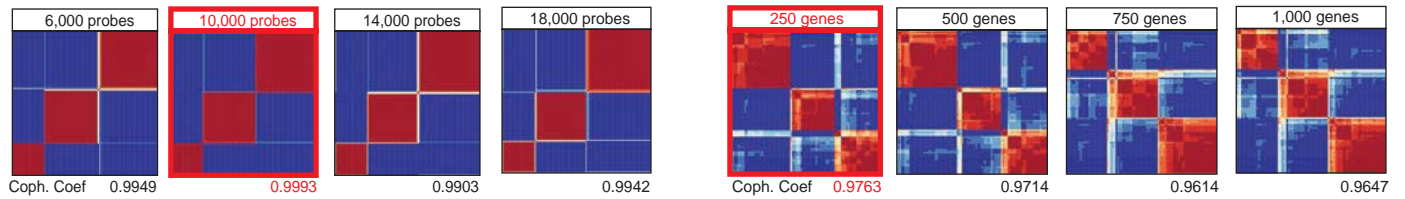
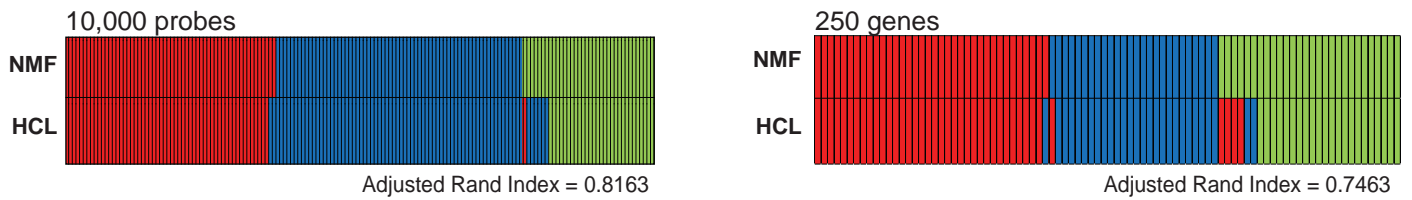
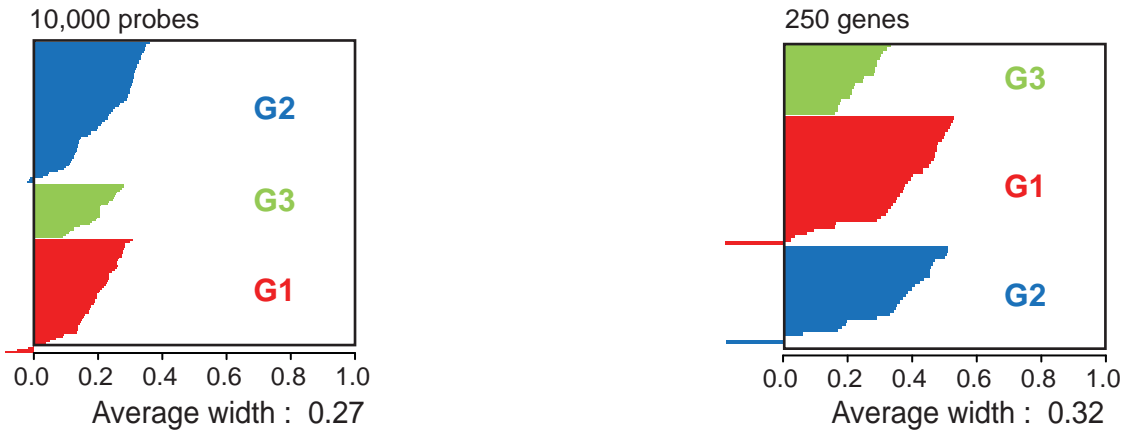
A**B****C****D****E**

Figure S2, related to Figure 2. Defining molecular classes of ATRT by global methylation and gene expression analyses

Multiple unsupervised consensus hierarchical cluster (HCL) analyses were performed on global methylation data generated from 162 primary ATRTs using the Illumina 450K BeadChip methylation arrays and 90 primary ATRTs using the Illumina HT12 Gene expression microarray. In order to discover molecular classes of ATRTs, an initial set of 30,000-6,000 probes and 2,000-250 genes with the highest standard deviation was re-iteratively analysed to determine the most stable tumor group clusters achievable with a minimal probe set.

(A) CDF plots of multiple unsupervised HCL cluster analyses performed on methylation data using 6,000 – 14,000 probes and 250 – 2,000 genes ranked by standard deviation to establish the most robust number of k classes, which was determined to be k=2 or 3 classes.

(B) Consensus HCL matrices for the individual probe sets for k=2 and k=3 classes. Dark blue indicates samples which remain stable within each cluster over 1000 iterations after 80% resampling. Lighter blue indicates samples which distribute between multiple groups. K=3 (red) was selected as the optimal number of k-classes.

(C) NMF consensus clustering was performed for k=3 using each probe set to establish the most robust subgrouping. Consensus matrices for each probe set determined that 10,000 probes and 250 genes gave the highest co-phenetic coefficient.

(D) Cluster assignments for consensus NMF and HCL are shown with an Adjusted Rand index of 0.8163 (methylation) and 0.7453 (gene expression) indicating a high agreement between orthogonal methods.

(E) Silhouette analysis for 10,000 probes and 250 genes identified five methylation and two gene expression samples with a silhouette width below 0, which were removed from further statistical analyses.

Table S6, related to Figure 2. Provided as a separate Excel file. Summary of genomic analyses and clinical information of ATRT subgroups

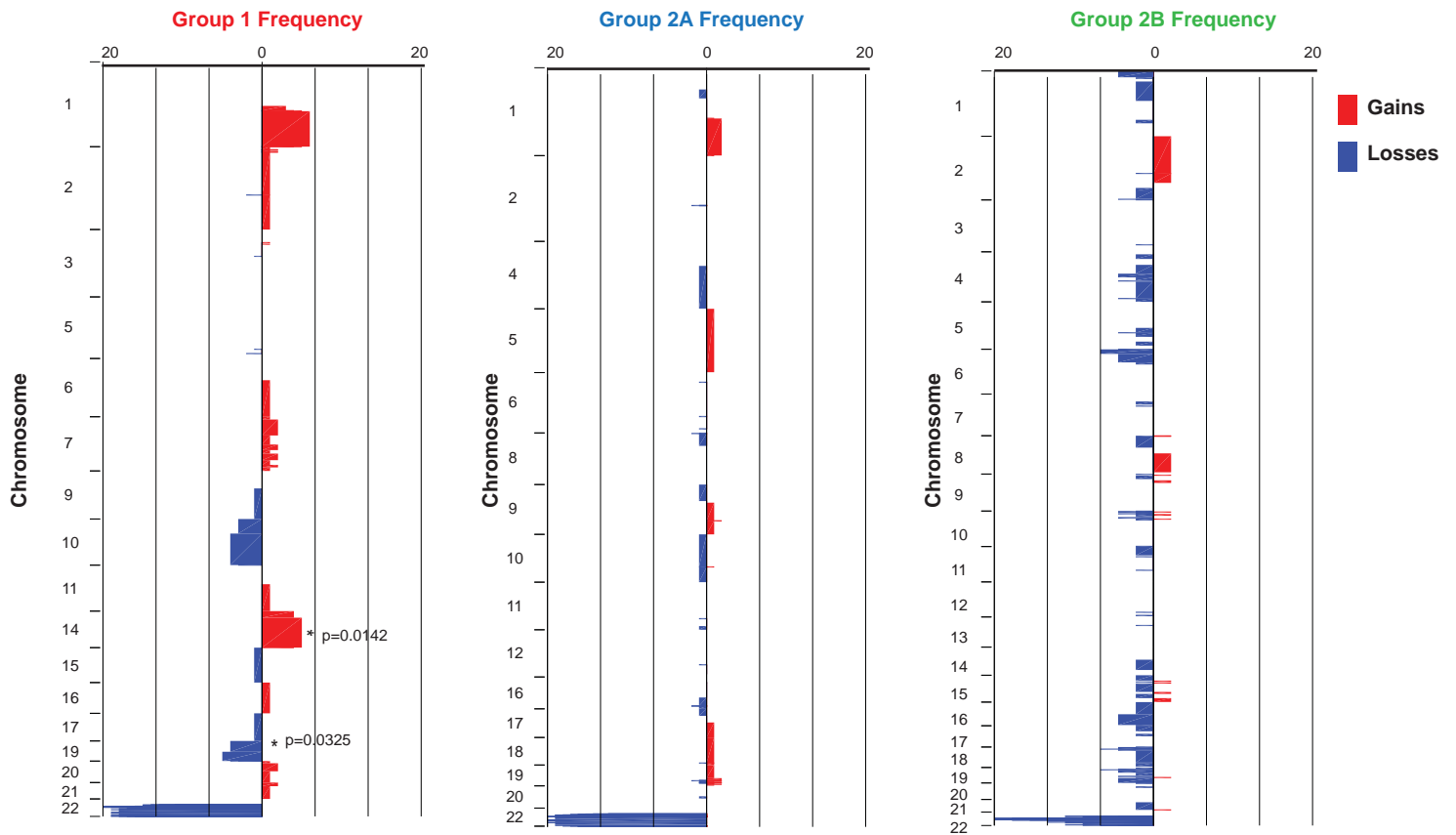
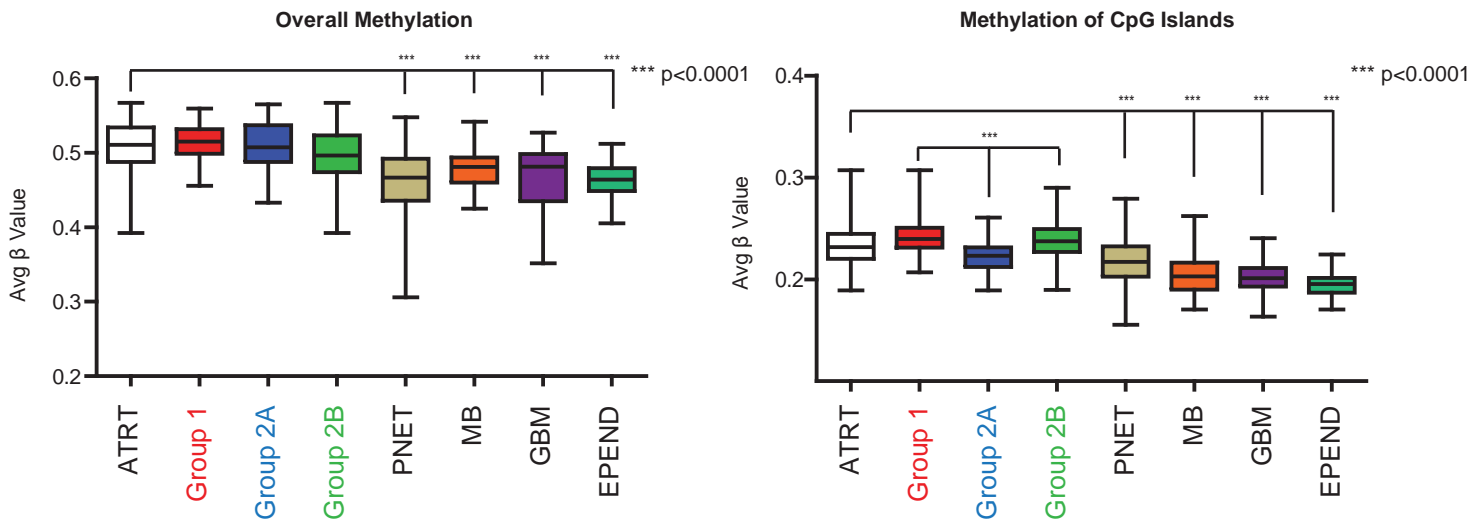
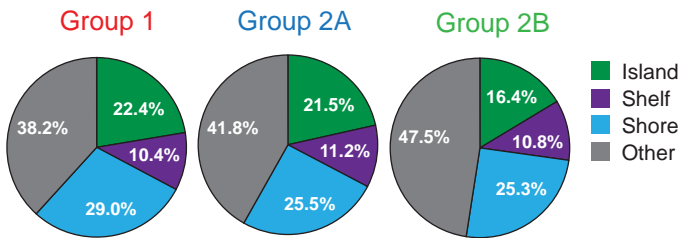


Figure S3, related to Figure 2. Global copy number features of ATRT subgroups

CGH plot of copy number events (red; gain, blue; loss) for each ATRT subgroup is shown. Y-axis depicts the frequency of events over each chromosome on the X-axis. Chromosome 14 gain and chromosome 19 loss enriched in group 1 ATRTs are indicated.

A**B**

Regions of differential methylation relative to CpG Island



Regions of differential methylation relative to gene features

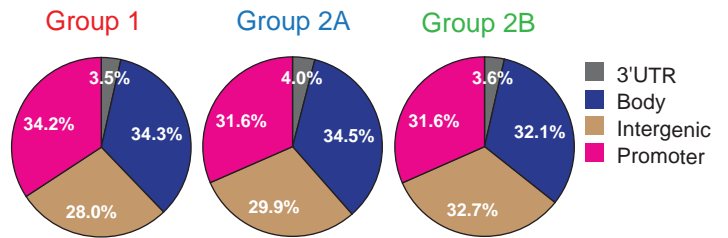


Figure S4, related to Figure 3. Global methylation features of ATRT subgroups

(A) Global (left panel) and CpG island (right panel) methylation levels in ATRT subgroups are shown relative to that in other pediatric brain tumors (PNET; primitive neuro-ectodermal tumor, MB; medulloblastoma, GBM; glioblastoma, and EPEND; ependymoma).

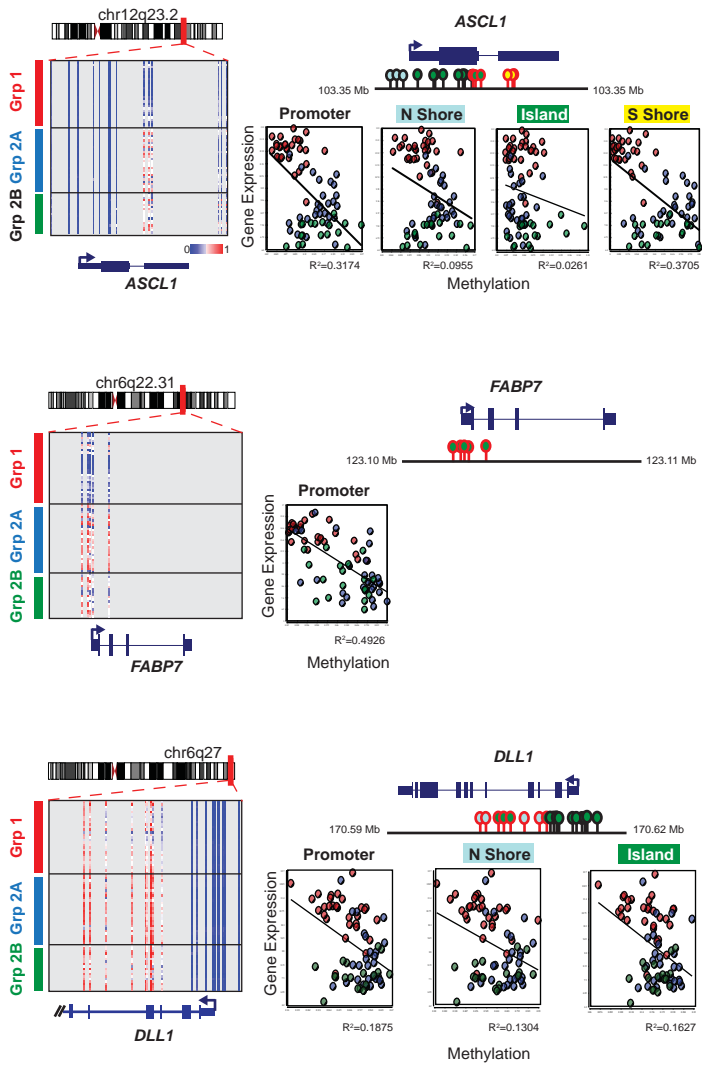
Methylation levels are represented as β -values and are normalized using BMIQ method (see supplemental experimental procedures).

Boxplot middle represents mean, box boundaries represent 1st and 3rd quartiles and whiskers represent 10th and 90th percentiles.

(B) Proportion and location of differentially methylated probes in ATRT subgroups.

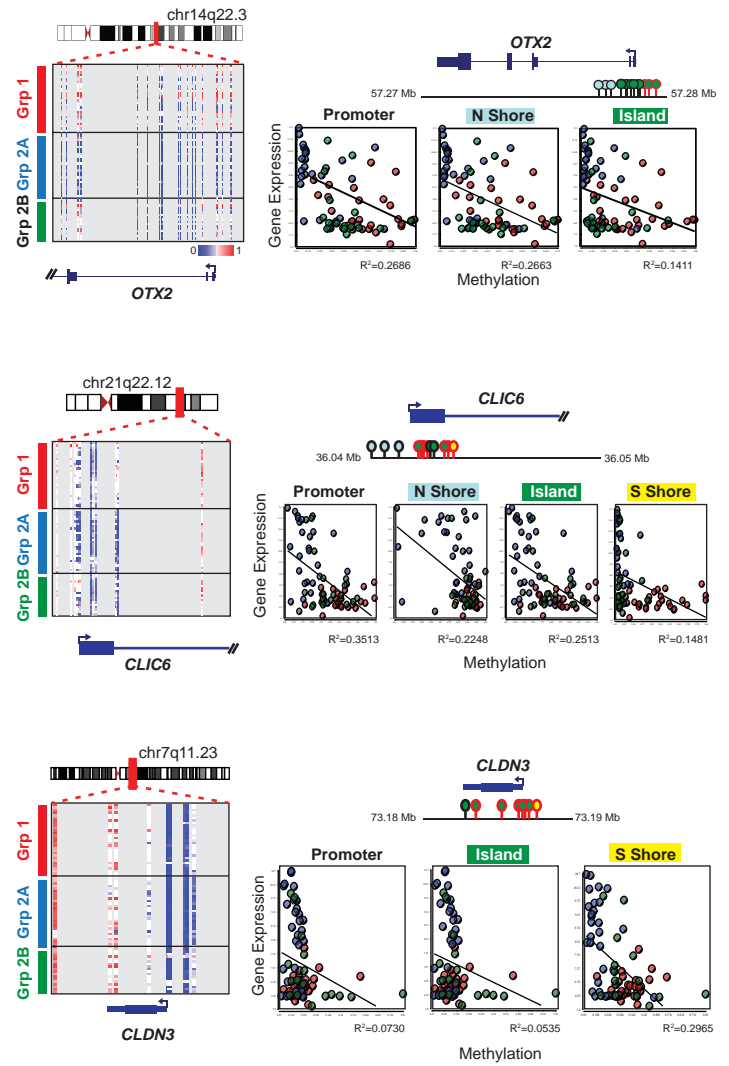
A

Methylation at Group 1 Specific Loci



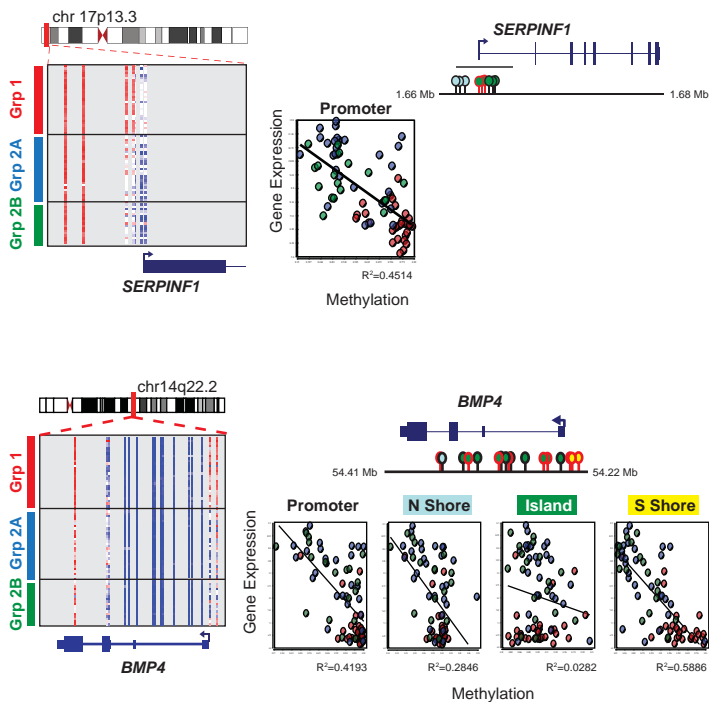
B

Methylation at Group 2 Specific Loci



C

Methylation at Group 2A Specific Loci



D

Methylation at Group 2B Specific Loci

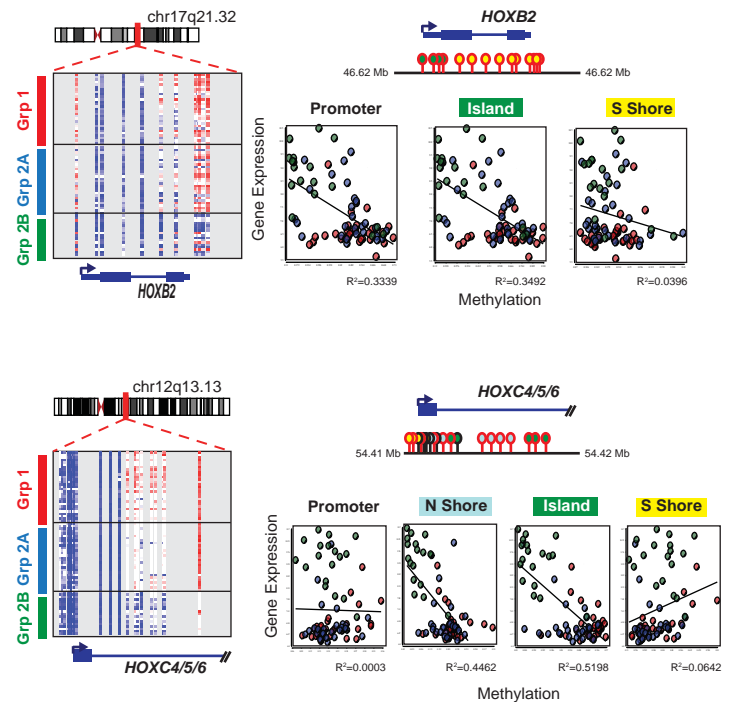
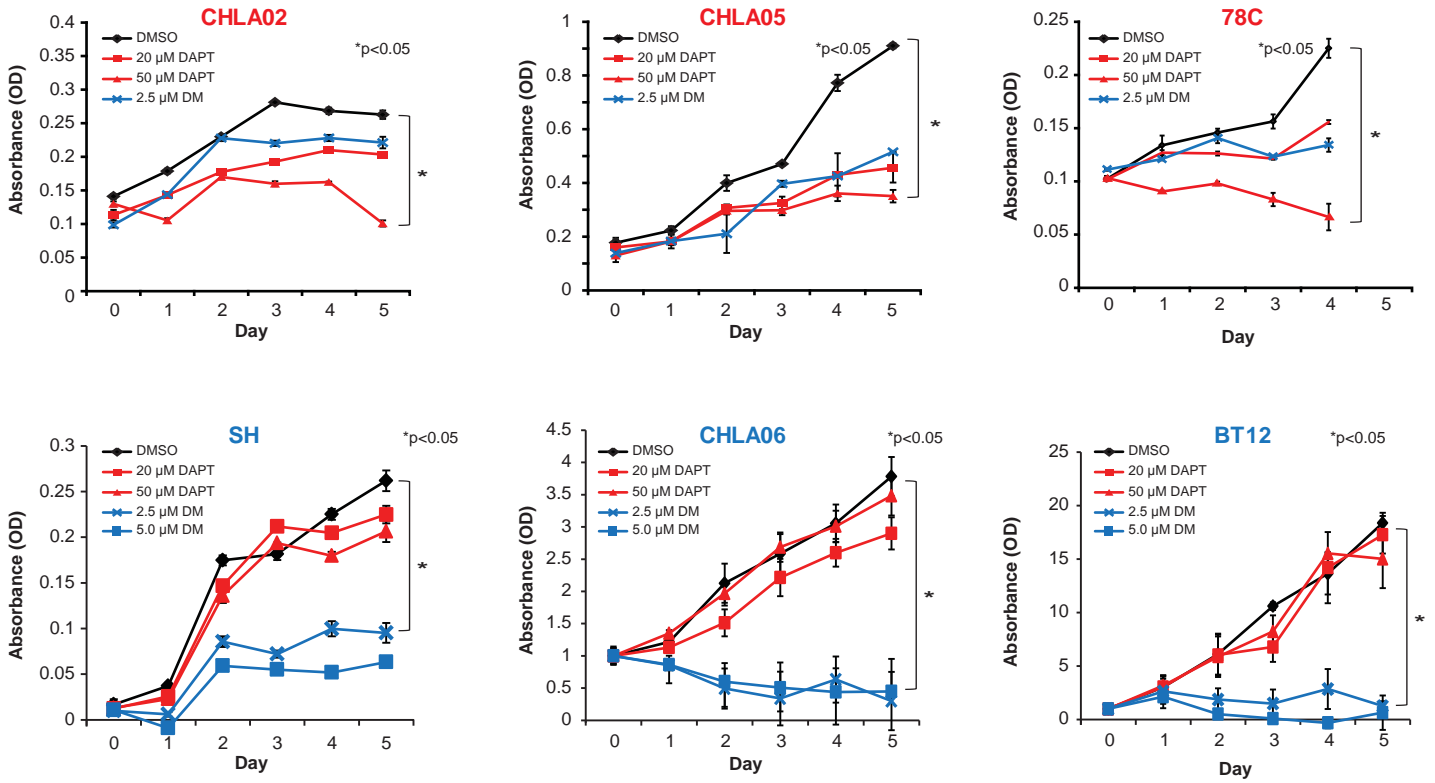


Figure S5, related to Figure 3. Methylation patterns at representative gene promoters in ATRT subgroups (A-D). Heatmap of probe methylation levels in promoter regions of representative group 1 (*ASCL1*, *FABP7*, *DLL1*), group 2 (*SERPINF1*, *BMP4*), group 2A (*OTX2*, *CLIC6*, *CLDN3*), and group 2B (*HOXB2*, *HOXC4/5/6*) enriched loci with corresponding scatter plot of \log_2 gene expression and β value methylation score. Average methylation levels of probes at the promoter +/- 2.5 kb from TSS (encompassing north/south shore and CpG islands) are plotted against gene expression levels for each individual tumor; a corresponding regression line and Pearson's correlation value (R^2) are indicated. Group 1, 2A, and 2B tumors are respectively shown as red, blue or green circles. Schema show locations of TSS and methylation probes (blue = North/N. shore, green = Island, and yellow = South/S. shore) in individual loci; probes most significantly correlated with gene expression activity are highlighted in red.

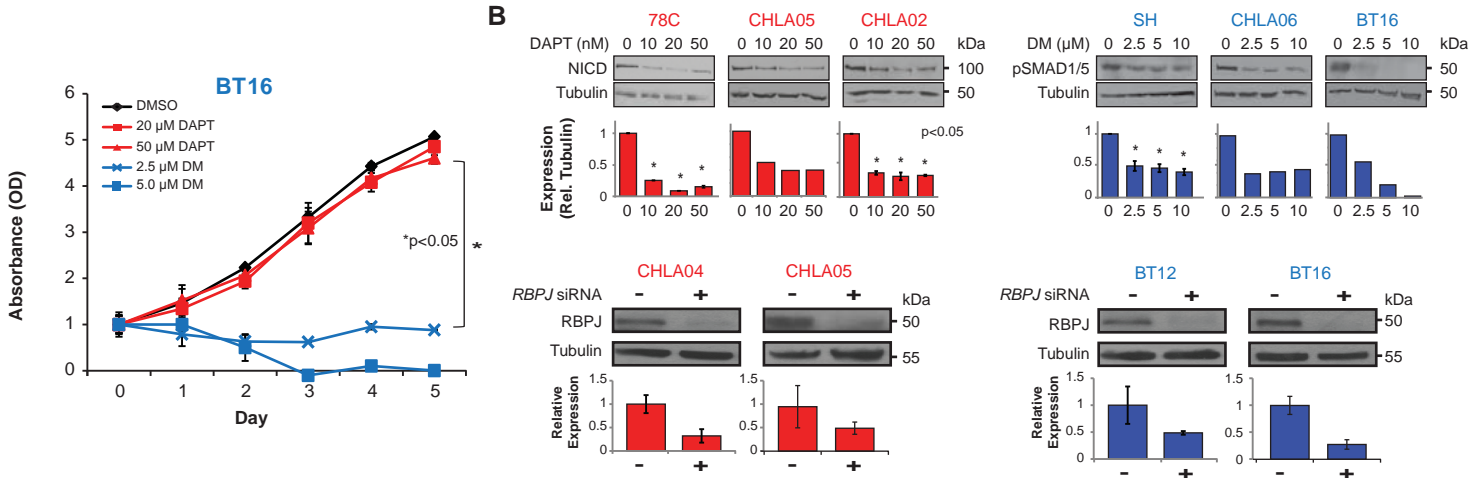
Table S7, related to Figure 3. Provided as a separate Excel file. Ingenuity Pathway Analyses (IPA)

Table S8, related to Figure 4. Provided as a separate Excel file. Differentially open chromatin peaks

A



B



C

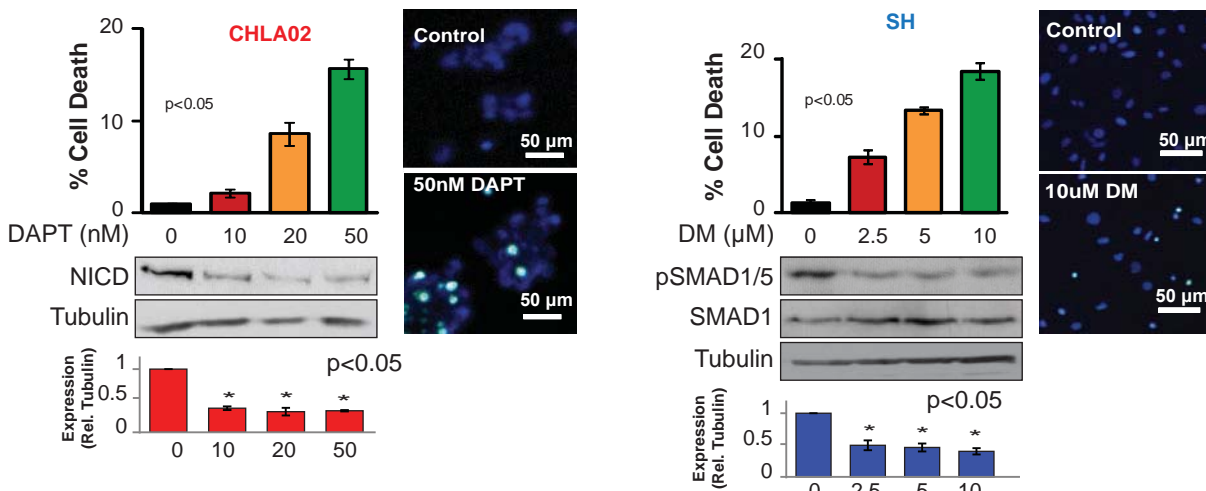


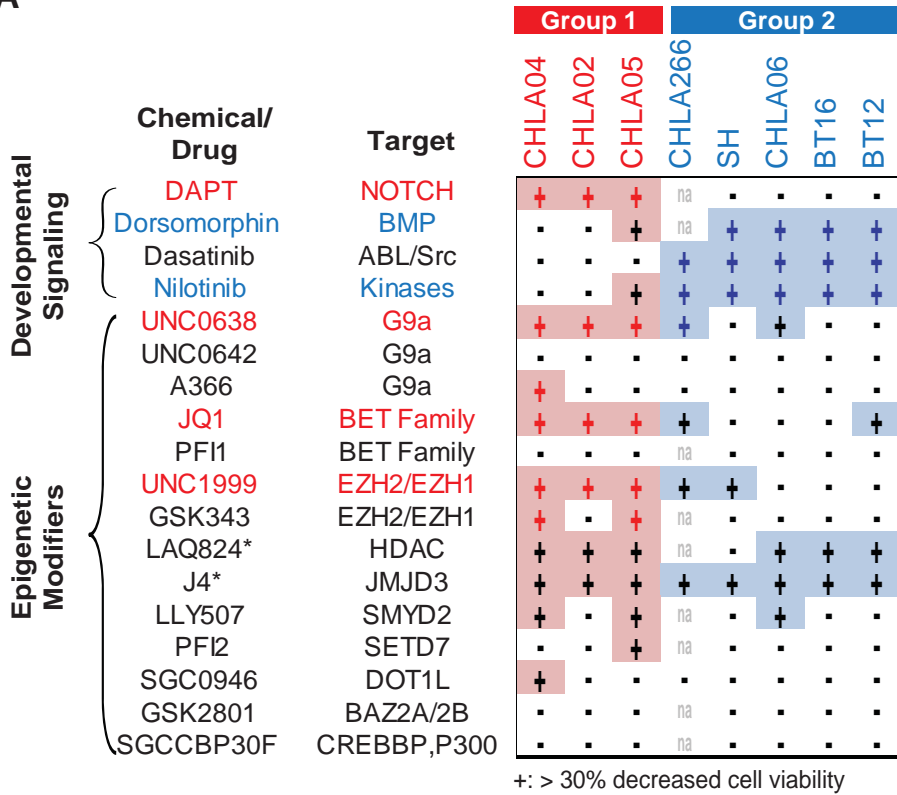
Figure S6, related to Figure 5. Treatment of Group 1 and 2 cell lines with DAPT and DM

(A) MTS cell viability assays for group 1 (CHLA02, CHLA05, 78C) and 2 (SH, CHLA06, BT12, BT16) ATRT cell lines treated with γ -secretase inhibitor DAPT and BMP pathway inhibitor Dorsomorphin (DM) for 5 days. Differences in cell viability were assessed using the Student's independent *t* test.

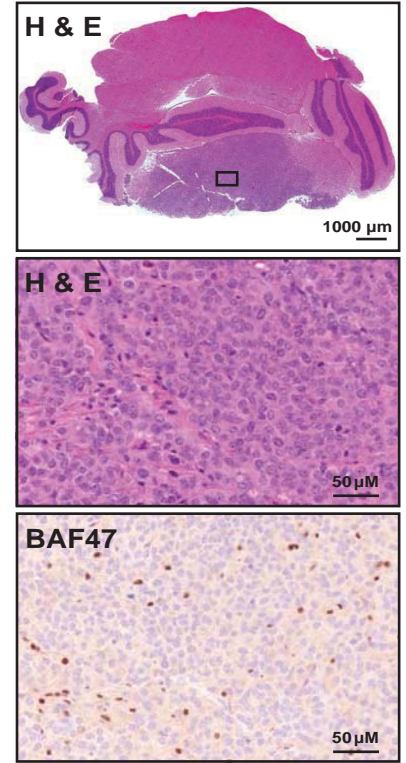
(B) Densitometry scans for **Figure 5C**.

(C) TUNEL assay shows DAPT and DM induced apoptosis respectively in group 1 (CHLA02) and 2 (SH) ATRT cell lines. Western blot of NICD and pSMAD1/5 confirming DAPT and DM induced apoptosis respectively via NOTCH and BMP signaling with corresponding densitometric analyses. Error bars depict \pm SEM (n=3).

A



C



B

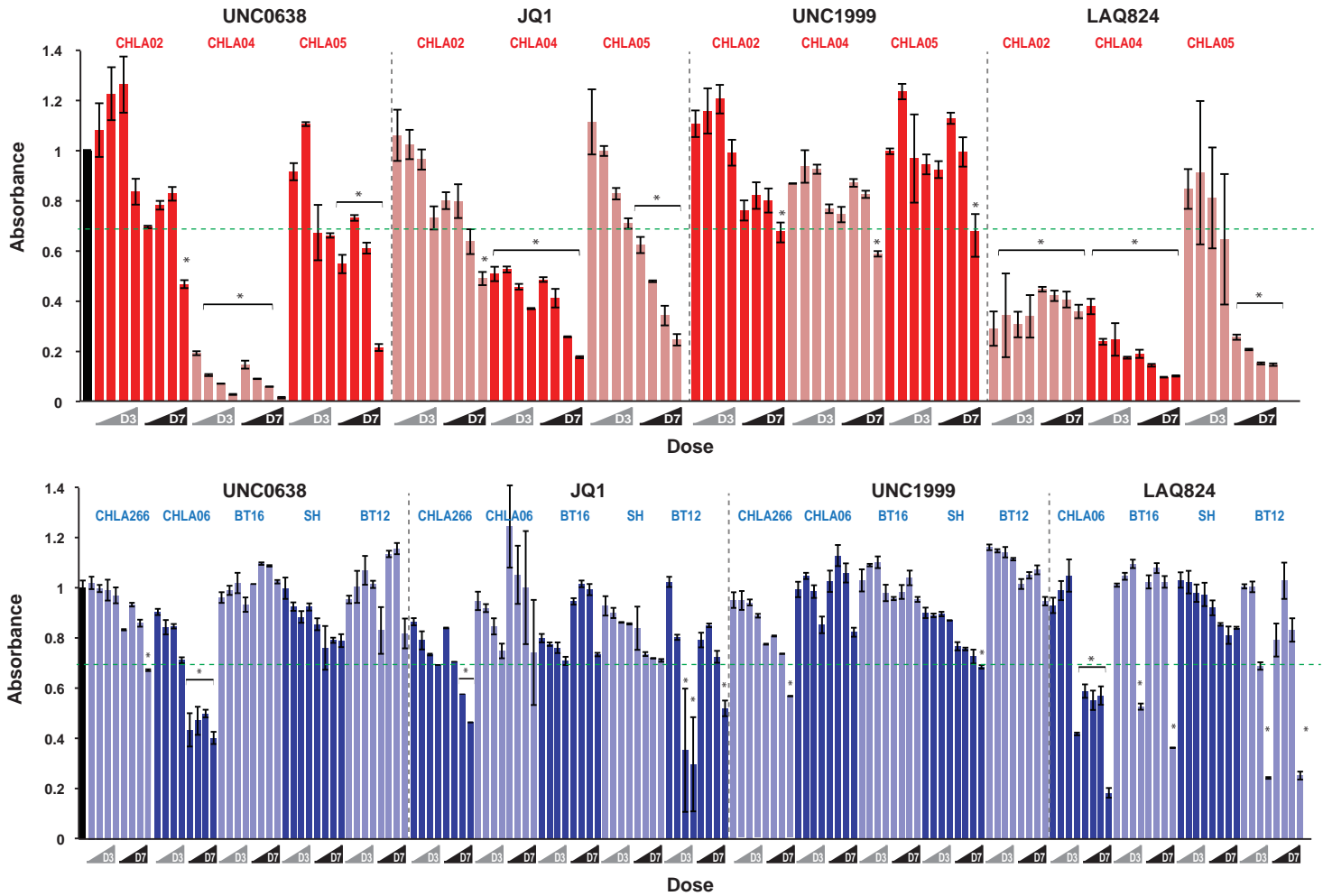


Figure S7, related to Figure 6. Summary of screen for ATRT subgroup-specific therapeutic targets

(A) MTS cell viability assays were performed on group 1 (CHLA02, CHLA04, CHLA05) and group 2 (CHLA266, CHLA06, BT16, SH, BT12) ATRT cell lines after treatment with various small molecule inhibitors. For each drug and each cell line, 4 concentrations (0.1, 0.25, 0.5, 1.0 μ M [SGC946, JQ1, UNC642, PFI1, A366, UNC638], 0.5, 1.0, 2.5, 5.0 μ M [GSK2801, GSK343, SGCCBP30F, UNC1999, LAQ824, PFI2], 0.1, 0.5, 1.0, 2.0 μ M [LLY507], 0.5, 2.5, 5.0, 10.0 μ M [J4]) of inhibitor were tested and MTS absorbance readings were taken at day 3 and 7 post treatment. Drugs/chemical probes which resulted in $>30\%$ reduction in cell viability (+/- indicates $>$ or $<$ 30% reduction in cell viability) was considered active in specific cell lines. Drugs/chemical probes with significant growth inhibitory activity in group1 and 2 ATRT cells lines are shown respectively in red and blue. Drugs active in both ATRT subgroups are shown in bold. na: failed due to lack of growth, *: universally toxic at low concentrations.

(B) Bar plot summary of MTS assays for a subset of drug/chemical probes with robust and consistent subgroup-specific effects on ATRT cell viability. Green dashed line indicates threshold of $\geq 30\%$ reduction in cell viability, * = $p < 0.05$ reduction in cell viability relative to DMSO-treated controls. Data for probes with inconsistent subgroup-specific therapeutic activity is not shown. Error bars depict \pm SD (n=3)

(C) Representative images of BT16 orthotopic xenografts in NSG mice. Images depict H&E immunohistochemical staining of gross brain (top panel) and cellular morphology (middle panel), in addition to BAF47 immunohistochemical staining (bottom panel).

Figure S8, related to Figure 7 and 8. Schema of *PDGFRB* locus

(A) UCSC gene tracks are shown for *PDGFRB* locus (chr5:149,479,360-149,545,365; outlined in red) relative to *CSF1R*. Tracks shown (top to bottom) include RefSeq gene annotation, Illumina 450k probe addresses and regulation tracks from the ENCODE project including DNase hypersensitivity sites, H3K27ac, H3K27me1, H3K27me3, and various transcription factor binding indicated by ENCODE ChIP-seq data. Highlighted orange, blue, and pink lines respectively depict the predicted enhancer domain, *PDGFRB* gene body and *PDGFRB* promoter. Arrows indicate predicted DNA:DNA interactions and a putative chromatin loop (see **Figure 8B**). Illumina 450k probes significantly hypomethylated in group 2A/B versus group 1 primary ATRTs are shown in red.

(B). Gene expression heatmap of transcription factor expression in 90 primary ATRTs. TFs with predicted binding to the *PDGFRB* promoter/enhancer region including *MYC* (blue) and *FOS* (green) which are upregulated in group 2 ATRTs and have known functions in *PDGFRB* transcription are shown in bold. Fold change (Group 1 vs. 2) and FDR corrected p values were calculated using a supervised Student's *t* test.; $p < 0.05$ was considered significant.

SUPPLEMENTAL EXPERIMENTAL PROCEDURES

Next Generation DNA and RNA Sequencing

Whole genome/exome and RNA sequencing were performed respectively at Genome Quebec Innovation Centre, Montreal, Quebec and at The Centre for Applied Genomics, Toronto, Ontario. For DNA library preparation, 2-3 μg of high molecular weight genomic DNA (gDNA) were fragmented using a Covaris E210 and prepared using the TruSeq DNA Sample Prep Kit (v1 FC-121-1001, FC-121-1002, Illumina Inc, San Diego, CA) as per the manufacturer's specifications with modification for size selection of fragments (between 450-550 bp for whole genome shotgun or 350-4,500 bp for whole exome) performed on a 1.5% gel Pippin Prep cassette (Sage Science, Beverly, MA). For exome preparation we followed the standard manufacturer procedures using the IlluminaTruSeq exome enrichment kit. RNA preparation was performed using the IlluminaTruSeq RNA sample preparation kit for poly-adenylated mRNA selection, or using Illumina RiboZero Stranded library preparation kit for total RNA sequencing.

WES/WGS sequence alignment and variant calling

We generated a total of 69.95 billion reads for whole genome sequencing of 23 matched normal lymphocyte/tumor samples, respectively (average of 3.04 billion reads per subgroup tumor/normal pair) using the IlluminaHiSeq 2000 platform with a mean sequencing coverage of 47.76x and 37.66x respectively for tumor DNA and normal lymphocyte (**Table S1**). Fifteen tumor/normal pairs were sequenced using paired-end 100 bp length reads, and 8 pairs were sequenced using 125 bp reads. For whole exome sequencing, a total of 66.02 billion reads were generated for 27 samples, 5 had matched normal lymphocyte DNA, and were sequenced to a mean CCDS coverage of 66.86 (**Table S1**). Illumina sequence adapters were removed and reads were trimmed from the 3' end to have a phred score of ≥ 30 using Fastx software (v0.0.13.1). Reads were aligned to hg19 (NCBI build 37, August, 2012) reference genome using BWA aligner (v0.6.2). Local re-alignments were performed using GATK (v2.1-9g6149b06) to reduce false positive rates across putative indels where mismatch bases are preferred over indel calls during alignment and 5' PCR-duplicated reads were marked using Picard software. Somatic SNV and small indel calling was performed using SAMtools mpileup and bcftools varfilter (v0.1.18) with default parameters and the bcftools -T pair option enabled to compute a phred-scaled likelihood ratio (CLR score) to score somatic variants. Low-quality variants were filtered using a minimum depth coverage of 2, maximum coverage of 1200 and a minimum RMS mapping quality of 15.

Detection of somatic structural variation (SV) from next generation sequencing data

We employed four orthogonal SV detection algorithms – CREST (Wang et al., 2011), BreakDancer (Chen et al., 2009), and Pindel (Ye et al., 2009), and the trans-ABYSS pipeline (Robertson et al., 2010) on whole genome sequencing data from $n=23$ matched tumor/lymphocyte DNA. CREST was run with default parameters using germline subtraction of soft-clipped reads option to select for somatic variants. We required dual-sided soft-clipped reads with one side having at least 3 supporting reads and retained SV's affecting genetic loci defined in RefSeq (hg19, Build 37, August 19, 2012). We visualized all inversions, translocations and large insertions/deletions at the alignment level using IGV and examined by a post-filtering assembly process. CREST was also run on WES samples ($n=27$ tumors, 5 with matched lymphocyte DNA) and filtered as previously. Discordant reads were extracted from the BAM files and assembled using the Velvet algorithm (Zerbino and Birney, 2008) within Geneious Software Suite (v5.6.5). Assemblies provided a contig spanning the predicted breakpoints of structural events which were re-aligned to the reference sequence using BLAT. A structural event was considered pre-validated if the contig unambiguously mapped to the two breakpoint regions. Events were compared to the Database for Genomic Variants (v10) to exclude normal population SVs. Orthogonal tools BreakDancer and Pindel were used in parallel. BreakDancer was run with the following parameters: (1) minimum mapping quality 35, (2) read-pairs within +/- 3 standard deviations of insert size for tumor and +/- 2 standard deviations for normal were excluded. Pindel was run according to the following parameters: (1) minimum match around breakpoint 10 bp, (2) minimum match to reference 50 bp, (3) minimum read mismatch rate 0.1. For both tools, somatic events were selected by requiring read call support of ≥ 10 reads in the tumor with 0 supporting reads in the normal. Hyper- and hypomappability regions and microsatellite regions were also discarded. Finally, the trans-ABYSS pipeline (v1.4.8) was performed according to previous publications (Cancer Genome Atlas Research, 2013) (Morin et al., 2013). Briefly, *de novo* assembly of sequencing reads across multiple k-mer values was performed and merged into a non-redundant set of contigs. Assembled contigs were aligned using BLAT to human reference genome hg19, and discordant alignments not matching known gene annotations (RefSeq, UCSC) were identified as putative gene rearrangements. Further filtering of candidates was conducted by mapping reads back to contigs using Bowtie

(v1.0.1), and to the genome using BWA (v0.7.8), and putative fusions are maintained by requiring at least 2 reads spanning contig breakpoints and at least 4 flanking paired-end supporting reads. Somatic events are selected by comparison of tumor calls to normal lymphocyte DNA. Detection of CNVs from WGS data was performed using a Hidden Markov Model (HMM) approach, which compares tumor to normal lymphocyte using HMMcopy (v0.0.6) (Ha et al., 2012). We also employed APOLLOH (v0.1.1) (Ha et al., 2012), which compares high confidence SNP allelic ratios between tumor and normal DNA for detection of loss of heterozygosity. All putative structural events are then filtered using the database for genomic variation (July 2013) to exclude normal variants in the healthy population, and then subjected to visual inspection of alignments using the Integrated Genomics Viewer (IGV).

Alignment and processing of RNA-sequencing data

We generated an average of 97.64 million reads/sample and aligned reads using the Tophat algorithm (n=5 tumors, n=1 normal). Adapter sequences were trimmed using Trim Galore (v0.2.5) and aligned using TopHat (v2.0.5), with an average of 92.13 million reads aligned per sample (**Table S1**). We used the hg19 reference genome and the UCSC gene annotation file for alignment to known genes. Tophat was run with the fusion search function enabled for detection of potential fusions using the following parameters: segment length=50, mate-std-dev=80, fusion-anchor-length=13, fusion-multipairs=4, fusion-min-dist=100000. Candidate fusions were manually curated to include only fusions with at least 10 spanning reads or 5 read pairs and annotated according to hg19 RefFlat (August 19th, 2012) using custom scripts based on BEDtools. For samples prepared using the RiboZero protocol, we enabled the fr-firststrand library-type option to allow for strand-specific alignments. Putative events were inspected at the alignment level using IGV and further corroborated by extraction of discordant reads, Velvet assembly and re-alignment using BLAT. Gene expression values were represented as FPKM values generated from RNA-seq alignments using cuffquant and cuffnorm programs within the Cufflinks RNA-seq assembly suit (v2.2.1) (Trapnell et al., 2012) with geometric library normalization and blind replicate dispersion estimation.

ATAC-seq Sample Preparation and Bioinformatics Analysis

Snap-frozen ATRT primary tissue or freshly cultured cell lines were prepared for ATAC-seq according to previously published methods with minor modifications (Buenrostro et al., 2013). Briefly, nuclei were prepared from ~50,000 cells by spinning at 600 x g for 10 min, followed by a wash using 50 µl PBS buffer, and further centrifugation at 600 x g for 5 min. Cells were lysed using cold lysis buffer (10 mM Tris -HCl, pH 7.4, 10 mM NaCl, 3 mM MgCl₂, 0.1%), and subsequently centrifuged for 10 min at 600 x g at 4°C. The supernatant was removed and pellet resuspended in 50 µl of transposase mix (25 µl of 2xTD Buffer, 2.5 µl of transposase [TD enzyme; Illumina], 22.5 µl of water) for 30 min at 37°C. Next, library amplification was performed using the NEBnext High Fidelity 2xPCR Master Mix (NEB#M0541S) according to previously published PCR conditions (Buenrostro et al., 2013). PCR reactions were purified using QIAGEN miniElute kit, and a following size selection step was performed using LabChip (#760601). ATAC-seq library preparations were sequenced using single-end 50 bp reads on the Illumina HiSeq 2000 platform. Raw reads were adapter-trimmed using Trim Galore (v0.2.5) and aligned to the genome with Bowtie (v1.0.1) with the m1 option enabled to allow for only uniquely aligned high-quality reads. Peaks were called using the MACS2 software (v2.1.0.20140616) (Zhang et al., 2008) with the options -q 0.05 to retain significant peaks, -shiftsize 50 to account for the transposase fingerprint, and otherwise default parameters were used. Tag count libraries and bedgraph files were constructed using HOMER software (v4.7) (Heinz et al., 2010). Correlation and PCA analyses were performed using the DiffBind software (v1.16.2) (Ross-Innes et al., 2012).

Cross-Cell type Correlation (C3D) analysis

We performed a Cross-Cell type Correlation of DNaseI hypersensitivity signal (C3D) analysis to predict interactions between open chromatin regions. This approach is based on a similar method described by Thurman *et al.* and the Pearson correlation coefficient between open regions was similarly calculated in a pairwise manner across the open chromatin signal from 79 ENCODE cell lines. Our analysis additionally used sample-specific mapping of the DNaseI signal intensities from the ENCODE samples to open regions identified by ATAC-seq in each of ATRT T13, T4, T26, T27, and T45, and restricted to a 500 kb window around the *PDGFRB* promoter. All correlations were tested for statistical significance and adjusted for multiple testing (FDR) within the 500 kb window. The correlation matrices were generated using the corrplot R package [Taiyun Wei (2013). corrplot: Visualization of a correlation matrix. R package version 0.73. <http://CRAN.R-project.org/package=corrplot>]

H3K27ac ChIP-seq Sample Preparation and Bioinformatics Analysis

Formaldehyde cross-linked chromatin from 5x10⁶ CHLA04, CHLA05, and BT12 cells were fragmented via water

bath sonication (20-40 cycles, max amplitude, 30 second intervals) to an approximate fragment length of 200-400 bp. After centrifugation of fragmented chromatin, the supernatant was incubated with H3K27ac antibody (Abcam Cat# ab4729) (preincubated for 6 hours with Dynabeads A and G [Invitrogen Cat# 10002D, 10004D]) overnight at 4°C. Antibody-free input was retained as a control. After incubation, chromatin was decrosslinked using decrosslinking buffer (1% SDS and 0.1M NaHCO₃) and DNA was purified using QIAGEN QIAquick PCR purification kit (Cat # 28104), and further quantified using PICO green. Sequencing was performed similarly as ATAC-seq using single-end 50 bp reads on the Illumina HiSeq 2000 platform. Alignment and peak calling was performed as above with the exception of removing the `-shiftsize=50` parameter used for ATAC-seq.

Chromatin conformation capture analysis

Chromatin conformation capture (3C) was performed on BT16 and CHL05 cells. The 3C library preparation followed two previously published reports (Hagege et al., 2007) (Zhang et al., 2012) with modifications suggested by Court et al 2011 (Court et al., 2011). Briefly, ~ 8 million cells were prepared for chromatin cross-linking with 1% formaldehyde for 10 min at room temperature with rocking. The reaction was quenched with glycine. Following washing and incubation with permeabilization buffer, the nuclei of the cells were digested with Hind III by adding serially 150 units (U) of restriction enzyme for a total of 450 U. 150 U of Hind III-HF was added and incubated at 37°C for 2h shaking at 900 rpm, then added gently for a second time more 150 U of Hind III and incubate at 37°C for 2h shaking at 900 rpm, then add again 150 U of HindIII for an overnight digestion at 37°C shaking at 900 rpm. To inactivate restriction enzyme, SDS (final 1.6%) was added and incubated for 30 min at 37°C. The cross-linked and digested DNA was ligated at low DNA concentration (T4 ligase 4000 units, 4 hr at 16 C and then 30 min at room temperature). Cross-linking was reversed by incubation at 65°C for 16 hr in the presence of Proteinase K (40 µg/ml) followed by phenol/chloroform/ethanol DNA clean up.

3C interaction products were detected by qPCR using SYBR green with candidate primer pairs (anchor and bait/controls) following an adapted previously published report. The reaction for detecting 3C interaction was performed using KAPA Sybr Fast qPCR Master Mix, 175 nM of the anchor forward primer and bait/controls reverse primers (final concentration) and 20 ng of 3C libraries (adjusted after quantification). Samples were tested in triplicate for amplification detection. The PCR conditions were 95 °C for 3 min followed by 40 cycles of 5 s at 95 °C, annealing and extension 30 s at 64 °C. The qPCR results from 3C-processed sample were normalized to serial dilutions (standard curve) of 3C-positive control template on each plate. The positive control was generated by synthesis of all possible PCR products using the available primers, followed by gel extraction and purification. PCR products were mixed in equimolar concentrations, digested with Hind III and purified by phenol/chloroform extraction and ethanol-acetate precipitation. The digested fragments underwent random ligation (T4 ligase) at high DNA concentration and purified with MiniElute PCR. To mimic 3C sample condition, the concentration of control template was adjusted by addition of genomic DNA that had undergone digestion and random ligation to the control template, increasing the complexity of the control. This way the PCR efficiency was not affected by the total amount of the DNA present (only target regions in the control template). We used a published normalization method for data analysis (Hagege et al., 2007). The final value was calculated using $\text{value} = 10^{-(\text{Ct}-b)/a}$ (b: intercept and a: slope). These values were normalized to an internal control (GAPDH).

Primers for Chromatin Confirmation Capture

Fragment	Forward Primer (5'-3')	Reverse Primer (5'-3')
Anchor	TCTGGGCAGTGACAAAACCATAACC	AGACCACGGGACCTCTTTCACT
FR1	CCCTGCAGTTTTCTTGCCTCCTA	CTACCCTGCCCTGCCTGAAG
FR 2	CCCACCACAAAGCACTGTCATG	TGATCGTTGTAAACAGTGGCCTTT
FR3	GTTGGAACCACAGGACTGGAAT	ATGGAGAACCTGTGATTCTACTGAA
FR4	GGGGAAGCAGGCTCAGAGAGAT	GCAGAGAGAGGATGGAGCTTGT
FR5	GGACAGACAGGACAGTGCAAGA	GCTCAGAGAGGGTCAGGACTGT
Bait/promoter	AGTCCTCAGAACAATCCCATGACA	GGAGCCTGTCTGCCCAGTATTA
FR6	CTGGGTGGATGGGAGTTCTTGT	CCACTGACCACCTCTCCAATCT (w/R)
FR7	CTGGGTGGATGGGAGTTCTTGT (w/F)	CCACTGACCACCTCTCCAATCT
FR8	AAGGGAGATTATGCAGTGGTTTGT	TGGAACACAGGAGCAGGAAACA
FR9	TGCCAGGACAGAGAGGAGTAATT	AAACTCCCGTCCCCTAATGCAT
FR10	CACAGGGCATGGTAGACGTACT	CCCAGCCCTGCCTTCACTTG (w/R)
FR11	CACAGGGCATGGTAGACGTACT (w/F)	CCCAGCCCTGCCTTCACTTG
GAPDH	CCACTCCTCCACCTTTGAC	ACCCTGTTGCTGTAGCCA

Copy number analysis

OmniQuad SNP array analyses were performed on 60 primary and 2 recurrent ATRTs. Probe fluorescence intensity normalization was performed using Illumina's GenomeStudio (v. 2011.1, Genotyping Module 1.9.0) and represented as Log R ratio ($\text{Log}_2 [R_{\text{experiment}}/R_{\text{controlset}}]$) and B Allele Frequency (BAF) plots. SNP positions were based on the hg19 (Build 37, August, 2012) human reference genome. SNP data was analyzed using orthogonal tools: DNACopy, dChip, Partek, and ASCAT (Allele Specific Copy Number Analysis of Tumors). Normalized Log R ratios were imported into the R statistical language environment (v2.14) and analysed using the Circular Binary Segmentation (CBS) algorithm provided in the DNACopy R package (v1.32.0). Segments with < 10 markers were filtered out, and copy number regions were classified according to the following criteria: homozygous loss: $R \leq -0.5$, heterozygous loss: $-0.5 < R < -0.1$, balanced (2n): $|R| \leq 0.1$, gain: $0.1 < R < 0.2$, amplification: $R \geq 0.2$. Partek and dChip were also used to detect copy number variants. For Partek, genomic segmentation was performed using a 150-probe bin size and events with < 10 markers were discarded. For dChip, Log R Ratios were exported from Genome Studio and normalized using the MBEI algorithm. Available matched normal lymphocyte DNA samples from 11 ATRTs were used as a diploid reference, and resulting copy number estimates were compared against the human HapMap project and the Database of Genomic Variants to exclude normal population CNVs. Focal CNVs (less than 12 Mb) were annotated using the hg19 RefFlat with custom scripts to identify candidate targets that mapped within regions of CNV. Tumor purity and ploidy was assessed using ASCAT with default parameters.

Determination of somatic mutation rates across the ATRT genome

To define genomic somatic mutation rates, we visually validated a subset of 881 somatic mutations ($\text{CLR} \geq 35$) to establish the sensitivity and specificity of CLR score as a predictor of somatic status (CLR scores from 35-200 were tested). For each CLR score tested, sensitivity and specificity were calculated using the following formula: Specificity = $\text{TN}/(\text{TN} + \text{FP})$ and Sensitivity = $\text{TP}/(\text{TP} + \text{FN})$

TN = True negative; Non-somatic mutation with $\text{CLR}_{\text{mutation}} < \text{CLR}_{\text{tested}}$

FP = False positive; Non-somatic mutation with $\text{CLR}_{\text{mutation}} \geq \text{CLR}_{\text{tested}}$

TP = True positive; Somatic mutation with $\text{CLR}_{\text{mutation}} \geq \text{CLR}_{\text{tested}}$

FN = False negative; Somatic mutation with $\text{CLR}_{\text{mutation}} < \text{CLR}_{\text{tested}}$

We determined CLR= 68 provided a sensitivity and specificity of 89% for determining true somatic status of a mutation, and used this score to calculate the mutation rate for the 13 primary as well as 2 recurrent ATRTs with matched lymphocyte DNA in both the CCDS coding regions and in the whole genome. We included chromosomes 1-22, X and Y and mutations with an overall minimum depth of coverage of at least 10x. Mutations were

categorized into single nucleotide variations (SNVs) and small insertions/deletions (indels), and mutation rate was determined as the total number of mutations/total megabases covered (callable region) for the coding region and for the genome. Callable region was defined as the percentage of CCDS or genome coverage at a depth of 10x multiplied by the total length of the genome or coding region (**Table S1**). Mutations with CLR \geq 68 were also used to categorize nucleotide transitions and transversion profiles using custom scripts written in python.

Gene expression and methylation array data processing

For gene expression analysis (90 primary and 2 recurrent ATRTs), probes were collapsed into genes by taking the average value, quantile normalized using the Lumi R package (v. 2.11) and batch corrected using ComBat (Broad Institute) (Johnson et al., 2007). For methylation 450k analyses, only probes with a detection p value less than 0.01 and bead count > 3 were retained for analysis. Data (162 primary and 2 recurrent ATRTs) was normalized using BMIQ algorithm to obtain beta values for downstream analyses using the ChAMP package (v1.4.1) (Morris et al., 2014). All X and Y chromosomes probes (n=11,649), single-nucleotide polymorphisms (dbSNP, n=88,679), and unannotated probes (relative to hg19, n=65) were excluded leaving a total of 385,184 probes for methylation analyses.

Gene expression and DNA methylation analyses to define ATRT subgroups

We applied two orthogonal unsupervised consensus cluster methods to define the number of ATRT molecular subgroups using gene expression and methylation data. Gene expression and methylation data were independently examined using consensus unsupervised hierarchical clustering (Consensus Cluster Plus) (v1.20.0) (Wilkerson and Hayes, 2010) and Non-negative Matrix Factorization (NMF; Broad Institute) consensus cluster analyses. For these analyses, genes and methylation probes were ranked based on co-efficient of variation for gene expression or standard deviation for methylation data. For consensus HCL analyses, we performed re-iterative analyses of gene expression and methylation data sets using 200-2,000 genes or 6,000-30,000 methylation probes to reveal the optimal number of molecular classes over a range of 2-10 k classes. Consensus HCL analyses of gene expression and methylation data revealed ATRTs comprised three molecular subgroups. Next, to determine the optimal, most stable subgroup classification we performed NMF analyses using the same range of probe sets with k set to 3, to determine the number of probes with the highest cophenetic coefficient. In addition to strong agreement between orthogonal techniques, we also evaluated the concordance between gene expression and methylation tumor grouping using the Rand index to determine cluster agreement. Methylation and gene based clusters were most stable using probe sets of 10,000 and 250 probes or genes, respectively, and were used to assign tumor subgroup for downstream analyses. Silhouette analyses were performed using the optimal probe and gene sets to identify outlier samples. Samples with a negative silhouette width were excluded from further statistical analyses.

Pathway analyses of gene expression data

To define molecular and cellular features of the three ATRT subgroups, we conducted parallel and integrated analyses of gene expression and methylation data. Genes and probes enriched within tumor subgroups were respectively determined using a supervised t-test or Wilcoxon-Rank Sum test adjusted for multiple hypotheses testing using the Benjamini-Hochberg FDR method ($q \leq 0.05$) to identify genes and probes with respective +/- 2 fold or +/- 0.1 fold changes in expression or methylation levels between tumor subgroups. Magnitude of gene expression (\log_2) or methylation difference (beta values) and significance of change ($-\log_{10} q$ value) were visualized using volcano plots with a significance threshold of 1.3 $-\log_{10} q$ value ($q=0.05$) of one subgroup relative to the other two subgroups. To define enriched biological processes associated with tumor subgroups, Ingenuity Pathway Analysis (IPA) (<http://www.ingenuity.com/>) was performed using gene expression data +/- 2 fold with an FDR q value less than 0.05.

Prediction analyses of Microarray data (PAM) analysis

For determination of subgroups in ATRT cell lines we used PAM (Prediction Analysis of Microarray) analysis using the pamr package (Tibshirani et al., 2002) and adapted methods from Northcott *et al.* (Northcott et al., 2012). Briefly, genes for model training were selected based on the top differentially expressed genes from 90 primary ATRT samples of known subgroup identified using Student's *t* test adjusted using FDR method (described above). Using primary ATRT data as a training set, we trained a predictor model using the top 5-100 genes, and used this to predict the subgroup of ATRT cell lines. All class prediction analyses were performed in the R statistical programming environment (v3.0.2).

Validation of genomic alterations

For validation of SNVs and indels from next generation sequencing data, PCR primers were designed in-house and

applied to the Fluidigm Dynamic 48x48 array (<http://www.fluidigm.com/>). Primer pairs were multiplexed and PCR was performed according to manufacturer's instructions. PCR products were pooled and sequenced using IonTorrent or Illumina MiSEQ sequencing platform according to the manufacturer's instructions.

For structural variants, individual primers were designed in-house and Sanger sequencing was performed with Big Dye Terminator v3.1 according to the manufacturer's procedures (Applied Biosystems). PCR was performed using KAPA2G Fast Hotstart (Kapa Bioscience).

Cell culture and viability assays

ATRT cell line CHLA-02-ATRT (ATCC, Cat# CRL-3020), CHLA-04-ATRT (ATCC, Cat# CRL-3036) were cultured according to the manufacturer's protocol. CHLA-05-ATRT and CHLA-06-ATRT cells, which were derived from primary ATRTs by Dr. Anat Erdreich-Epstein from the Children's Hospital of Los Angeles (Erdreich-Epstein et al., 2014), were cultured in DMEM/F12 supplemented with 20 ng/mL FGF, 20 ng/mL EGF, and 1x B27 supplement. SH cells were obtained from Dr. Shih Hwa Chou at Taipei Veterans General Hospital and was cultured as previously described (Kao et al., 2005). BT12 and BT16, which were kind gifts from Dr. Peter Houghton at Nationwide Children's Hospital, were cultured in RPMI-1640 supplemented with 10% FBS. ATRT 78C cells was established from a corresponding primary ATRT (T13; diagnosed at The Hospital for Sick Children) and cultured in Neurobasal medium supplemented with 75 ng/mL BSA, 10 ng/mL FGF1, 10ng/mL EGF, 2 µg/mL Heparin, 1x B27 and 1x N2 supplements. CHLA266 was grown in IMEM media with 10% FBS and 1x ITS (Xu et al., 2012). G401 (ATCC, Cat# CRL-1441) was grown in McCoy's 5A media with 10% FBS.

Details of ATRT cell lines

Cell Line	Type	Age (Months)	Group	Location	SMARCB1 Status
78C	Primary (T13)	13.0	1	Supratentorial	HMZ Del x1-3
CHLA-05-ATRT	Primary	34.0	1	Supratentorial	HMZ Del x6
CHLA-02-ATRT	Primary	20.4	1	Infra-tentorial	HMZ Del x1-9
CHLA-04-ATRT	Primary	20.0	1	Supratentorial	HMZ p.Gln257X
CHLA-266	Established	18.0	2	Infra-tentorial	HMZ Del x1
34C	Primary (T45)	13.0	2	Infra-tentorial	HMZ pArg40x
SH	Established	n/a	2	Infra-tentorial	HMZ p.Arg53X
CHLA-06-ATRT	Primary	3.0	2	Infra-tentorial	HMZ Del x6
BT16	Established	24.0	2	Infra-tentorial	HMZ p.Met27Argfs*28
BT12	Established	1.5	2	Infra-tentorial	HMZ p.Arg60Glufs*10

To assess effects of NOTCH and BMP signaling on ATRT cell phenotypes, cells were treated with N-[N-(3,5-Difluorophenacetyl)-L-alanyl]-S-phenylglycine t-butyl ester (DAPT; EMD Chemicals, Germany, Cat # 565770) or Dorsomorphin (DM; Sigma-Aldrich, USA, Cat # P5499) and analyzed using MTS assays for cell viability. Similarly, Dasatinib (Selleckchem, US. Cat #S1021 and Nilotinib (Selleckchem, US. Cat#S1033) were used to assess PDFG/Src signaling. Cells were seeded at a density of 30% confluency per well and treated either with DMSO vehicle control or varying doses of DAPT, DM Dasatinib or Nilotinib. On specific days (days 1-5), cells were evaluated with the CellTiter 96 Cell proliferation assay kit (Promega, USA, Cat# G3580) as per the manufacturer's instructions. Epigenetic drugs/probes including Bromodomain proteins (JQ1, PFI-1, 2, 3, GSK2801, SGC-CBP30), Methyltransferases (GSK343, UNC1999, UNC0642, UNC0638, A-366, LLY507) and histone deacetylases (LAQ824) were obtained from the Structure Genomics Consortium (<http://www.thesgc.org>). For epigenomic drug screening experiments, conditions were set up identically with the exception of absorbance readings being taken at 3 and 7 days post-treatment. Cell viability was determined based on mean cell absorbance at 492 nm.

siRNA knockdown of *RBPJ*

To confirm the effect of NOTCH inhibition in ATRT cell lines we used siRNA directed against *RBPJ* (ON-TARGETplus Dharmacon; Cat# L-007772-00-0005) in group 1 (CHLA04, CHLA05) and group 2 (BT12, BT16) cell lines. Cells were seeded in 6-well plates at a density of (1 million per plate for group 1 lines and 250,000 per

plate for group 2) and treated with either an *RBPJ* siRNA pool at a concentration of 25 nM or scramble control RNA according to the manufacturer's instructions. We used Dharmafect 1 Transfection Reagent Cat #T-2001-01. Cell viability was assessed using Alamar Blue at day 1, 3, 5 and 7 days post-treatment, and Western blot analysis of *RBPJ* protein levels confirmed 50-80% effective knockdown relative to scrambled control at 96 hours post transfection

Dasatinib IC50 assays

Group 1 (CHLA02, CHLA04, CHLA05) and group 2 (BT12, BT16, CHLA266, CHLA06) ATRT cell lines were seeded at densities of (10,000 cells per well for CHLA-02, CHLA-04, CHLA-05) and (1000 per well for BT-16, BT-12, CHLA-266 and CHLA-06) in a 96 well plate and grown overnight and treated with Dasatinib the following day. Cell viability was assessed by Alamar Blue, 4 days after treatment using a sixteen point dose curve with drug doses from 10 μ M to 305 pM (2 fold serial dilution series). Percent viable cells at each concentration was determined relative to vehicle control (DMSO). IC50 values were calculated in excel using the XLfit Plugin (IDBS) with the Boltzmann sigmoidal curve fitting algorithm. All experiments were performed in duplicate in three independent biological replicates.

Orthotopic xenografts studies

5×10^5 BT16 cells were injected orthotopically (from Bregma, 2 mm right, 3.8 mm anterior) into NOD scid gamma (NSG) mice and engraftment was allowed for 7 days (n=19 mice each for treatment and vehicle). Dasatinib treatment was initiated at day 7 post-injection and was performed daily using a dose of 30 mg/kg of dasatinib delivered via intraperitoneal (i.p.) injection for a total of 14 days (n=19 treatment, n=19 vehicle). Tumor growth of three representative control and treatment mice was monitored by weekly bioluminescence (BLI) imaging using the IVIS Lumina II system and is expressed as total flux (photons/second) or radiance (photons/second/cm²/steradian). After treatment, mice were monitored until they reached endpoint and were sacrificed at first sign of neurological deficit. Mice studies were conducted in accordance with the policies and regulations for ethical treatment of animals approved for the Toronto Centre for Phenogenomics.

Western blotting and immuno-histochemical analyses

Nuclear and whole cell lysates were prepared using cytosol lysis buffer or nuclear buffer F (Sommer et al., 1998) respectively and immunoblotted with antibodies to SMARCB1/BAF47 (BD Biosciences, USA, Cat # 612110), cleaved NOTCH1 (Cell Signaling, USA, Cat# 2421S), pSMAD1/5 (Cell Signaling, USA, Cat#9516S), SMAD1 (Cell Signaling, USA, Cat# 9743S) or α -Tubulin (Sigma-Aldrich, USA, Cat# T9026) as per standard methods. Phospho-PDGFRB P70 was obtained from Santa Cruz Biotechnology (Santa Cruz, CA, USA, Cat# sc-12909-R) Total PDGFRB (Cat# 3169) was obtained from Cell Signaling Technology. BAF47 immuno-staining of tumor samples was performed by the Hospital for Sick Children Pathology Department (Toronto, ON, Canada) as per standard clinical protocols.

TUNEL assays

TUNEL assays were performed using in situ cell death detection kit, Fluorescein, according to manufacturer's instructions (Roche, West Sussex, UK). Pictures were taken at 20x magnification. Percentage of TUNEL positive population was calculated with respect to DAPI-positive cells, in five random fields per cell cultured slide, and averaged as representative population. Fold-changes were obtained by comparing with untreated control.

qRT-PCR analyses

cDNAs were synthesized from high quality RNA using the High Capacity cDNA Reverse Transcription Kit (Applied Biosystem, Cat# 4368814) as per the manufacturer's instructions and qRT-PCR analyses were performed using purchased Taqman probes and the TaqMan® Gene Expression Master Mix (Invitrogen) (*BAMBI*, *SOST*, *BCR* [exon2, 8, 16, 18, 21, 23], *RGLA*, *CHCHD10*, *MMP11*, *SMARCB1* [exon 2, 5]). A subset of analyses were performed with Platinum SYBR Green qPCR reagent kit (Invitrogen) as per the manufacture's protocol with in-house designed primers to amplify invariant exons (*HES1*, *HES5*). For gene expression analysis of DAPT or DM treated cells, RNA was isolated from test and control cell lines at four days post-treatment. Synthesized cDNA were analysed with gene specific probes using the Platinum SYBR green qPCR reagent kit. The ΔC_t or $\Delta\Delta C_t$ method was used to calculate mRNA expression levels.

Primers used for qRT-PCR analyses

Gene	Forward Primer (5'-3')	Reverse Primer (5'-3')
<i>BAMBI (Ex3)</i>	GGGCAGGTTGCAAAGTTAGA	ATCGTTGCTGAGGTCTGCTT
<i>BCR (Ex2)</i>	TCGGAACACCACCTGGATAC	GATGAGGAGGGCGAGTCAT
<i>BCR (Ex8)</i>	CTTGCTGAAGCACACTCCTG	GGGTGTGATCTCCTCATTGAT
<i>BCR (Ex16)</i>	GCTCCCAGACCCTGAGGATAC	CCCTTCCCCATGAGTCTGTC
<i>BCR (Ex18)</i>	AGCTCTCGGTCAAGTTCAACA	TTGGTGACCACAGCAATCTT
<i>BCR (Ex21)</i>	TCTTTCAGACCCGGTTGC	TTTTTCAGGTGGTCCAGAAGG
<i>BCR (Ex23)</i>	TGATGATGAGCGAGATGGAC	CTGCGAAGTTGGGGTAGAAC
<i>CHCHD10 (Ex3)</i>	GCCTACGAGATCAGGCAGTT	GGTAGTACTTGCACTGCTTCAGG
<i>HES1 (Ex4)</i>	GAGAGGCGGCTAAGGTGTTT	GTGTAGACGGGGATGACAGG
<i>HES5 (Ex3)</i>	CTTTTGTGAAGGCCGAACTC	CACACTCAGGAGCCTTTTGG
<i>MMP11 (Ex2)</i>	ATGCAGCCCTGCCAGTA	GGCACTCAGCCCATCAGA
<i>RGL4 (Ex11)</i>	CTGGCTGGTCTTTCTCCTTG	AACCTTTGGAGAACCCCAAGT
<i>SMARCB1 (Ex2)</i>	TCCGTATGTTCCGAGGTTCT	TTTACCATGTGACGATGCAA
<i>SMARCB1 (Ex5)</i>	CCCAGCTGTGATCCATGAG	TCCAGGTGAAGGCGTCTC
<i>SOST (Ex2)</i>	ATGGGCAGAGGTGAGAGAGA	TTGGCTGTGAGAAGAGAGCA

Statistical Analyses

Difference in nucleotide transition/transversion rates from next generation sequencing SNV calls were determined using the two-proportion Z test with Yates' correction for continuity. Significance of gender, location, metastasis, and individual genomic loci differences between the molecular subgroups were analyzed using a two-sided Fisher's exact test. Kruskal-Wallis test was used to assess significance of tumor subgroups in relation to age, and counts of genomic alterations. All analyses were conducted in the R statistical environment (v2.15.2) or with SPSS version 22.0. A p value of < 0.05 was regarded as significant for all analyses.

Contributing Institutions

Institution	CPBTC Institution	Location
The Hospital for Sick Children	C17 CPBTC	Toronto, Ontario, Canada
Montreal Children's Hospital	C17 CPBTC	Montreal, Quebec, Canada
Children's Hospital Colorado, University of Colorado Denver		Denver, Colorado, USA
Children's Hospital of Los Angeles		Los Angeles, USA
Virginia Commonwealth University, Richmond		Virginia, USA
Chinese University of Hong Kong		Hong Kong, China
Seoul National University Children's Hospital		Seoul, South Korea
Asan Medical Center		Seoul, South Korea
Stollery Children's Hospital	C17 CPBTC	Edmonton, Alberta, Canada
University of British Columbia		Vancouver, BC, Canada
Hospital de Santa Maria, Centro Hospitalar Lisboa Norte		Lisbon, Portugal
Kumamoto University		Kumamoto, Japan
Schneider Hospital		Petach Tikva, Isreal
Ludwig-Maximilians-University		Munich, Germany
University of California, San Francisco		San Francisco, USA
University of Bonn		Bonn, Germany
Shizuoka Children's Hospital		Aoi-ku, Shizuoka, Japan
Alberta Children's Hospital	C17 CPBTC	Calgary, Alberta, Canada
British Columbia's Children's Hospital	C17 CPBTC	Vancouver, BC, Canada
CancerCareManitoba	C17 CPBTC	Winnipeg, Manitoba, Canada

Contributing Institutions continued

Institution	CPBTC Institution	Location
The Children's Hospital of Eastern Ontario	C17 CPBTC	Ottawa, Ontario, Canada
The Sainte-Justine University Hospital Centre	C17 CPBTC	Montreal, Quebec, Canada
IWK Health Centre	C17 CPBTC	Halifax, Nova Scotia, Canada
Children's Health Research Institute	C17 CPBTC	London, Ontario, Canada
McMaster Children's Hospital	C17 CPBTC	Hamilton, Ontario, Canada
University of Utah School of Medicine		Salt Lake City, USA
University of Debrecen		Debrecen, Hungary
Semmelweis University		Budapest, Hungary
University of Szeged		Szeged, Hungary
Portuguese Cancer Institute		Lisbon, Portugal
Uppsala University Hospital		Uppsala, Sweden
CHU Sainte-Justine/Université de Montréal	C17 CPBTC	Montreal, Quebec, Canada
Taipei Veterans General Hospital		Taipei, Taiwan
Hadassah Hebrew University Hospital		Jerusalem, Israel
Shizuoka Children's Hospital		Aoi-ku, Shizuoka, Japan
The University of Nottingham		Nottingham, United Kingdom
Seoul National University Children's Hospital		Seoul, Korea
Seoul National University Hospital		Seoul, Korea
St. Jude Children's Research Hospital		Memphis, Tennessee, USA
Vancouver General Hospital		Vancouver, BC, Canada
The Children's Hospital at Westmead		Brisbane, Queensland, Australia
Children's Cancer Centre, Murdoch Children's Research Institute		Melbourne, Victoria, Australia
Princess Margaret Cancer Center-University Health Network		Toronto, Ontario, Canada
Groupement Hospitalier Est, CHU de Lyon-Bron, France		Lyon-Bron, France
Faculty of Medicine, Ramathibodi Hospital, Mahidol University		Bangkok, Thailand
Cincinnati Children's Hospital Medical Center		Cincinnati, Ohio, USA
Ann and Robert H. Lurie Children's Hospital of Chicago		Chicago, Illinois, USA
Children's Medical Center of Israel		Petach Tikva, Israel

Supplemental References

- Buenrostro, J. D., Giresi, P. G., Zaba, L. C., Chang, H. Y., and Greenleaf, W. J. (2013). Transposition of native chromatin for fast and sensitive epigenomic profiling of open chromatin, DNA-binding proteins and nucleosome position. *Nature methods* *10*, 1213-1218.
- Cancer Genome Atlas Research, N. (2013). Genomic and epigenomic landscapes of adult de novo acute myeloid leukemia. *N Engl J Med* *368*, 2059-2074.
- Chen, K., Wallis, J. W., McLellan, M. D., Larson, D. E., Kalicki, J. M., Pohl, C. S., Mcgrath, S. D., Wendl, M. C., Zhang, Q., Locke, D. P., *et al.* (2009). BreakDancer: an algorithm for high-resolution mapping of genomic structural variation. *Nature methods* *6*, 677-681.
- Court, F., Baniol, M., Hagege, H., Petit, J. S., Lelay-Taha, M. N., Carbonell, F., Weber, M., Cathala, G., and Forne, T. (2011). Long-range chromatin interactions at the mouse *Igf2/H19* locus reveal a novel paternally expressed long non-coding RNA. *Nucleic Acids Res* *39*, 5893-5906.
- Erdreich-Epstein, A., Robison, N., Ren, X., Zhou, H., Xu, J., Davidson, T. B., Schur, M., Gilles, F. H., Ji, L., Malvar, J., *et al.* (2014). *PID1* (*NYGGF4*), a new growth-inhibitory gene in embryonal brain tumors and gliomas. *Clin Cancer Res* *20*, 827-836.
- Ha, G., Roth, A., Lai, D., Bashashati, A., Ding, J., Goya, R., Giuliany, R., Rosner, J., Oloumi, A., Shumansky, K., *et al.* (2012). Integrative analysis of genome-wide loss of heterozygosity and monoallelic expression at nucleotide resolution reveals disrupted pathways in triple-negative breast cancer. *Genome Res* *22*, 1995-2007.
- Hagege, H., Klous, P., Braem, C., Splinter, E., Dekker, J., Cathala, G., de Laat, W., and Forne, T. (2007). Quantitative analysis of chromosome conformation capture assays (3C-qPCR). *Nat Protoc* *2*, 1722-1733.
- Heinz, S., Benner, C., Spann, N., Bertolino, E., Lin, Y. C., Laslo, P., Cheng, J. X., Murre, C., Singh, H., and Glass, C. K. (2010). Simple combinations of lineage-determining transcription factors prime cis-regulatory elements required for macrophage and B cell identities. *Molecular cell* *38*, 576-589.
- Johnson, W. E., Li, C., and Rabinovic, A. (2007). Adjusting batch effects in microarray expression data using empirical Bayes methods. *Biostatistics* *8*, 118-127.
- Kao, C.-L., Chiou, S.-H., Chen, Y.-J., Singh, S., Lin, H.-T., Liu, R.-S., Lo, C.-W., Yang, C.-C., Chi, C.-W., Lee, C.-h., and Wong, T.-T. (2005). Increased expression of osteopontin gene in atypical teratoid/rhabdoid tumor of the central nervous system. *Modern Pathology* *18*, 769-778.
- Morin, R. D., Mungall, K., Pleasance, E., Mungall, A. J., Goya, R., Huff, R. D., Scott, D. W., Ding, J., Roth, A., Chiu, R., *et al.* (2013). Mutational and structural analysis of diffuse large B-cell lymphoma using whole-genome sequencing. *Blood* *122*, 1256-1265.
- Morris, T. J., Butcher, L. M., Feber, A., Teschendorff, A. E., Chakravarthy, A. R., Wojdacz, T. K., and Beck, S. (2014). ChAMP: 450k Chip Analysis Methylation Pipeline. *Bioinformatics* *30*, 428-430.
- Northcott, P. A., Shih, D. J., Remke, M., Cho, Y. J., Kool, M., Hawkins, C., Eberhart, C. G., Dubuc, A., Guettouche, T., Cardentey, Y., *et al.* (2012). Rapid, reliable, and reproducible molecular sub-grouping of clinical medulloblastoma samples. *Acta neuropathologica* *123*, 615-626.
- Robertson, G., Schein, J., Chiu, R., Corbett, R., Field, M., Jackman, S. D., Mungall, K., Lee, S., Okada, H. M., Qian, J. Q., *et al.* (2010). De novo assembly and analysis of RNA-seq data. *Nature methods* *7*, 909-912.
- Ross-Innes, C. S., Stark, R., Teschendorff, A. E., Holmes, K. A., Ali, H. R., Dunning, M. J., Brown, G. D., Gojis, O., Ellis, I. O., Green, A. R., *et al.* (2012). Differential oestrogen receptor binding is associated with clinical outcome in breast cancer. *Nature* *481*, 389-393.

Sommer, A., Bousset, K., Kremmer, E., Austen, M., and Luscher, B. (1998). Identification and characterization of specific DNA-binding complexes containing members of the Myc/Max/Mad network of transcriptional regulators. *The Journal of biological chemistry* 273, 6632-6642.

Tibshirani, R., Hastie, T., Narasimhan, B., and Chu, G. (2002). Diagnosis of multiple cancer types by shrunken centroids of gene expression. *Proceedings of the National Academy of Sciences of the United States of America* 99, 6567-6572.

Trapnell, C., Roberts, A., Goff, L., Pertea, G., Kim, D., Kelley, D. R., Pimentel, H., Salzberg, S. L., Rinn, J. L., and Pachter, L. (2012). Differential gene and transcript expression analysis of RNA-seq experiments with TopHat and Cufflinks. *Nat Protoc* 7, 562-578.

Wang, J., Mullighan, C. G., Easton, J., Roberts, S., Heatley, S. L., Ma, J., Rusch, M. C., Chen, K., Harris, C. C., Ding, L., *et al.* (2011). CREST maps somatic structural variation in cancer genomes with base-pair resolution. *Nature methods* 8, 652-654.

Wilkerson, M. D., and Hayes, D. N. (2010). ConsensusClusterPlus: a class discovery tool with confidence assessments and item tracking. *Bioinformatics* 26, 1572-1573.

Xu, J., Erdreich-Epstein, A., Gonzalez-Gomez, I., Melendez, E. Y., Smbatyan, G., Moats, R. A., Rosol, M., Biegel, J. A., and Reynolds, C. P. (2012). Novel cell lines established from pediatric brain tumors. *Journal of neuro-oncology* 107, 269-280.

Ye, K., Schulz, M. H., Long, Q., Apweiler, R., and Ning, Z. (2009). Pindel: a pattern growth approach to detect break points of large deletions and medium sized insertions from paired-end short reads. *Bioinformatics* 25, 2865-2871.

Zerbino, D. R., and Birney, E. (2008). Velvet: algorithms for de novo short read assembly using de Bruijn graphs. *Genome Res* 18, 821-829.

Zhang, X., Cowper-Salari, R., Bailey, S. D., Moore, J. H., and Lupien, M. (2012). Integrative functional genomics identifies an enhancer looping to the SOX9 gene disrupted by the 17q24.3 prostate cancer risk locus. *Genome Res* 22, 1437-1446.

Zhang, Y., Liu, T., Meyer, C. A., Eeckhoute, J., Johnson, D. S., Bernstein, B. E., Nusbaum, C., Myers, R. M., Brown, M., Li, W., and Liu, X. S. (2008). Model-based analysis of ChIP-Seq (MACS). *Genome Biol* 9, R137.